

cy 1

**ARCHIVE COPY
DO NOT LOAN**

I-543

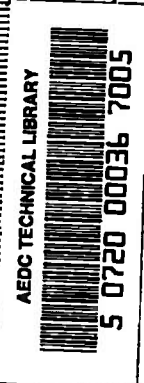


**EXPERIMENTAL DETERMINATION OF GAS
PROPERTIES AT HIGH TEMPERATURES
AND/OR PRESSURES**

C. Carey, J. Bradshaw, E. Lin, and E. H. Carnevale
Panametrics, Inc.
Waltham, Massachusetts

May 1974

Final Report for Period September 1971 - October 1973



Approved for public release; distribution unlimited.

Property of U. S. Air Force
AEDC LIBRARY
F40600-74-C-0001

Prepared for

**ARNOLD ENGINEERING DEVELOPMENT CENTER (DYFS)
AIR FORCE SYSTEMS COMMAND
ARNOLD AF STATION, TENNESSEE 37389**

NOTICES

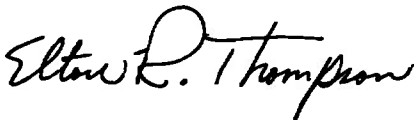
When U. S. Government drawings specifications, or other data are used for any purpose other than a definitely related Government procurement operation, the Government thereby incurs no responsibility nor any obligation whatsoever, and the fact that the Government may have formulated, furnished, or in any way supplied the said drawings, specifications, or other data, is not to be regarded by implication or otherwise, or in any manner licensing the holder or any other person or corporation, or conveying any rights or permission to manufacture, use, or sell any patented invention that may in any way be related thereto.

Qualified users may obtain copies of this report from the Defense Documentation Center.

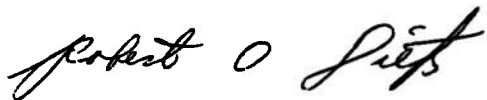
References to named commercial products in this report are not to be considered in any sense as an endorsement of the product by the United States Air Force or the Government.

APPROVAL STATEMENT

This technical report has been reviewed and is approved.



ELTON R. THOMPSON
Research and Development
Division
Directorate of Technology



ROBERT O. DIETZ
Director of Technology

REPORT DOCUMENTATION PAGE		READ INSTRUCTIONS BEFORE COMPLETING FORM
1. REPORT NUMBER AEDC-TR-74-33	2. GOVT ACCESSION NO.	3. RECIPIENT'S CATALOG NUMBER
4. TITLE (and Subtitle) EXPERIMENTAL DETERMINATION OF GAS PROPERTIES AT HIGH TEMPERATURES AND/OR PRESSURES		5. TYPE OF REPORT & PERIOD COVERED Final Report-September 1971 to October 1973
		6. PERFORMING ORG. REPORT NUMBER
7. AUTHOR(s) Carey, C., Bradshaw, J., Lin, E., and Carnevale, E. H., Panametrics, Inc., Waltham, Massachusetts		8. CONTRACT OR GRANT NUMBER(s) F40600-72-C-0006
9. PERFORMING ORGANIZATION NAME AND ADDRESS Panametrics, Inc. Waltham, Massachusetts		10. PROGRAM ELEMENT, PROJECT, TASK AREA & WORK UNIT NUMBERS Program Element 61102F Project 7065
11. CONTROLLING OFFICE NAME AND ADDRESS Arnold Engineering Development Center (DYFS), Arnold Air Force Station, TN 37389		12. REPORT DATE May 1974
		13. NUMBER OF PAGES 137
14. MONITORING AGENCY NAME & ADDRESS (if different from Controlling Office) Arnold Engineering Development Center (DYR), Arnold Air Force Station, TN 37389		15. SECURITY CLASS. (of this report) UNCLASSIFIED
		15a. DECLASSIFICATION/DOWNGRADING SCHEDULE N/A
16. DISTRIBUTION STATEMENT (of this Report) Approved for public release; distribution unlimited.		
17. DISTRIBUTION STATEMENT (of the abstract entered in Block 20, if different from Report) <i>1. Gases -- Properties -</i>		
18. SUPPLEMENTARY NOTES <i>2 " " " "</i> <i>3 " " " "</i> Available in DDC <i>4 " " " "</i>		
19. KEY WORDS (Continue on reverse side if necessary and identify by block number) gases, properties of diffusion, viscosity, transport properties, thermal conductivity, ultrasonics, kinetic theory, acoustic cavities		
20. ABSTRACT (Continue on reverse side if necessary and identify by block number) A new technique for the accurate (1-0.01%) determination of transport and thermodynamic properties of gases is described. This technique consists of measuring the linewidth of a small acoustic resonator. The linewidth of more than one type of resonance allows the transport properties (thermal conductivity and viscosity) to be determined independently. The center frequency gives the sound speed. The theory of the acoustic resonator is presented including		

20. ABSTRACT (Continued)

the effects of relaxation in the gas, slip and accommodation on the cavity walls, and acoustic transmission into the walls. The contributions of transducer coupling and feedthrough are also included in the cavity theory. Realization of cavities and transducers suitable (but not optimized) for measurements at temperatures up to 1000°K and pressures up to 500 atm are discussed. Measurements employing the resonator technique are presented in Ar, N₂, air and H₂. High pressure measurements (p < 460 atm) span temperatures between 300 and 600°K. Measurements at 1 atm at temperatures up to 1000°K are also presented. In N₂ and air measurement accuracies of the order of 0.1% in viscosity are verified in the present work. Consideration of the theory and experimental state-of-the-art indicates 0.01% in viscosity is possible under optimum conditions.

PREFACE

This report was prepared by Panametrics, Inc., Waltham, Massachusetts, under U. S. Air Force Contract No. F40600-72-C-0006. This contract was initiated under Air Force Project 7065, Program Element 61102F. The work was jointly sponsored by the Aerospace Research Laboratory and Arnold Engineering Development Center, Air Force Systems Command, with Mr. Elton R. Thompson (AEDC/DYR), Project Manager.

This report covers work performed between September 1971 and October 1973.

The manuscript was released by the authors October 1973 for publication as a technical report.

The authors would like to acknowledge James Bradshaw and Raymond Morris for the design and construction of special electronic apparatus. The authors are grateful to E. A. Mason and J. V. Sengers for many helpful suggestions.

The reproducibles used in the reproduction of this report were supplied by the authors.

TABLE OF CONTENTS

	<u>Page</u>
LIST OF ILLUSTRATIONS	5
LIST OF TABLES	6
LIST OF SYMBOLS	8
I. INTRODUCTION	15
1.1 Objective	15
II. THEORY OF IDEAL CAVITY RESPONSE	18
2.1 Linewidth and Center Frequency in Acoustic Gas Resonators	18
2.2 Physical Basis of Cavity Equations	24
III. CORRECTIONS TO BASIC CAVITY THEORY DUE TO TRANSDUCER COUPLING AND ELECTRICAL FEEDTHROUGH	30
3.1 Effects of Coupling Hole Transmission Lines.	30
3.2 Effects of Coupling Hole Reflection Coefficients	33
3.3 Mode Coupling Effects.	34
3.4 Feedthrough Routines for Data Reduction.	36
3.5 Summary Data Reduction Procedure	45
IV. EXPERIMENTAL APPARATUS AND RESULTS.	49
4.1 Summary of Experimental Problems With Gas-Filled Acoustic Cavities	49
4.2 Mechanical Hardware.	50
4.3 Transducers.	61
4.4 Electronics.	66
4.5 Data	76
V. SUMMARY	86
REFERENCES.	88

TABLE OF CONTENTS (cont'd)

	<u>Page</u>
APPENDIX A - TRAVELING WAVES IN A CYLINDRICAL WAVE GUIDE.	93
APPENDIX B - EFFECTS OF MULTIPLE WAVES IN COUPLING HOLES126
APPENDIX C - REFLECTION AND TRANSMISSION COEFFICIENTS AT COUPLING HOLES129

LIST OF ILLUSTRATIONS

<u>Figure</u>	<u>Page</u>
1. Variation of phase and amplitude with frequency near a resonance	19
2. Amplitude versus frequency response over several resonances	22
3. Signal paths for resonant cavity transport and thermodynamic property measurements.	37
4a. Composite measured signal polar diagram.	43
4b. Vector diagram for various components in cavity output	43
5. Techniques for exciting acoustic cavities with good wall isolation.	51
6. Aminco high pressure cell and pvt equipment.	53
7. Hastalloy high pressure cell for high pressure use.	54
8. Quartz oven for low pressure-high temperature use.	55
9. Cavity and furnace for measurements in atmospheric air.	57
10. Acoustic cavity and transducer	58
11. Circuit details for cavity proof tests	67
12. Improved electronic system for cavity measurements	69
13. Driver amplifier with cathode follower	70
14. Block diagram of automated line width measurement system using a double side band technique	73
15. Block diagram of hybrid circuit.	75
16. Timing diagram for digital synthesizer decoder	77
B1. Definition of terms for coupling hole problem	127
C1. Terminology for hole coupling problem.	130

LIST OF TABLES

<u>Table</u>	<u>Page</u>
1. Constants for first approximation linewidths for symmetric modes in a cylindrical acoustic cavity.	23
2. Ratio of mean free path to viscous wavelength for nitrogen under typical pressure-temperature and frequency conditions	26
3. Typical linewidth components (argon 300°K) for the first longitudinal mode.	31
4. Material and dimensional characteristics of cavities used to measure data reported below . . .	60
5. Dielectric and flexible electrode parameters . . .	63
6. High temperature measurements in nitrogen (1 atm).	78
7. High temperature measurements in air (1 atm) . . .	79
8. High pressure measurements in nitrogen	80
9. High pressure measurements in air.	81
10. High pressure measurements in hydrogen	82
11. High pressure measurements in argon.	83
12. High pressure-temperature measurements in argon.	84
13. High pressure-temperature measurements in hydrogen	85
A.1. Summary of wave equations for acoustic, thermal and viscosity potentials (see Ref. 3).	94
A.2. (Ratio thermal to acoustic wavelength) ² for nitrogen at several pressures and temperatures	96
A.3. Expression for particle velocity and temperature at the wall.	102
A.4. Simultaneous equations for $A_p^{(n)}$ derived from temperature and particle velocity boundary condition.	103

LIST OF TABLES (cont'd)

<u>Table</u>		<u>Page</u>
A.5.	Dispersion relation for acoustic waves in a cylindrical wave guide with slip accomodation and acoustic transmission into the walls105
A.6.	Second order correction factors for nonideal acoustic wave guide in p'th radial mode.111
A.7.	Boundary conditions for acoustic source wall . .	.114
A.8.	Total second order correction factor for viscosity and thermal conductivity in cavity linewidth expressions.123
C.1.	First two orthogonalized wave functions in a coupling tube.136

LIST OF SYMBOLS

a	Cavity radius
a_1, a_2	Mode strength for acoustic and thermal waves, respectively (Eq. A. 7 and Table 1)
A	Pressure amplitude of resonance line
A_+, A_-	Amplitudes at the half power points
A_o	Maximum pressure amplitude
c	Sound speed
c_w	Sound speed in wall material
C_f	Cavity signal including all transducer effects
\bar{C}_p	Complex specific heat at constant pressure $\bar{C}_p = C_p + (\bar{C}_v - C_v)$
C_p, C_v	Equilibrium specific heats
\bar{C}_v	Complex specific heat at constant volume
C_{vw}	Specific heat of wall materials
d	Cavity length
f	Frequency
F	Cavity response function
F_1, F_2	Coupling hole response functions (Eq. B. 1)
g_η (pn)	Mode factor for viscous component of coupling hole loss
g_λ (pn)	Mode factor for thermal component of coupling hole loss
G^+, G^-	Green's functions for coupling hole and cavity, respectively (C. 14, C. 15)

LIST OF SYMBOLS (cont'd)

G_p	Transmitter acoustic source strength
$G(pn)$	Mode factor for coupling hole losses for a mode with radial mode number p and longitudinal mode number n , calculated with "lossless" wave functions in coupling holes.
h	Side wall loss wave number (A. 55)
H_1, H_2, H_3	Velocity potential for acoustic, thermal and viscous waves, respectively.
J_0, J_1	Zero order Bessel's functions, first order Bessel's functions.
k_1	Complex free wave acoustic wave number $\sim \frac{\omega}{c}$.
k_2, k_3	Thermal and viscous wave numbers.
$k_s^{(1)}, k_p^{(1)}$	Complex wave number for sth or pth radial mode waves, i. e., $k_p^{(1)2} \sim k_1^2 - \gamma_p^2$. Note $k_p^{(1)}$ becomes very small near a radial resonance.
K_n, k_m	Wave numbers in cavity and coupling tube, respectively, for hole correction calculations.
K_T	Isothermal compressibility
l	Coupling hole length
l_t	Accommodation length for thermal exchange at a wall
l_v	Accommodation length for momentum exchange at a wall
l_D	Range of thermal wave in wall (A. 22)
L	Mean free path
p	Pressure fluctuations in sound field
P_r	Prandtl number $\frac{\eta C}{\lambda}$

LIST OF SYMBOLS (cont'd)

Q	Quality factor or ratio of center frequency to linewidth of a resonant element.
Q_w	Heat flux to cavity walls
r	Radial cavity coordinate
r_o	Coupling hole radius
R	Gas constant per gram
R'	Ratio of cavity radius to cavity length
R_m^s	Amplitude excitation coefficient for the mth mode when the sth mode is incident on coupling hole.
R_s^s	Amplitude reflection coefficient for the sth mode in cavity incident on coupling hole (Eq. C. 6).
S	Cavity surface
t_m^s	Amplitude excitation coefficient for the mth mode in the coupling tube exiting the sth mode in cavity.
T, T_w	Temperature fluctuations in gas and wall, respectively.
$T_{1.}$	Amplitude transmission coefficient for waves from transmit coupling hole into cavity.
$T_{.2}$	Amplitude transmission coefficient for waves in cavity into receive coupling hole.
U_m^s	Coupling coefficient for the sth mode waves incident on cavity end walls generating the mth mode waves (C. 3).
\bar{V}_f	Complex received feedthrough voltage.
V_m^s	Coupling coefficient for the sth mode waves in coupling holes incident on cavity generating the mth mode waves cavity surface.
\bar{V}_s	Complex received signal voltage.

LIST OF SYMBOLS (cont'd)

Y	Effective wall modulus-pressure in wall divided by normal strain in wall.
z	Axial cavity coordinate.
Z	Compressibility factor.
α_s	Side wall acoustic transmission factor (Eq. A. 27).
α_E	End wall acoustic transmission factor.
β	Thermal expansion coefficient and δ is in units of angular frequencies.
$\beta_1, \beta_2, \beta_3$	Proportionality constants for derivatives of acoustic (A. 37), viscous (A. 33) and thermal (A. 33) waves, respectively.
γ	Specific heat ratio $\left(\frac{C_p}{C_v}\right)$.
$\bar{\gamma}$	Complex specific heat $\frac{\bar{C}_p}{C_v} = \gamma_R + i\gamma_I$.
γ_p	Lossless radial wave number equals the pth root of the order of Bessel's function divided by the tube or cavity radius $\sim \frac{\omega p_0}{c}$.
$\gamma_p^{(2)}, \gamma_p^{(3)}$	Radial wave numbers for viscous and thermal waves (A. 15 and A. 16).
γ_R	Real part of specific heat.
δ	Half width of a Lorentzian line. Note the linewidth is 2δ and δ is angular frequency.
δ_h	Effective linewidth correction due to propagation delays in coupling holes.
δ_v	Frequency normalized linewidth due to volume losses (see Table 1).

LIST OF SYMBOLS (cont'd)

Δ_{np}	Linewidth contribution due to acoustic transmission into cavity walls.
$\Delta\phi_+$	Signal phase shift correction at ω for tuned amplifier set to ω_0 .
ϵ_+, ϵ_-	Acoustic transmission loss factors (A.62).
$\epsilon_{sp} \ 1/2 \ k_1$	Imaginary part of acoustic mode wave number (A.47).
η	Viscosity
θ	Normalized temperature defined by Eq. (A.6).
θ_n	Phase shift of sth wave upon reflection or coupling (C.5).
λ	Thermal conductivity.
λ_t	Wavelength for thermal waves.
λ_v	Wavelength for viscous waves.
λ_w	Thermal conductivity of wall material.
μ^s_0	Particle velocity in σ .
ρ	Density
ρ_w	Density of wall material.
σ	Surface of coupling hole cavity interface $d\sigma = 2\pi r dr$ $0 < r < r_0$.
ϕ_h	Phase angle of complex quantity $F_1 T_1 \cdot T_2 F_2$.
ϕ_s	sth radial wave function in cavity (Fig. C1).
χ_μ	Trial functions for variational calculation of particle velocity σ (Eq. C.18).
ψ_m	mth radial wave function in coupling hole (Fig. C1).

LIST OF SYMBOLS (cont'd)

ω	Angular frequency $2\pi f$.
ω_+, ω_-	Upper and lower half power points.
ω_m	Modulation frequency. If ω_o is the carrier a balanced mixer produces $\omega_o + \omega_m$ and $\omega_o - \omega_m$.
ω_o	Angular frequency at maximum amplitude.
ω_{pn}	The center frequency of the lossless cavity mode with longitudinal mode number n and radial mode number p .

SECTION I

INTRODUCTION

1.1 OBJECTIVE

The objective of this work is the experimental determination of gas properties at high temperatures and/or pressures. The temperature range is up to 1500°K and the pressure range is up to 400 atm. These measurements are needed for engineering needs as well as to support potential function and dense gas theory requirements.

Transport and thermodynamic properties are the data base for aerodynamics, gas phase engine design, refrigeration, and many important industrial applications. Uncertainties of 15% are apparent¹ in the specific heat of a simple gas such as argon at ~800 atm 300°C. The thermal conductivity of many common polar and polyatomic gases and their mixtures are not known to 50% at extremely low (100°C) and high temperatures or at high densities. In addition, new propulsion systems and laser systems generate new gas property requirements. Recent experience in chemical laser research, for instance, has generated property requirements in gases for which no information was available. Finally, improvements in computational and test capabilities continually require extended range or accuracy in gas property information. The long lead time required to produce new measurements and to critically evaluate them, calls for a basic research effort.

New techniques based on acoustic and schlieren interferometric measurements have been developed at Panametrics to help expand this data base. An ultrasonic pulse^{2, 3} technique in arcs and shock tubes was used to measure transport properties of largely dissociated and monatomic gases. The ultrasonic technique becomes intractable in the temperature region corresponding to about 0.1% to 80% dissociation. Therefore, a schlieren interferometric technique^{4, 5} employing the end wall boundary layer in a shock tube was developed.

The acoustic pulse technique was used to help fulfill the requirements for high pressure transport and thermodynamic properties. It was found that the sound speeds measured this way could provide useful specific heat data (~0.1%). However, the sound absorption consisted of a sum of viscosity, thermal conductivity and bulk viscosity. The bulk viscosity was approximately as large as the density effect in viscosity and thermal conductivity, therefore, a more complete theory than is available today is required to make pulse absorption measurement useful.

However, the pulse technique can provide useful information on diffusion of helium and hydrogen in the heavier gases.^{6, 7}

The data required to satisfy the high pressure requirements must be high precision so that an accurate estimate of the excess transport properties can be obtained. Also, independent measurements of viscosity and thermal conductivity are required. These objectives can be in principle achieved with an acoustic cavity resonance technique. High precision can be achieved with the cavity technique because all measurements can be reduced to frequency. The center frequency provides sound speed, which can be used at low pressures to calibrate temperature sensors. The linewidth provides transport properties. Measurement of linewidth for different types of resonances, i. e., radial, longitudinal, provides simultaneous viscosity and thermal conductivity values. Thus, one obtains a complete set of highly accurate thermodynamic and transport properties from this cavity technique.

During the past three years the acoustic resonant cavity technique for measuring the thermodynamic and transport properties of gases in the "low" temperature range $300 < T < 1000$ °K and pressure range 1-500 atm has been demonstrated. This technique compliments the pulse ultrasonic optical techniques developed for elevated temperatures ($1000 < T < 20,000$) during the first few years of the present effort. The cavity technique is extremely precise because the measurements have been reduced to easily measured quantities - frequency, a 90° phase angle, and cavity radius. The theory of the resonator indicates that the acoustic resonance technique should be capable of yielding 0.01% in viscosity and 0.05% in thermal conductivity. However, we have only pushed the precision to 0.1% in viscosity and 0.5% in thermal conductivity for the sake of supplying immediate engineering needs. It should also be noted that 0.5% viscosity and 1% thermal conductivity measurements seem possible⁸ with wave guide driven cavities up to ~2000 °K.

The present report discusses the precision of the cavity technique, some experimental realizations of the cavity technique electronic readout options, and the results of a systematic measurements program in nitrogen, air, hydrogen, and argon. The first section of this report discusses how well the cavity response can be described. This includes the dependence of linewidth and center frequencies on viscosity, thermal conductivity, relaxation times and sound speed (thermodynamics). Also discussed here are the effects of nonideal boundary conditions such as slip, accommodation, and wave leakage into the cavity walls. The effects of the transducers on the cavity response are discussed in the

second section. Mode coupling, transducer coupling, electrical and acoustic feedthrough, are included in the cavity response. Temperature limitations imposed mainly by the transducer are discussed. All these effects are dependent on how one chooses to construct and drive the cavity. Methods of "reading out" sufficient information electronically to determine transport and thermodynamic properties are given with typical results. Finally, the experimental gas properties determined in the past year and a half are presented.

SECTION II

THEORY OF IDEAL CAVITY RESPONSE

2.1 LINEWIDTH AND CENTER FREQUENCY IN ACOUSTIC GAS RESONATORS

The linewidth and center frequency of an acoustic resonance line illustrated in Fig. 1 can be related to the properties of the gas in the cavity. Since we are using small amplitude disturbances (1 pt in 10^9 to 10^6) the linearized conservation equations of fluid dynamics describe the cavity performance to the limit that the continuum theory is valid. In addition, the linearity allows the device equations to be worked out as accurately as one desires. First, the completeness of the device equations is never in question as is the case with the nonlinear corrections (convection, edge, and entrance corrections) necessary in other techniques for transport property measurement. Second, the calculations can always be carried out with orthogonal functions and perturbation theory in such a way that the maximum error in the neglected terms can be calculated. Finally, slip and accommodation can easily be included in the theory by modifying the wall boundary conditions. The section below will show how the linewidth and center frequency are related to the gas properties and boundary conditions to 0.01% in linewidth.* However, before launching into details, a summary of the first order results is appropriate.

The gas property information is contained in the resonator line shape. The line shape is the complex pressure amplitude versus frequency characteristics of the cavity. Although the line shape can have a very complex mathematical form, a Lorentzian line shape is a useful approximation because of its simplicity. The pressure \bar{p} in the sound field of a cavity driven at frequency f is

$$\bar{p} = \frac{A \delta}{2 \pi (f - f_0) + i \delta} \quad (1)$$

in the Lorentzian approximation. A is the pressure at the maximum amplitude point, that is, at $f = f_0$. The center frequency is f_0 , and the half width is δ .

*This corresponds to $\frac{0.01\%}{Q}$ in sound speed. See below.

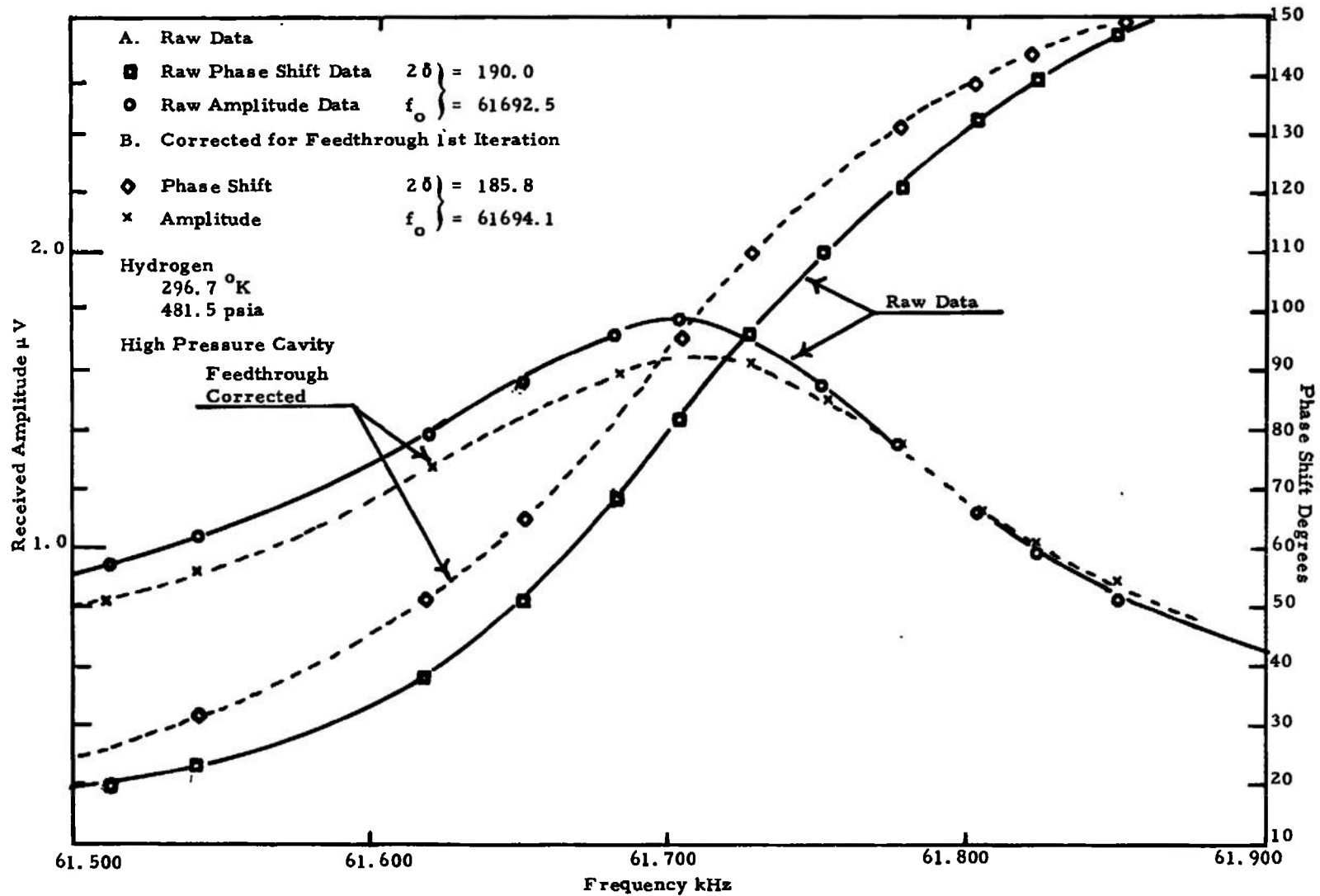


Fig. 1. Variation of phase and amplitude with frequency near a resonance.

The complex pressure is used to simplify the bookkeeping, and is composed of the pressure amplitude and a phase factor $e^{i\phi}$. Only complex pressures are found in nature because phase in addition to frequency and pressure is necessary to specify the sound wave. The phase of the complex pressure in the cavity is measured relative to the pressure wave driving the cavity. Experimentally, the cavity is driven by some incident pressure wave at one end wall and the resulting field in the cavity sensed at the other end wall. The frequency of the driving wave is varied while the amplitude and phase of the pressure in the cavity are measured.

The amplitude and phase variation versus frequency is shown in Fig. 1 near an acoustic resonance. The most distinctive feature of the cavity response is the maximum amplitude at f_0 . The center frequency can be measured using this amplitude measurement to a

$\left(\frac{\Delta f}{f_0}\right)$ which depends on the linewidth (δ) and the amplitude uncertainty

by the relation

$$\frac{\Delta f_0}{f_0} = \frac{\delta}{2\pi f_0} \frac{dA}{A} \quad (2)$$

where ΔA is the pressure amplitude jitter and A is the pressure amplitude. The linewidth can be measured by varying the frequency on either side of the center frequency until the amplitude reaches

$\frac{1}{\sqrt{2}} A$ as indicated in Fig. 1.

Similar definitions are possible in terms of the phase versus frequency curves. The half power points correspond, for a Lorentzian line, to the 45° and 135° phase shift points. In fact, the phase is ultimately used in the present work to define the linewidth because the phase measurement can be made more accurately than the amplitude determination. This is discussed below in the section on experimental technique.

The cavity has several types of resonances or modes, each being an independent solution to the equations of motion and the cavity boundary conditions. The relative contributions of viscosity and thermal conductivity to the linewidth are different for each mode. Thus, measurement of two modes allows the transport properties to be separately determined. The cavity dimensions determine the frequency at which each mode is appreciably excited. Thus, as we increase frequency the various modes

rise to a maximum and fall to zero within a few linewidths of their center frequency. A typical amplitude versus frequency plot is shown in Fig. 2. Any mode can be isolated by driving the cavity near the resonant frequency of the mode in question.

The first order expressions for sound speed and linewidth in terms of the gas properties are accurate to the order of $\left(\frac{\delta}{\omega_0}\right)^2$. The center frequency is

$$f_{ij} = \alpha_{ij} \frac{c}{2d} + \frac{\delta}{2} ij. \quad (3)$$

The linewidth is

$$\frac{\delta_{ij}}{f_{ij}^{1/2}} = a_{ij} \left(\frac{\eta}{\rho}\right)^{1/2} + b_{ij} \frac{\gamma-1}{P_r^{1/2}} + \delta_v f_{ij}^{1/2}. \quad (4)$$

Here the first subscript refers to the radial mode number and j refers to the longitudinal mode number.* The c is the sound speed, d the length

of the cavity, $\left(\frac{\eta}{\rho}\right)$ the kinematic viscosity, γ the specific heat ratio,

P_r the Prandtl number and δ_v the volume loss. The quantities, α_{ij} , a_{ij} and b_{ij} , are known quantities which depend on cavity geometry and the mode numbers. These constants as well as δ_v are given explicitly in Table 1. Typical linewidth and center frequency values are 120 Hz in 20 kHz at 1 atm, decreasing to 15 Hz in 30 kHz at 400 atm.

Equations (3) and (4) describe the losses due to dissipation in the cavity itself. Additional losses discussed in later sections occur due to the transducers and mode coupling. The cavity is designed so that the dissipation in the cavity itself is the dominant loss. The rest of this section is devoted to the accuracy of these two relationships.

* (jo) are the radial modes, (oj) are the longitudinal modes, and (ij) are compound modes. See Jack Bradshaw's thesis⁹ and Ref. 3 for more details.

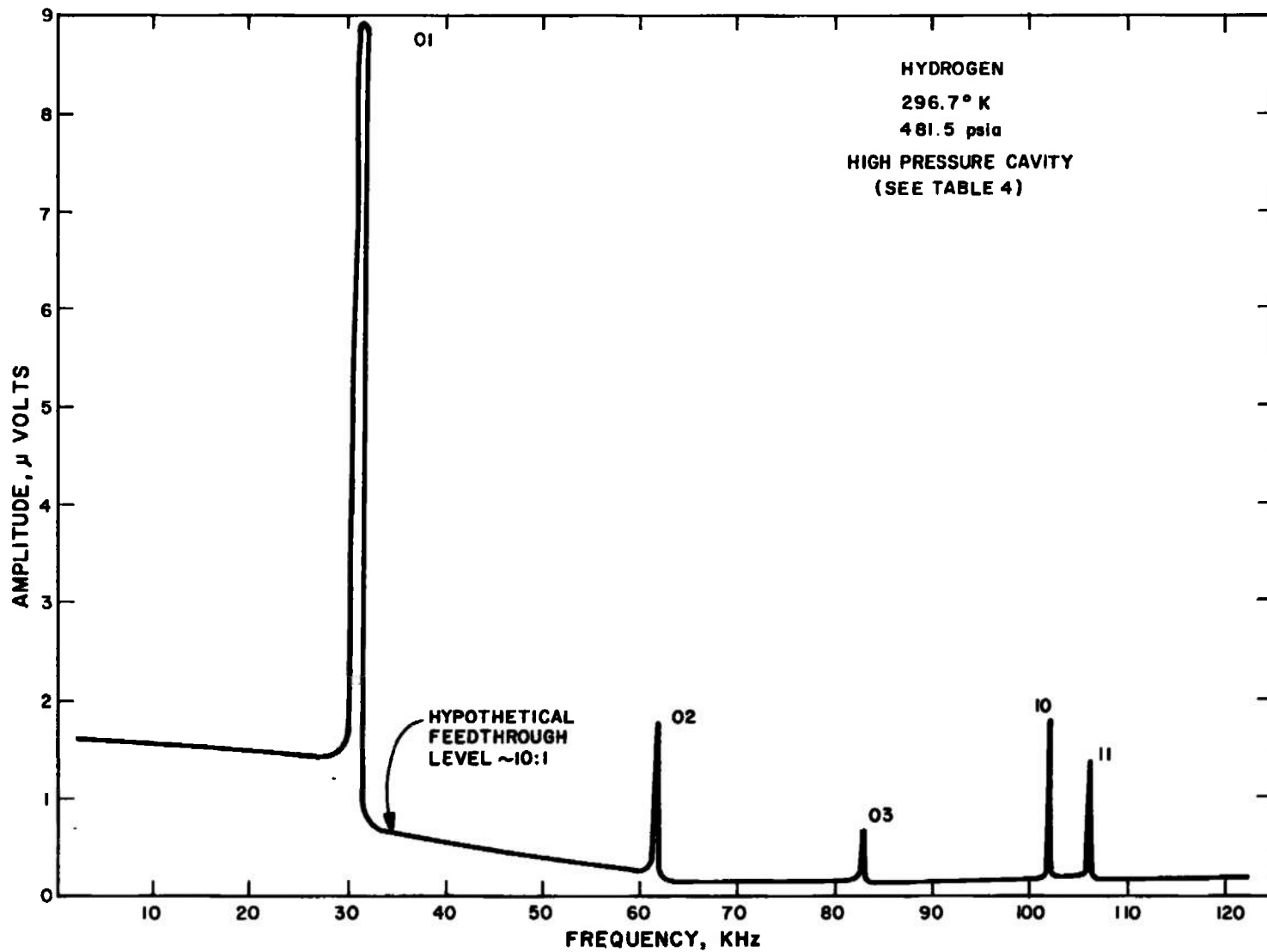


Fig. 2. Amplitude versus frequency response over several resonances.

Table 1. Constants for first approximation linewidths for symmetric modes in a cylindrical acoustic cavity.

Mode		
Longitudinal	Radial	Compound
$\alpha_{om} = m$	$\alpha_{no} = \frac{\gamma_n}{\pi R}$	$\alpha_{mn} = m \left[1 + \left(\frac{\gamma_n}{m \pi R} \right)^2 \right]^{1/2}$
$a_{om} = \frac{1}{\sqrt{\pi r^2}}$	$a_{no} = \frac{1}{\sqrt{\pi r^2}}$	$a_{nm} = \frac{\beta_{mn}^2 + 2(1 - \beta_{mn}^2) R}{\sqrt{\pi r^2}}$
$b_{om} = \frac{(1 + 2R)(\gamma - 1)}{\sqrt{\pi r^2}}$	$b_{no} = \frac{(1 + R)(\gamma - 1)}{\sqrt{\pi r^2}}$	$b_{mn} = \frac{(1 + 2R)(\gamma - 1)}{\sqrt{\pi r^2}}$

$$\delta_v = \frac{2\pi}{\rho c^2} \left[\frac{4}{3} \eta + \eta' + \frac{\gamma - 1}{P_r} \right]$$

r = cavity radius

d = cavity length

$$R = \frac{r}{d}$$

γ = specific heat ratio

γ_n = n'th root of first order Bessel function

$$\beta_{mn} = \frac{f_{no}}{\sqrt{f_{no}^2 + f_{om}^2}} = \frac{\gamma_n^2}{\sqrt{(m\pi R)^2 + \gamma_n^2}}$$

2.2 PHYSICAL BASIS OF CAVITY EQUATIONS

Following Thiesen¹⁰ and Fritsche^{11,12}, the exact equivalence of the conservation equations of fluid dynamics with a set of three wave equations was demonstrated in a previous report.³ These three wave equations describe the propagation of acoustic, viscous, and thermal waves.* These waves propagate independently of each other except at finite amplitudes and at discontinuities in elastic properties (such as the cavity walls). The boundary conditions on the cavity walls, continuity of temperature and strain, can only be satisfied if thermal and viscous waves are generated on the walls.

The boundary conditions on the walls of the cavity must be carefully evaluated. Application of the boundary conditions to the three wave equations is then only a formal problem. The idealized boundary conditions used by Fritsche assume that the wall has much greater capacity to absorb heat than the gas. Thus, the temperature fluctuations at the wall vanish. In addition, the wall is assumed to be much stiffer than the gas so that the particle velocity vanishes there. Due to velocity slip, thermal accommodation, finite wall thermal capacity and finite wall acoustic impedance, the particle velocity and fluctuating temperature do not vanish. These^{15,16} effects have been discussed for the lowest order traveling wave in a tube. Generalization of these wall effects to higher order traveling waves and to waves reflected from end walls is given in Appendix A below. However, mean free path effects, slip and accommodation require further discussion here.

The wavelengths λ_v and λ_t for the viscous and thermal waves, respectively, are given by³

$$\lambda_v = \sqrt{\frac{2\eta}{\rho\omega}} = \sqrt{P_r} \lambda_t. \quad (5)$$

The continuum theory might be expected to be in error in an amount roughly equal to the ratio of the wavelength to the mean free path squared since the theory includes first order deviations from equilibrium. A mean free path (L) can be defined by the zero pressure viscosity η_0 and the expression

*The viscous and thermal waves at the vortex and entropy are used in the theory of turbulence.^{13,14} The entropy wave is also responsible for the central peak of Brillouin scattered light.

$$L = \frac{\eta_o}{\rho c} \sqrt{\frac{\gamma}{3}} \quad (6)$$

Values of $\frac{\lambda}{L}$ for representative conditions (shown in Table 2) indicate that the continuum formulas for absorption (= linewidth) should be good to 10^4 .

Slip^{17,18} and accommodation^{19,20} are mean free path effects due to imperfect momentum and energy exchange within a few mean free paths of the wall. If the molecules were simply reflected like billiard balls the surface would look like a stationary layer of gas. The temperature of the wall, for instance, would simply be the value extrapolated from the temperature gradient in the wall. However, a certain fraction of the molecules stick to the wall before being reemitted into the hotter flowing gas. Thus, the gas in a layer a few mean free paths thick has a lower flow velocity and a higher temperature* than one would predict from the gradients by extrapolation to the wall. The size of this effect depends on the fraction of gas molecules which become attached to the wall. This is mathematically equivalent to (but not physically equal to) assigning a length l_v and l_t for the reflected molecules to adjust to the flow and temperature of the gas.

The effect of slip is to give a net flow velocity on the wall. The wall flow with slip is

$$U = l_v \frac{\partial U}{\partial r} \quad (7)$$

instead of $U = 0$. Similarly, the fluctuating component of temperature at the wall is

$$T = l_t \frac{\partial T}{\partial r} \quad (8)$$

instead of zero. The correction to the linewidth which results from slip and accommodation is the same as that in Table 1 with l_v and l_t in place of mean free path. Since l_v and l_t are a few mean free paths typically (and can be as much as $10L$) these corrections are somewhat greater than those given in Table 2. The measurements reported below were taken

*The temperature is somewhat lower for a negative temperature gradient.

Table 2. Ratio of mean free path to viscous wavelength for nitrogen under typical pressure-temperature and frequency conditions.

PRESSURE ATM		10 kc Temperature		100 kc Temperature	
		300	1000	300	1000
		0.1	2.3×10^{-2}	4.92×10^{-1}	4.00×10^{-2}
10	2.20×10^{-3}	$2/11 \times 10^{-3}$	3.81×10^{-3}	3.65×10^{-3}	
500	6.47×10^{-6}	1.71×10^{-5}	1.12×10^{-5}	2.96×10^{-5}	

under frequency, pressure and temperature conditions where slip and accommodation coefficients contribute less than 1 pt to 10^2 to the viscosity and thermal conductivity. However, under the assumption that the theory for slip and accommodation corrections given in Appendix A is good to 10%, it is possible to correct measurements of transport properties to 1 pt in 10^4 for densities between 10-100 amagats.

The losses to the side walls and end walls due to acoustic transmission into the cavity walls give rise to a linewidth component Δ_{np} which must be added to Eq. (4) to get the total cavity linewidth. It is difficult to calculate this effect exactly since the type of acoustic motion excited in the cavity walls can be very complex. Nevertheless, as shown in Appendix A, the linewidth due to acoustic transmission is proportional to frequency and the ratio of the acoustic impedance of the gas (ρc) to the acoustic impedance of the cavity walls ($\rho_w c_w$).

The acoustic transmission linewidth is

$$\Delta_{np} = \left[\alpha_s f + \alpha_E \sqrt{f^2 - f_{no}^2} \right] \frac{\rho c}{\rho_w c_w} \quad (9)$$

where α_s and α_E are constants for each cavity.* In addition, α_s and α_E are approximately equal to $\frac{1}{\pi}$ for the present cavities. The acoustic impedance ratio varies from $\sim 10^{-5}$ at 1 atm to 10^{-3} at 100 atm for the steel cavities used in the present work. Note the acoustic transmission losses to the end wall goes to zero for a radial resonance. This is because the wave number $k_p(1)$ goes to zero at a radial resonance and there is no axial particle motion to couple to the wall.

In practice, α_s is determined by measuring more than one radial mode in the cavity of interest. The difference between the total linewidth/(frequency)^{1/2} then provides α_s . Similarly, α_E can be measured by the same technique using more than one longitudinal mode. Notice that α_s and α_E do not depend on the gas so that a self-consistent check is obtained from measurements in different gases.

The linewidth component Δ_{np} can be obtained to $\sim 0.5\%$ in the present experiment. Thus, an uncertainty due to Δ_{np} of typically 1 pt in 10^5 in viscosity at 1 atm becomes 1 pt in 10^3 at 100 atm and increases to 3 pts in 10^3

*This assumes that there are no resonances in the cavity walls at the operating frequencies.

at 500 atm. There are several ways to reduce the size of the acoustic transmission loss which we have not had time to realize. For instance, high density and modulus material such as tungsten can be used for cavity construction. In addition, radial compound modes and especially asymmetric modes⁷ can be employed instead of longitudinal modes. Finally, large cavities can be used to accentuate the transport property losses (which vary as $\frac{1}{\sqrt{d}}$) compared to the acoustic transmission losses (which vary as $\frac{1}{d}$).

The losses calculated from the linewidth expressions given above are somewhat larger than the real dissipation in the cavity. The wave equation cannot be separated exactly into radial wave functions due to the corners of the cavity. For instance, when a traveling wave which satisfies the side wall boundary conditions exactly is incident on the end wall a new set of viscous and thermal waves is required (A. 56) to satisfy the end wall conditions. These waves are assumed to propagate 10^{-3} cm or less away from the cavity wall. The waves originating on the end wall lying near the corner give rise to unbalanced temperature and normal velocity on the side wall. Similarly, the viscous and thermal waves originating from those portions of the side wall near an end wall (A. 50) cause similar unbalanced temperatures and velocities on the end wall.

Expansions of cavity wave functions can be used to satisfy the boundary conditions more exactly. Radial wave functions may be used to satisfy the end wall boundary conditions and longitudinal mode wave functions may be used to provide a suitable expansion from the side wall boundary conditions. A similar problem arises for acoustic resonances in a finite cylindrical solid resonator when one tries to satisfy shear and normal stress boundary conditions.^{21, 22}

A good approximation can be obtained by noting that the corners must be temperature and velocity nodes. In addition, the troublesome

waves vanish roughly as $e^{-k_i r}$ or $e^{-k_i z}$, ($i = 2, 3$), for the end wall and side wall misfits, respectively. Thus, we can assume that in the final solution the energy density (E) must be a function of distance along the wall instead of constant (as assumed in Appendix A). On the side

wall the viscous wave amplitude must fall off as $e^{-|k_2 z|}$ with distance from the end wall. Similar relations hold for the thermal waves and on the end walls for both types of waves. Integrating the reduced energy density over the wall area a correction factor for viscosity

$$1 - 4 \left(\frac{2\eta}{\rho \omega} \right)^{1/2} \left(\frac{1}{d} + \frac{2}{r} \right)$$

and thermal conductivity

$$1 - \frac{4}{\sqrt{Pr}} \left(\frac{2\eta}{\rho\omega} \right)^{1/2} \left(\frac{1}{d} + \frac{2}{r} \right)$$

are obtained. The correction factors were always less than 1 pt in 10^3 in the present work and were neglected.

SECTION III

CORRECTIONS TO BASIC CAVITY THEORY DUE TO TRANSDUCER
COUPLING AND ELECTRICAL FEEDTHROUGH

3.1 EFFECTS OF COUPLING HOLE TRANSMISSION LINES

The linewidth of a resonance is a measure of how fast energy leaks out of the standing wave trapped in the acoustic cavity. The total linewidth consists of the "natural" linewidth due to dissipation of energy through thermal conduction and viscous friction (discussed in Section II plus additional linewidth due to energy transmitted out of the cavity. For instance, in a completely closed cavity the transmission loss to the finite acoustic impedance of the end wall is ~ 0.01 cycles at 1 atm and increases to 1 cycle at 100 atm.

Similarly, when the transducers are used to couple sound in and out of the cavity there are additional linewidth components due to energy which propagate into the transducers. The phase shift due to the transit of sound from the electrical drive to the cavity on the transmit side and a similar phase shift on the receive side add to the resonance phase shift in the signal. In addition, the electrical signal used to drive the transducers can take a path through the cavity walls or directly by electromagnetic pickup. We measure the phase versus frequency to obtain linewidth. The phase shift due to each of these effects give rise to an effective linewidth component which must be processed out to obtain transport properties.

The relative size and sign of each of the above linewidth components are displayed in Table 3 for the type of cavities employed in the present experiments. An examination of Table 3 indicates that the hole size of 0.004" or smaller is desirable* at elevated pressures. In addition, accurate calculation of correction factors due to the hole is necessary to provide accurate absolute viscosity and thermal conductivity measurements. The sound was coupled into the cavity through small holes in the present work. Although the corrections for the hole in the cavity are difficult to calculate (for a 0.1-0.01% linewidth measurement), this coupling technique has many practical advantages over other possible transducers.

*However, hole sizes greater than 0.008" were used in the present work. Future work should include the development of smaller coupling hole transducers.

Table 3. Typical linewidth components (argon 300°K) for the first longitudinal mode.

Pressure	Hole diameter	Natural linewidth	Hole loss linewidth	Transducer phase shift
		δ_o	δ_a	δ_h
1	0.013	119	2	
	0.004		0.05	0.5
100	0.013	12.5	27	2
	0.004		0.1	0.3
500	0.013	9.5	27	2
	0.004		2	0.3

The losses to the transducer in the present case consist of several terms. In general, the acoustic impedance of the coupling hole terminated by the electrostatic transducer could be calculated in the usual way.^{23, 24} The reflection coefficient so generated could be put into the usual formulas for linewidth of a transmission line (which the cavity is) terminated by the impedance of coupling holes. However, we have found detailed tracing of multiple reflections much simpler to use in the present case. This is particularly true when it comes time to see which physical parameters are significant to sort out approximations and to calculate second order terms.

The increase in linewidth due to the traveling wave multiple reflections depends only on the complex reflection coefficients (R) calculated in Appendix C. These reflection coefficients include the loss of energy due to the excitation of other modes during each reflection. The contribution of these other modes is considered in Section 3. 3. The coupled modes behave like feedthrough provided the cavity modes are separated by 10 linewidths. Finally, the additional phase shift due to multiple reflections in the coupling holes is given in Appendix B.

The total signal received can be calculated by adding up the multiple reflections of the various waves trapped in each of the three sections of the cavity. As shown in Appendix B the total receive signal is

$$C_f = A_o F_1 T_1 \cdot FT \cdot T_2 F_2 \cdot \quad (10)$$

Here A_o is the amplitude generated by the vibration of the drive transducer. F_1 and F_2 are the response coefficients which result from adding up all multiple reflections in the transmit hole (F_1) and the receive coupling hole (F_2) given by Eq. (B. 1). T_1 and T_2 are the traveling wave transmission coefficients from the transmit coupling hole into the cavity T_1 and from the cavity into the coupling hole on the transmit side T_2 . The reflection coefficients, R_{11} and R_{22} , as well as T_1 and T_2 (see Eq. (B. 1)), are calculated from the equations in Appendix C. The additional reflection coefficients, R_{00} and R_{33} , acquired to calculate F_1 and F_2 , respectively, are taken as unity. More exact values for these reflection coefficients have been calculated from the theory of electrostatic transducers.²⁵ Measurements of linewidth with the transducers reversed were made, since an undefined constant is present in the transducer theory.

Only the phase of the quantity $F_1 T_1, T_2 F_2$ is needed to calculate the effect of phase shift in the coupling hole. This phase shift is always less than $\sim 25^\circ$ in the present experiment because the first resonance in F_1 or F_2 occurs at 3 to 10 times the operating frequency for the cavity modes employed in the present measurement. The change in coupling hole phase shift (ϕ_h) is always less than 2.5° over a typical linewidth. This is because the Q of the coupling hole is always less than one-tenth of the cavity Q . The effective linewidth of this correction is

$$\delta_h = \frac{\phi_h}{\pi} \quad (11)$$

This is the quantity listed under transducer phase shift correction in Table 3.

3.2 EFFECTS OF COUPLING HOLE REFLECTION COEFFICIENTS

The largest correction due to the coupling holes is contained in (F) itself. Considering the end walls perfectly reflecting except for the losses to the coupling holes and mode coupling, the linewidth due to the coupling hole can be written

$$\delta_{pn} = \frac{2 f_{on}}{n \pi} \frac{1 - r_{pn}^2}{1 + r_{pn}^2} \quad (12)$$

where f_{on} is the resonant frequency of the n th longitudinal mode and r is the reflection coefficient amplitude from Appendix C. This linewidth may be simply added to the other linewidth components described above.

The linewidth due to the coupling hole represented by

$$\delta_a = G(pn) \left(\frac{r_o}{a} \right)^2 \omega \quad (13)$$

where $G(pn)$ is a constant for each mode, r_o is the coupling hole radius, and a the cavity radius. The loss component δ_a represents the energy simply propagated into the hole.²⁶

A second component of the δ_{pn} arises from the complex parts of the wave numbers as described in Appendix C. This linewidth component

$$\delta_b = - \left[g_\eta (pn) + g_\lambda (pn) \frac{\gamma - p}{P_r^{1/2}} \right] \left(\frac{\eta \omega}{\rho} \right)^{1/2} \quad (14)$$

is dependent on the Prandtl number and the viscosity. Here, $g_\eta (pn)$ and $g_\lambda (pn)$ are constants for each mode which are considered to be additional factors in the desired cavity response. Thus, the hole correction is only δ_a (see below).

3.3 MODE COUPLING EFFECTS

The reflection coefficients of Appendix C account only partially for the energy lost to mode coupling. In fact, pressure carried by these other modes does reach the receive transducer. However, if the modes are well separated the additional signal due to mode coupling varies only slowly and looks like a form of feedthrough.

There are experimental precautions one takes to avoid mode coupling. First, the overall coupling between transducer and cavity is reduced as much as possible consistent with signal-to-noise considerations. Second, the symmetry of the transducer is chosen to favor the desired modes. For instance, an electrostatic transducer covering the entire face of the cavity employed in the present work excites the first 20 longitudinal modes, preferentially with radial and asymmetric modes down by at least 40 dB (a factor of 100). Similarly, a small centrally located transducer excites longitudinal, radial and compound modes, the asymmetric mode being undetectable (40 dB down). Finally, the ratio of cavity length to diameter is chosen for maximum frequency separation between modes. However, after all precautions have been taken one is typically left with a mode coupling phase shift equivalent to ~ 0.5 to 0.05% of the linewidth. Thus, to realize the accuracy inherent in the cavity technique a mode coupling correction is necessary.

The response of a cavity can be calculated in great detail by considering multiple reflections of the cylindrical wave guide traveling waves of Appendix A from the cavity end walls. Initially, the transducer excites many modes according to the transmitter coupling coefficient t_m^n for each radial mode ϕ_n as indicated in Appendix C. When the frequency of the driving transducer excitation is near the resonant frequency of the s th mode, the amplitude of the resonant mode is $\sim Q t_m^s$. All the other modes are $\sim t_m^n$ in amplitude. Each time the wave system reflects from one of the end walls, reflection, transmission and mode conversion

occurs. The amount of each wave generated depends on the reflection coefficient R_s^s and the coupling coefficient R_n^s of the transducers involved.

The calculation of the mode coupled signal is similar to the derivation in Appendix B. A right going wave

$$\bar{\phi}_s = \psi_m t_m^s e^{i(\omega t + k_s^{(1)} z)} \quad (15)$$

is introduced by the transmitter. Here ϕ_s is the radial wave function for the resonant wave in question. The transmitted wave bounces back and forth between the end walls of the cavity. These multiple reflections give rise to a total right going wave for the resonant mode on the receive wall

$$\phi_{s+} = \frac{t_s \psi_m}{1 - (R_s^s)^2 e^{2ik_s^{(1)} d}}$$

All the singly mode converted waves ϕ_{n+} arising from the reflection of ϕ_s from the receive transducer

$$\phi_{n+} = \phi_{s+} R_s^n$$

waves which undergo multiple mode conversions are proportional to higher order powers of the coupling coefficients. Since the coupling coefficients are small, these higher order terms are neglected. A similar contribution of singularly mode converted waves is generated by reflections from the transmit coupling hole. Thus, the total mode converted wave source strength in the n th radial mode is

$$\phi_n = \psi_m t_m^n + 2 \psi_m t_m^s R_s^n f \left[1 + e^{2ik_n^{(1)} d} \right]. \quad (16)$$

The first term is simple transmission into the cavity from the transmit coupling hole. This term gives rise to an acoustic feedthrough which contributes less than $\frac{2}{Q}$ of the total received signal at the half power points, where Q is the cavity quality factor $\left(\frac{\omega_0}{\delta} \right)$. This feedthrough-like component is processed out of the data as described in Section 3.4.

The second term in Eq. (16) is not mentioned in the literature. However, since it is proportional to the resonant mode response function F_s , it can dominate the mode coupling effects. The total signal received due in the presence of mode coupling* is

$$C_f = A_o F_s \left[F_1 T_{1.} T_{.2} F_2 + \sum_{n \neq s} T_{1.} R_s^n F_n T_{.2} \left(1 + e^{ik_n^{(1)} d} \right) \right]. \quad (17)$$

The second term in brackets represents the mode coupling contribution and is about 10^{-2} of the first term. When the modes are well separated the mode coupling term does not depend on frequency because we are in the wings of F_n . Thus, the major effect of the mode coupling term is to add a system phase shift. The system phase shifts are removed by the iterative determination of center frequency and phase shift at center frequency. Nevertheless, more accurate calculation of the phase shift due to mode coupling is possible using the coupling and transmission coefficients from Appendix C, although this was not done with the data reported below.

3.4 FEEDTHROUGH ROUTINES FOR DATA REDUCTION

Summarizing the last three sections, accurate determination of natural line shape, that is, phase and amplitude versus frequency for a given resonance, requires elimination of competing phase shift and amplitude variations. The effects of various components on the measured phase and amplitude can be more clearly understood by reference to a diagram of the experimental apparatus (Fig. 3). A frequency synthesizer is used to generate a reference signal for the lock-in amplifier and a driving signal for the resonant cavity. Between the synthesizer and the cavity, a line amplifier is adjusted to give enough output to drive the transmitted transducer. The output of the transmit transducer enters the cavity through a coupling hole and stimulates sound waves. The amplitude of the sound field in the cavity is sensed through a second coupling hole, and is picked up by the receive transducer. The output of the receiver is fed into a tuned amplifier to increase the signal-to-noise ratio. Finally, the lock-in amplifier provides the signals necessary to determine the amplitude of the signal and the phase of the signal with respect to the

* $T_{1.}$ has been used in place of t_m^s for simplicity. It should be borne in mind that $T_{1.}$ and $T_{.2}$ depend on radial mode number. For the modes used in the present work all modes above $m = 0$ in the coupling hole are below cutoff and contribute a negligible amount of signal.

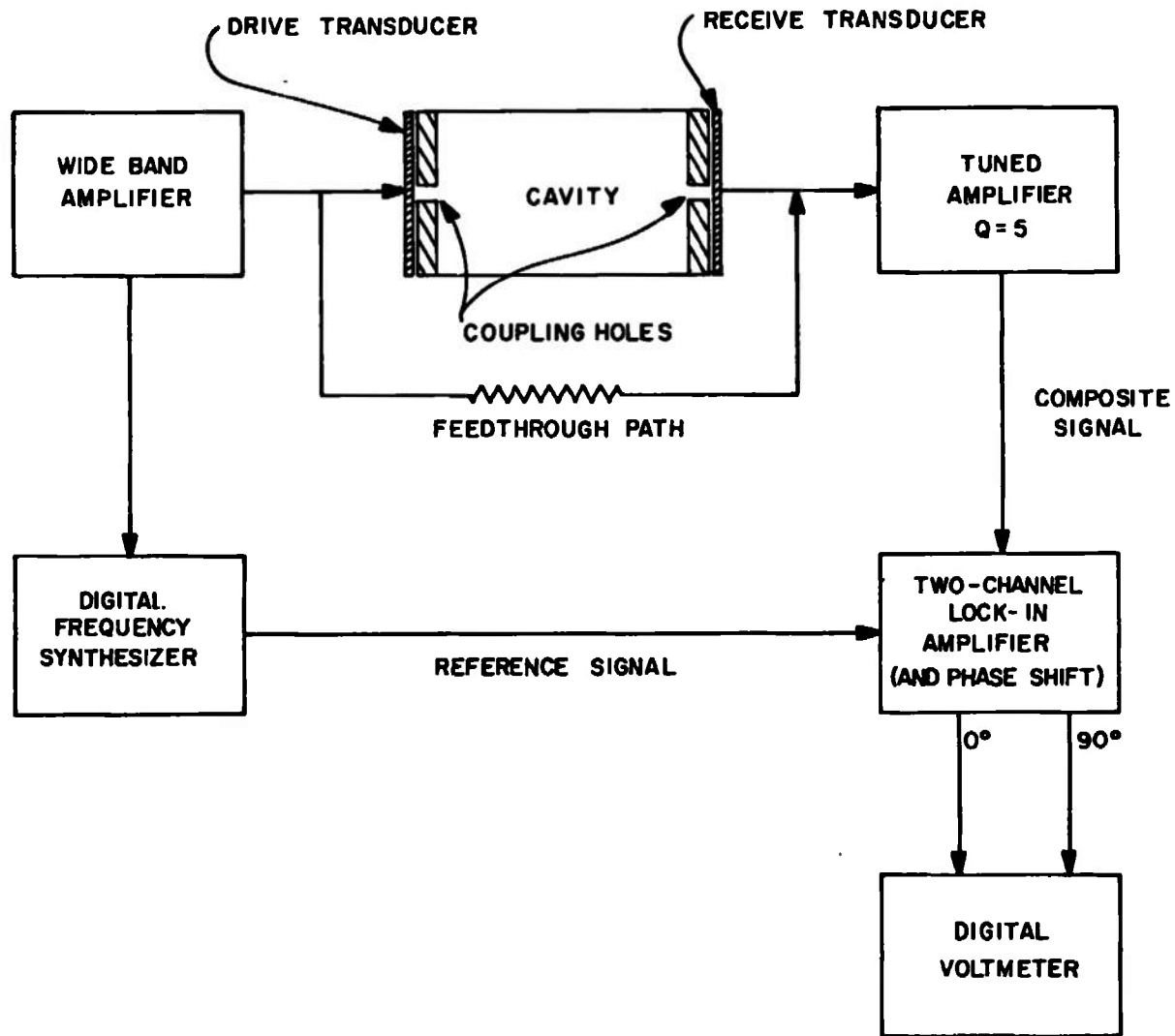


Fig. 3. Signal paths for resonant cavity transport and thermodynamic property measurements.

electrical driving voltage. The amplitude information is read out on a digital voltmeter. The phase is measured either on a phase shift dial in the reference channel or preferably as in-phase and out of phase components of amplitude on a digital voltmeter.

The major objective of the data reduction discussed here is the elimination of the systematic phase shift and feedthrough. The phase shift due to all signal components other than those due to the resonant cavity has to be eliminated in order to determine the true cavity linewidth and line shape. Systematic phase shift is introduced by the following elements of the apparatus: The frequency synthesizer, line amplifier, coupling holes, tuned amplifier, and distributed RC's. All these component phase shifts are in series and add up numerically. In addition, the amplitude variations with frequency due to elements in the signal path can be corrected by multiplication by a frequency dependent numerical factor.

A second set of interfering signals are the acoustic and electrical feedthroughs "around" the cavity. The feedthrough signal path is parallel to the signal path indicated in Fig. 3 by the imaginary resistor connected between the transmit and receive transducer terminals. There is electrical feedthrough, acoustic feedthrough through the cavity walls, and acoustic feedthrough on modes* other than the resonant mode in the gas itself. The feedthrough adds vectorially with the cavity signal. Therefore, in-phase and out of phase components of the composite measurement must be found and corrected for parallel feedthrough.

Information about the feedthrough is contained mainly in the wings ($|\omega - \omega_0| > \text{linewidth}$) of the resonance line. The signal amplitude in the wings depends mainly on the distance from the center frequency; therefore the resonance signal phase and amplitude in the wings can be calculated from a rough knowledge of ω_0 . The vector difference between the calculated resonance signal and the measured composite signal in the wings can then be interpreted as the feedthrough. This feedthrough can then be vectorially subtracted from the measured composite signal within one linewidth of ω_0 to obtain a refined value of ω_0 and linewidth δ . One can repeat this procedure to obtain successively better estimates of feedthrough and resonance signal. Most of the time the feedthrough is less than 5% of the signal and one iteration is sufficient to obtain ω_0 and δ to within the uncertainty of the measurement (see Fig. 2).

*Note that the resonant mode is built up by a factor of Q (~ 100) compared to a mode whose center frequency is far from the operating frequency.

The measured phase at maximum amplitude is an easily identifiable point on the resonance curve. The phase shift due to the resonance at this frequency is 90° . The systematic phase shift may then be eliminated by subtracting the phase shift at ω_o from each measured phase and adding 90° . In the presence of feedthrough, electrical or acoustic, the maximum amplitude frequency is, in general, the least affected characteristic of the resonance curve.

There is an optimum way to use information about amplitude to obtain the approximate resonant frequency and linewidth. The signal-to-noise is best at maximum amplitude. However, the amplitude is not sensitive at ω_o changes in frequency. The amplitude at the half power frequencies is more sensitive to frequency changes. Therefore, two amplitudes on either side of the maximum amplitude are used to estimate the resonant frequency (\sim maximum amplitude frequency).

Working relations can be derived once the line shape is known. Assuming the line is Lorentzian, the measured amplitude should vary with frequency as

$$A^2 = \frac{A_o^2 \delta^2}{(\omega - \omega_o)^2 + \delta^2} \quad (18)$$

where

$$\begin{aligned} A &= \text{amplitude} \\ \omega &= \text{frequency} \\ A_o &= \text{maximum amplitude} \\ \omega_o &= \text{center frequency} \\ \delta &= \text{half width} \end{aligned}$$

The half width (δ) may be determined from points near the half power frequencies of the line in question (i. e., $0.707 A_o$ pts) from each side of the center. Putting the amplitudes and corresponding frequencies of these two points in Eq. (18), we can solve for δ , obtaining

$$\delta = \frac{\omega_+ - \omega_-}{\left[\left(\frac{A_o}{A_+} \right)^2 - 1 \right]^{1/2} + \left[\left(\frac{A_o}{A_-} \right)^2 - 1 \right]^{1/2}} \quad (19a)$$

where plus and minus signs refer to either side of the center. Recalling that the amplitude is not sensitive to frequency change right near the center, we can use δ and A_o to approximate ω_o

$$\omega_o = \frac{\omega_+ - \omega_-}{2} - \frac{\delta}{2} \left\{ \left[\left(\frac{A_o}{A_+} \right)^2 - 1 \right]^{1/2} - \left[\left(\frac{A_o}{A_-} \right)^2 - 1 \right]^{1/2} \right\} \quad (19b)$$

The first approximation to the phase at maximum frequency is then the measured phase ϕ_{ω_o} at ω_o .

The system phase shift is in ϕ_{ω_o} as well as all the cavity signal phase shifts. Subtracting ϕ_{ω_o} from each measured phase shift eliminates the system phase shift. In fact, adding 90° to this phase difference, the phase between the pressure incident on the cavity and that transmitted through the cavity is obtained. This resonance phase shift is calculated in radians from

$$\phi = (\phi_L - \phi_{\omega_o} + 90) \times \frac{\pi}{180} \quad (20)$$

where ϕ_L = listed (measured phase angle) data

ϕ_{ω_o} = resonance phase angle interpolated to ω_o from nearby measured phases ϕ_1 and ϕ_2

i. e.,
$$\phi_{\omega_o} = \phi_1 + \frac{\phi_2 - \phi_1}{\omega_2 - \omega_1} (\omega_1 - \omega_o).$$

The systematic phase shift is not entirely independent of frequency. Frequency variation of phase shift is small over a linewidth, therefore, it is adequate to calculate the difference between phase at ω_o and phase at every other frequency theoretically. The small phase variation which does rise is subtracted from the phase data point by point.

The largest mechanical phase shift is that due to multiple reflection of the sound waves between the foil side of the coupling hole and the cavity. The phase shift due to transit through the coupling holes is the ϕ_h of Eq. (11).

In general, the electronic coupling and isolation are carefully designed to minimize RC phase shifts. However, a certain amount of bandpass filtering is required to optimize the accuracy of the phase and amplitude measurements. A tuned amplifier with a Q_a of 5 is used in the measurements to date. The amplifier is set at the maximum amplitude frequency and the measured phases at other frequencies are corrected. The phase shift due to the tuned amplifier is

$$\Delta\phi_t = \tan^{-1} \frac{\frac{\omega}{\omega_0} - \frac{\omega_0}{\omega}}{Q_a} \quad (21)$$

A similar correction to the amplitudes is also possible, but not usually important. Therefore we have considered only series phase shifts. Series phase shifts simply add to the desired resonance phase. Acoustical and electrical feedthroughs pass through channels parallel to the desired signal channel. Therefore, the feedthrough must be vectorially subtracted from the signal to obtain the resonance curves. We must be concerned with electrical feedthrough by direct electrical radiation from the transmit transducer to the receive transducer, acoustical feedthrough around the cavity walls and mode coupling signals through the gas path itself. Electrical feedthrough is frequency independent. However, the phase of the acoustical feedthrough will vary by about $\left(\pi \frac{\delta}{\omega_0}\right)$ or typically 2° over the range of frequencies of interest for a given mode.

A phase diagram* showing the various components which make up the composite signal (Fig. 4a) is helpful in understanding the method of separating series and parallel signal components. The lower phase diagram shows how the tip of the receive pressure vector traces a circle counterclockwise as the frequency increases. The ω_0 point is offset from 90° by the amount ϕ_0 due to the transit time in the coupling holes. The zero phase point was chosen to be the phase of the electrical signal and the driving transducer. The electrical feedthrough in these coordinates has a phase of zero degrees. The phase angle of the acoustic feedthrough via the cavity walls can be determined from the sound speed in the wall material and l_h the effective feedthrough path. The wall feedthrough has a phase of about 18° for the 001 mode in the present cavities. The acoustic feedthrough carried on nonresonant modes similarly has a phase somewhat

*Phase diagrams from measured modes are shown in our previous report, Ref. 3.

greater than 180° for frequencies near the 001 mode. Both acoustic feedthrough signals have phase variations of about 1% over a linewidth. The limits of the phase variations of the acoustic feedthrough are shown in Fig. 4b by the dotted line vectors. In addition, the acoustic feedthrough vectors increase phase as the drive frequency is increased. Thus, the composite feedthrough can be expected to have any phase between $0-720^\circ$ for lines used in the present experiment.*

The typical composite feedthrough vector for the 001 mode is shown in Fig. 4b. Also shown is the cavity signal vectors at $\omega - \omega_0$ and at the half power frequencies. All these vectors are shown as dotted lines. In addition, the reference phase has been shifted in accordance with the system phase shift. The solid lines show the measured composite signal which is the sum of the feedthrough and the signal.

The measured center frequency is pulled to frequencies slightly higher than the true cavity center frequency. A feedthrough vector at 30° instead of the 160° phase shown in Fig. 4a would lower the measured center frequency. The maximum pulling of the center frequency occurs for phases of 0 or 180° . The center frequency is pulled at most an amount equal to the feedthrough amplitude divided by maximum signal amplitude times the linewidth. Notice there is no effect on center frequency for feedthrough vectors with phases of 90° or 270° . Similar remarks hold for the linewidth. Generally, the feedthrough causes less than 5% broadening (or narrowing) of the linewidth and shifts center frequency by less than 5 Hz. The frequency dependent phase shifts lead to $\sim 0.5\%$ effects.

The feedthrough is determined from a few measurements ($\sim 10 \delta$) far from the center frequency and on either side of the line. Only two measurements on the line wings are required to obtain feedthrough. However, several points are measured for a few lines when a new transducer or cavity is introduced. The multiple measurements in the line wings are spot checks on the assumption of a linear frequency dependence of feedthrough, phase and amplitude.

The line shape due to the cavity resonance cannot be approximated by a Lorentzian line shape in the wings as is indicated in the final paragraphs

*Most of the lines used for data acquisition in the present effort are below the third longitudinal. The acoustic feedthrough vector, in general, can be $n360$ if the highest mode used in on.

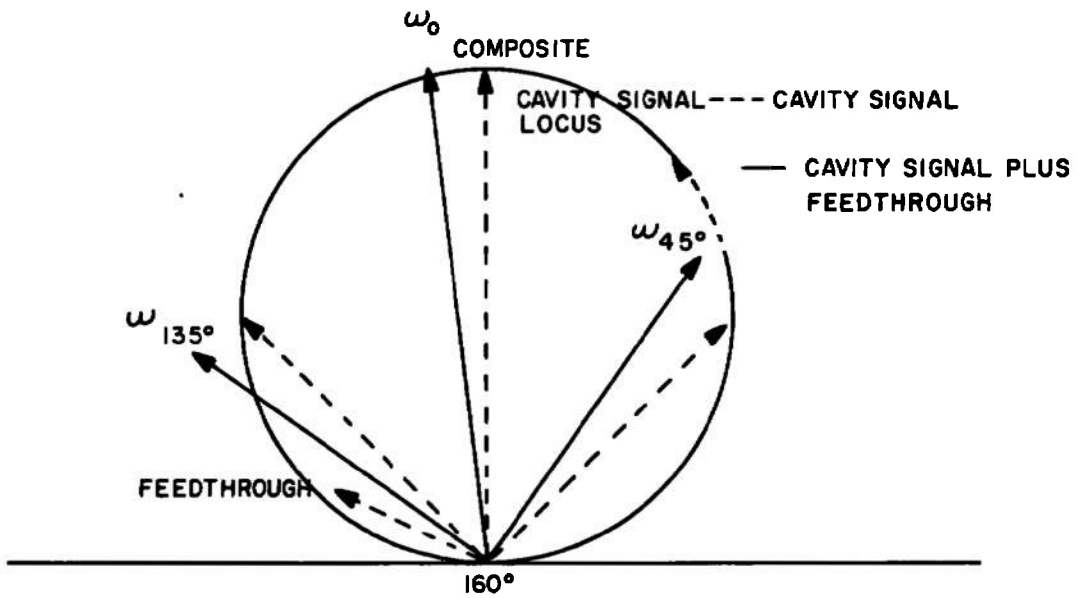


Fig. 4a. Composite measured signal polar diagram.

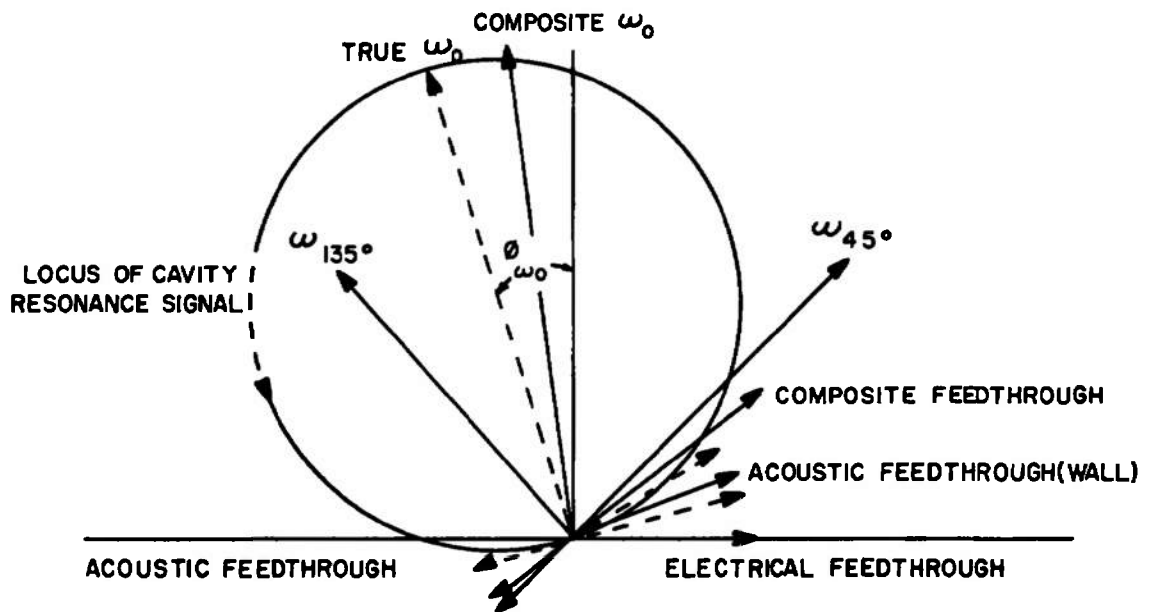


Fig. 4b. Vector diagram for various components in cavity output.

of Appendix A. The resonance signal drops to about $\frac{1}{Q}$ of its maximum value A_o and then varies slowly with frequency. The signal due to the cavity resonance and the feedthrough is usually of the same order of magnitude in the line wings. The electronic feedthrough \bar{V}_f is therefore the vector difference between the measured amplitude vector A and the vector due to the resonance

$$\bar{V}_f = (A \cos \phi - A_s \cos \phi_s) + j (A \sin \phi - A_s \sin \phi_s) \quad (22)$$

where A is the measured amplitude and ϕ the measured phase.* The signal due to the cavity resonance A_s and the associated phase shift ϕ_s are calculated in the first iteration from ω_o and δ from Eqs. (19a) and (19b. "Exact" natural line shapes are given for our cavity in Appendix A. An expression valid in the line wings where $|\omega - \omega_o| \gg \delta$ and sufficiently accurate for the present purposes is for the mode (pn)

$$\bar{V}_s = \frac{A_o \frac{n \pi \delta}{\omega_{on}} \sqrt{\frac{\omega + \omega_{po}}{\omega_{on}}}}{\sin n \pi \cdot \sqrt{\frac{\omega^2 - \omega_{po}^2}{\omega_{on}^2}} + j \frac{n \pi \delta}{\omega_{on}} \sqrt{\frac{\omega + \omega_{po}}{\omega_{on}}}} \quad (23)$$

where ω_{po} is the pth radial mode center frequency, ω_{on} is the nth longitudinal mode center frequency, δ the linewidth from Eq. (19a). For the longitudinal modes $\omega_{po} = 0$ and ω_{on} is obtained from Eq. (19b). For the radial modes $n = 1$ and ω_{po} is obtained from Eq. (19b) and measurement on the pth radial mode in question. The nth radial and pth longitudinal mode center frequencies are used with the measured δ for compound modes (pn). The phase ϕ_s is just the ratio of the imaginary to real parts of the denominator of Eq. (23).

The feedthrough program calculates A_s and ϕ_s from Eq. (23). The true feedthrough is then obtained by putting line wing data and A_s and ϕ_s into Eq. (22). This feedthrough signal is then used to correct the amplitude and phase of the composite signal measured near the half power points. The corrected phase versus frequency near the half power points then provides the true linewidth and center frequency of the cavity resonance.

*Corrected for systematic phase shifts to the first approximation.

3.5 SUMMARY DATA REDUCTION PROCEDURE

The greater part of Section 3 has been devoted to those contributions to the measured line shape which must be removed to obtain accurate (0.1%) gas properties from the cavity technique. The first problem is to eliminate feedthrough the systematic phase shifts. The initial phase shift is set equal to zero at the apparent maximum amplitude point with a reference phase shifter. A rough value of the line-width δ and the center frequency ω_0 is obtained from Eqs. (19a) and (19b), neglecting feedthrough. The rough values of δ and ω are then put in Eq. (24) to give the signal A_s in the wings. The feedthrough is then given by

$$\frac{\bar{A}}{A_0} - \frac{A_s}{A_0} = \frac{R}{A_0} + i \frac{I}{A_0} \quad (24)$$

where \bar{A} is the complex amplitude data in the wings, A_s is the signal in the wing and A_0 is the maximum voltage amplitude. R and I are the real and imaginary parts of the feedthrough.

The feedthrough is assumed to vary linearly with frequency and the data in the wings is used in Eq. (25) to obtain the feedthrough constants r_0 , r_1 , j_0 and j_1 . These are

$$\frac{R}{A_0} = r = r_0 + r_1 \omega \quad (25)$$

and

$$\frac{I}{A_0} = j = j_0 + ij_1 \omega. \quad (26)$$

Linear frequency dependence means that the feedthrough consists of electrical pickup plus acoustic feedthrough with no feedthrough resonances.

Once the feedthrough constants are obtained a better value of δ and ω_0 are obtained from the data within 2δ of ω . The second approximation to ω_0 and δ is obtained by fitting the equation

$$\omega = \delta (|a|^2 - 1)^{1/2} + \omega_0 \quad (27)$$

to the data. The quantity a is then defined by

$$a = \frac{\bar{A}}{A_0} - r + ij = \frac{\delta}{\omega - \omega_0 + i\delta} \quad (28)$$

and Eq. (27) follows from the assumption that the line shape is Lorentzian within 2δ of ω_0 . The variable ω is fit to a linear function of $(|a|^2 - 1)^{1/2}$. This process is repeated until consistent values of δ and ω_0 are obtained.

For large feedthrough amplitudes, $\sqrt{\frac{R^2 + I^2}{A_0^2}} \gtrsim 0.3$, the phase shift (ϕ_0)

at ω_0 must be readjusted after the first iteration using the improved estimate of ω_0 and the ϕ versus ω data. Most of the time two or three iterations with no ϕ_0 adjustment are required.

The feedthrough constants are then used to correct the original data. That is, r is subtracted from the in-phase signal component and j from the out-of-phase signal component point by point. Thus $\cot \phi$ at each data point within 2δ is then found from the ratio of imaginary to real parts of the feedthrough corrected signal.

The final step consists of making a fit of the measured frequencies to a linear function of $\cot \phi$

$$\omega = \delta \cot \phi + \omega_0. \quad (29)$$

The raw linewidth δ and center frequency ω_0 data are the constants of this fit.

The coupling hole corrections are then applied to the linewidth, subtracting δa (Section 3.2) and correcting for ϕ (Section 3.1). The acoustic transmission losses Δ_{np} (p. 14) are subtracted. The resulting linewidth contains only information on viscosity and thermal conductivity. This linewidth may be identified with the δ_{ij} of Eq. (4), plus the correction factors g_η and g_λ from Eq. (14).

The sound speed is then obtained from $\omega_0 = 2\pi f_0$ and Eq. (3). The sound speed defined by Eq. (3) is shown in Appendix A to be the real part of $\frac{\omega}{k_1}$. Since the internal modes (not including chemical degrees of freedom) do not affect the isothermal compressibility (K_T)

$$\rho K_T = \frac{1}{ZRT} \left[1 + \frac{\rho}{Z} \left(\frac{\partial Z}{\partial \rho} \right)_T \right] \quad (30)$$

the real part of $\bar{\gamma}$ is obtained from

$$\gamma_R = \frac{1}{1 + \frac{\rho}{Z} \left(\frac{\partial Z}{\partial \rho} \right)_T} \frac{c^2}{2ZRT} \quad (31)$$

Here Z is the compressibility factor from pvt measurements, ρ is the density, T the temperature, and R the ideal gas constant. The real part of γ_R is precisely the quantity needed to determine the Prandtl number from the linewidth. However, the specific heat at constant pressure is necessary to obtain the thermal conductivity from the Prandtl number. As long as the imaginary part of $\bar{\gamma}$ is small this specific heat is given by

$$C_P = \frac{\left[1 + \frac{T}{Z} \left(\frac{\partial Z}{\partial T} \right)_P \right]^2 c^2}{T (\gamma_R - 1)} \quad (32)$$

This approximation was used for all the thermal conductivity data of the present report.

Specific modes must be chosen to show how the transport properties are obtained from the linewidths. The expressions for the linewidths for different modes are obtained by putting the appropriate radial and longitudinal mode numbers into Eq. (4). For convenience, the normalized radial, compound, and longitudinal linewidth

$$\delta_R = \frac{\delta_{10}}{f_{10}^{1/2}}, \quad \delta_c = \frac{\delta_{11}}{f_{11}^{1/2}}, \quad \delta_L = \frac{\delta_{01}}{f_{01}^{1/2}}$$

respectively, are introduced. One can eliminate viscosity in favor of Prandtl number (P_r) using the longitudinal and compound mode linewidths* to get

$$\frac{\gamma_R^{-1}}{P_r^{1/2}} = \frac{\frac{\delta_R}{\delta_c} \left[1 - g_\eta(01) \right] - R' \left[1 + g_\eta(10) \right]}{(1 + R') \left[1 + g_\lambda(10) \right] - (1 + 2R) \frac{\gamma_R^{-1}}{P_r^{1/2}} \left[1 + g_\lambda(01) \right]} \frac{\delta_R}{\delta_L} \quad (33)$$

*See Section 3.2 for definition of g_η and g_λ .

Similar equations for $\frac{\gamma_{R^{-1}}}{P_r^{1/2}}$ can be obtained from the 01 and 11 or 11 and 10 modes. The value of the coupling hole radius is varied around its nominal value until the parameter $\frac{\gamma_{R^{-1}}}{P_r^{1/2}}$ is self-consistent. The hole correction δa and the parameter g_η and g_λ are functions of a .

Once a consistent value of Prandtl number is obtained the viscosity can be calculated from any of the measured linewidths. In particular, the viscosity can be calculated from the longitudinal linewidth using

$$\frac{\pi \eta}{\rho}^{1/2} = \frac{\pi r \delta_L}{R' \left[1 + g_\eta(01) \right] + (1 + R') \frac{\gamma_{R^{-1}}}{P_r^{1/2}} \left[1 + g_\lambda(01) \right]} \tag{34}$$

Notice that the Prandtl number does not depend on the density. All the effects of density in Eq. (33) are in measured quantities. Since it is simple to determine the required linewidth under identical pressure-volume-temperature conditions, the consistency of $\frac{\gamma_{R^{-1}}}{P_r^{1/2}}$ was chosen to

correct the hole radius. The viscosity, on the other hand, depends on the density. The density is determined from the measured pressure and the measured temperature and available pressure-volume-temperature, Refs. 26-29, in the present work. (The pressure measurement is the weakest link of the present work. The pressures were measured to ~0.1%.) There are many other ways in which the self-consistency of redundant cavity measurements can be used to check the various correction terms. However, only the consistency of the Prandtl number was used in the present work.

The reader has undoubtedly come to the conclusion at this point that there is a lot of arithmetic between the measurement and the desired properties with the cavity technique. However, the cavity measurement provides the same information obtained from simultaneous parallel plate thermal conductivity measurements,³⁰ oscillating disk measurements,^{31, 32} plus a Joule Thompson³³ measurement. In addition, the acoustic cavity can supply relaxation time measurements.³⁴ The response of the cavity can be calculated in much greater detail than the response of the above conventional measurements. Also, the difficult problem of measuring small temperature and pressure changes is bypassed. Therefore, the working equations and the type of measurements required are simpler for the cavity technique than for any other set of measurements one might envision to measure the same quantities.

SECTION IV

EXPERIMENTAL APPARATUS AND RESULTS

4.1 SUMMARY OF EXPERIMENTAL PROBLEMS WITH GAS-FILLED ACOUSTIC CAVITIES

There has been a great deal of effort expended on resonant acoustic cavities for the measurement of properties of gases.^{35, 12, 36} Usually, resonators dimensionally large compared to the cavities of the present work, were used. The small dimensions of the present cavities were chosen originally to make the cavity linewidth large, ~200 Hz. This made the stability requirements on the frequency realistic. For instance, to measure a 200 Hz linewidth to 0.01% directly requires 0.02 Hz frequency determination in ~20 kHz. An additional reason for using small cavities is to minimize the volume of material which must be maintained under constant high temperature and high pressure conditions.

However, previous work has employed large cavities due to the difficulty of eliminating acoustic feedthrough via the solid walls of the cavity. Several approaches to this problem have been used by ourselves and other workers. Magnetically driven pistons,³⁶ flexural ceramic transducers,³⁵ membrane coupled transducers and several other transduction³⁷ schemes have been used to couple more efficiently to the gas than to the walls. Isolation of the cavity walls can be accomplished by mounting the transducers on soft members³⁸ such as O-rings and minimizing the mechanical contact between the transducer and the cavity walls. Fritsche¹² used the fact that flexure of a thin membrane provided good isolation between the transducer and the cavity walls. Following Fritsche, we expended a great deal of effort during the initial part of the present work to realize a small membrane isolated transducer such as is shown in Fig. 5a. However, the small size of the required transducer dimensions meant that a small diameter membrane had to be used. The decreased diameter led to stiffening of the flexure and consequently acoustic feedthrough and membrane resonances.

Nevertheless, our experience indicated that membrane flexure was the most promising isolation technique. Therefore, electrostatic transducers³⁹ were tried. These transducers were mounted facing the cavity with no tension on the dielectric membrane. The elastic compliance of these transducers was due to a central vent in the transducer backup and the gas trapped between the backup and the transducer membrane. These transducers are isolated to a level below our detection capabilities. They have a uniform, flat response, between 5 kc-250 kc.

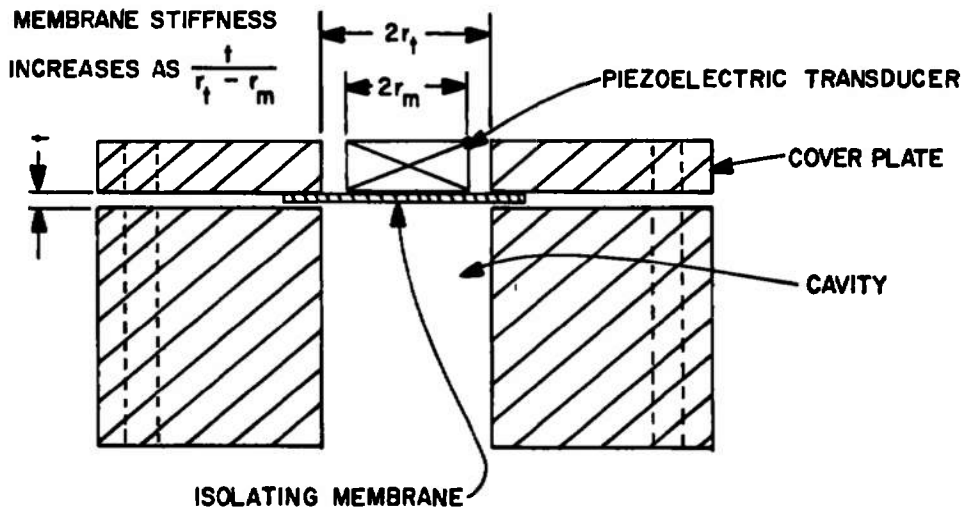
That is, they do not introduce additional resonances themselves. However, the end wall impedance is difficult to control and/or calculate when mounted facing the cavity as shown in Fig. 5b. This problem was solved by isolating the transducer from the cavity with a solid end wall containing a small coupling hole. Although the calculation of the losses of energy from the cavity into the coupling hole is involved, it can be carried out with great precision. In addition, the end wall impedance can be varied by simply changing the size of the coupling hole.

Finally, the electronic readout of the phase and amplitude versus frequency must be done in sufficient detail to eliminate interference from feedthrough and thermal drift. Also, problems with resonances in the transducer and cavity walls can be detected only from detailed line shape measurement. The first technique used consisted of setting several frequency points around a resonance and measuring the phase and amplitude at each point. The most serious problem with this approach is that the frequency must be stable over the period of the measurement, typically to 0.02 Hz in 20 kHz (1 pt in 10^7). A factor of three variation in center frequency is necessary to make a measurement with the cavity technique. Therefore, parts in 10^7 stability is difficult to achieve. The proliferation of digital frequency synthesizers during the past two years has solved this problem.

However, one is left with thermal drift of the cavity center frequency due to the temperature dependence of sound speed. The precise calibration of phase shift to 0.01% is also difficult. Several modulation techniques were developed in which two waves spaced $\omega_m \sim \delta$ apart and centered on a frequency equal to the center frequency of the mode in question were simultaneously sent through the cavity. Finding the half power (450 points) was reduced to varying ω_m until a null was observed. The 90° phase shift was automatically assured by the theory of the modulation process. However, the modulation techniques were not suited to collecting sufficient information to process out interfering signals. Therefore, a line sweep was found necessary to determine feedthrough, etc. Then, additional measurements of the modulation techniques could also be used to obtain extremely precise (pts in 10^5) linewidth determinations. However, all the data in the present report were taken with the line sweep technique. The modulation device was used only to get a quadrature calibration for the phase-lock amplifiers.

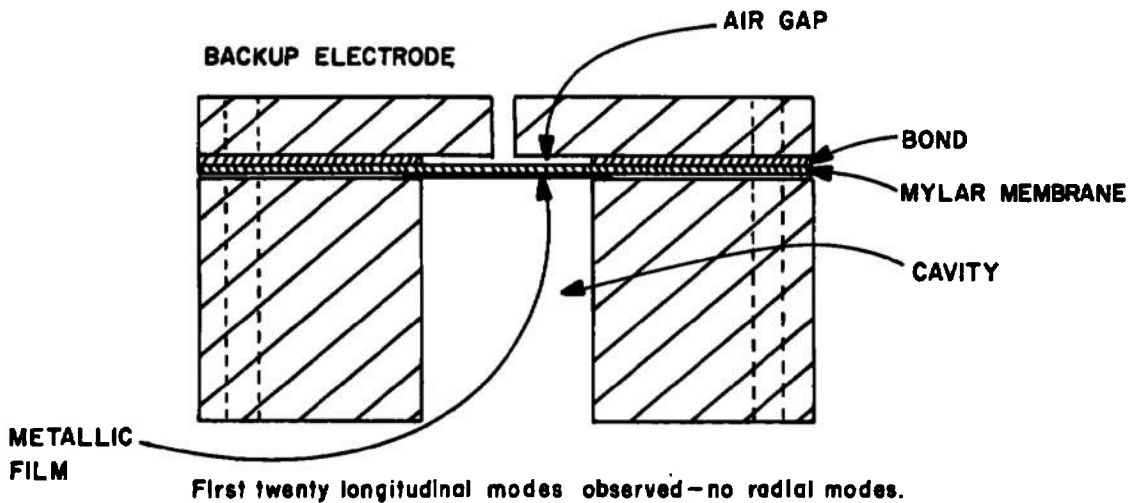
4.2 MECHANICAL HARDWARE

The cavity is mounted inside a pressure vessel. Most of the measurements were made in an Aminco pressure cell. The pressure cell had two thermocouple ports, two electrical feedthroughs, and a gas



No clean modes above first longitudinal (19000 KMz) obtained.

(a) MEMBRANE ISOLATION



(b) ELECTROSTATIC

Fig. 5. Techniques for exciting acoustic cavities with good wall isolation.

inlet and outlet. A thermistor was inserted through one of the thermocouple ports on all measurements below 400°K . Two high pressure gages 0-1500 and 0-7500 psia - Bourdon gages (Heise) - were mounted on one of the gas ports. A low pressure gage 0-100 (also Heise) and a mercury manometer were attached through a second port. The second port was used to load and evacuate the high pressure cell. The details are given in Fig. 6.

A second cell was set up for high temperature (700°K), high pressure (500 atm) operation. The cell material, Hastalloy C, was chosen specifically for high pressure-high temperature operation. The cell volume was minimized for safety. The cavity slip-fit into the pressure cell, as indicated in Fig. 7. The electrical signal lines were brought in through the 1/8 inch ID high pressure tubing. The high pressure lines from the cell are ~ 25 cm long and made of Hastalloy C. The high pressure electrical feedthroughs are made at low temperature on a high pressure tee at the end of the Hastalloy C high pressure lines. The gage, vacuum and source connections were common to the first cell.

A high temperature quartz oven was used for measurements in nitrogen and air. In addition, elevated temperature measurements were made in atmospheric air with a cavity inside a heating element wrapped in insulating material. The quartz oven shown in Fig. 8 had a cavity mounted over three-quarters of the way down a 4 inch diameter quartz tube. The cavity was mechanically supported by two steel tubes which in turn were rigidly fastened to the steel end flange of the furnace. The electrical signals were brought into the oven through these steel tubes in quartz tubing. The vacuum seal of the electrical lines and mechanical support for the cavity were accomplished at the cool oven end flange.

The 18 inch long quartz tube was immersed 14 inches into a furnace. The last 4 inches of the quartz tube was exposed to the room temperature air. The exposed parts of the quartz and the end flange were always sufficiently cool to touch. Four stainless steel baffles were placed along the length of the quartz oven to prevent radiation and convection. Since the quartz and steel pieces were only fastened together at one end no thermal expansion problems were encountered. However, the central steel wire conductor of the signal feedthroughs was coiled to avoid thermal expansion against the transducer membrane.

The sound speed was taken as the true measure of temperature in 1 atm high temperature measurements. However, thermocouples were inserted into a hole about halfway into the wall of the acoustic cavities. Unfortunately, it was not possible to measure temperature gradients in the walls of the cavity due to time limitations. However,

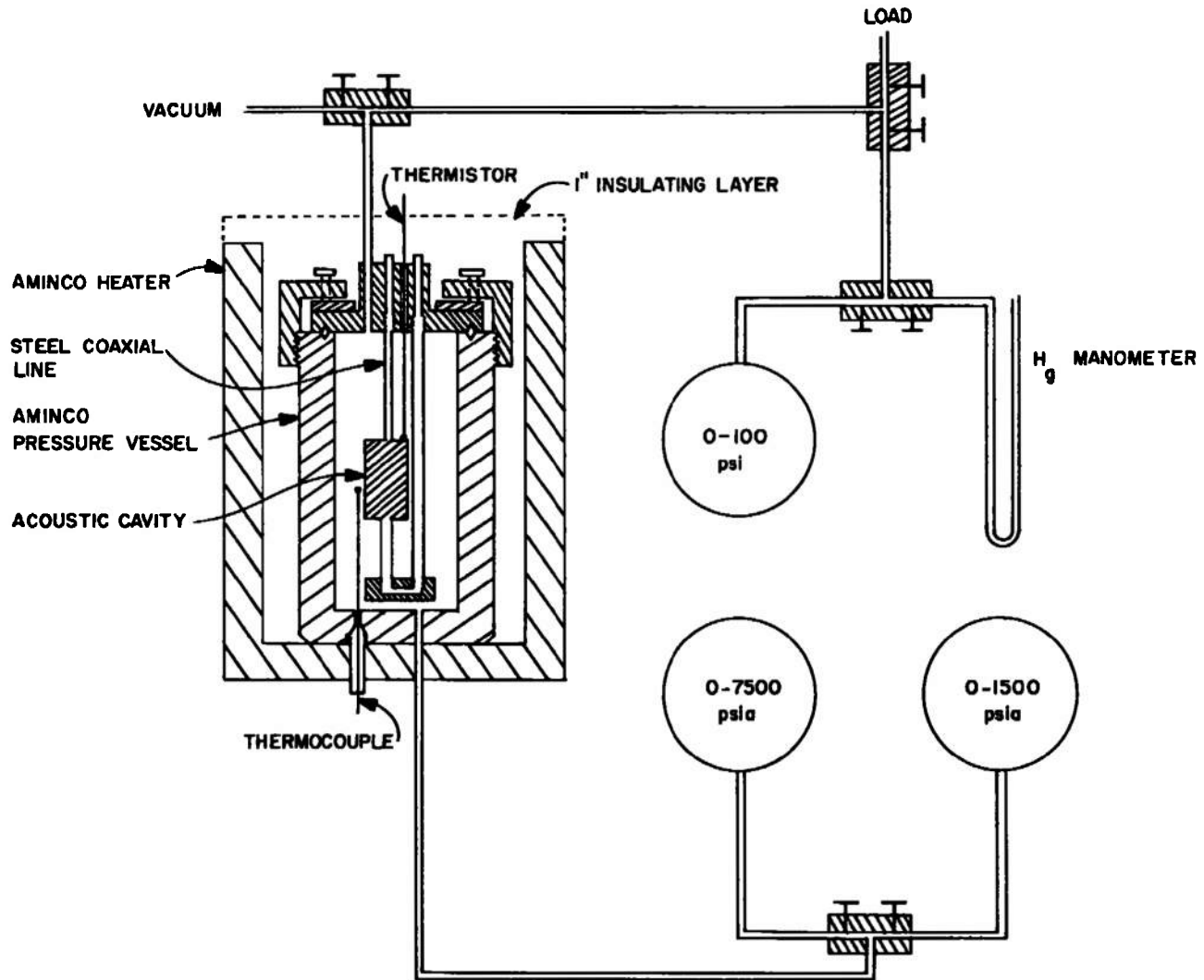


Fig. 6. Aminco high pressure cell and pvt equipment.

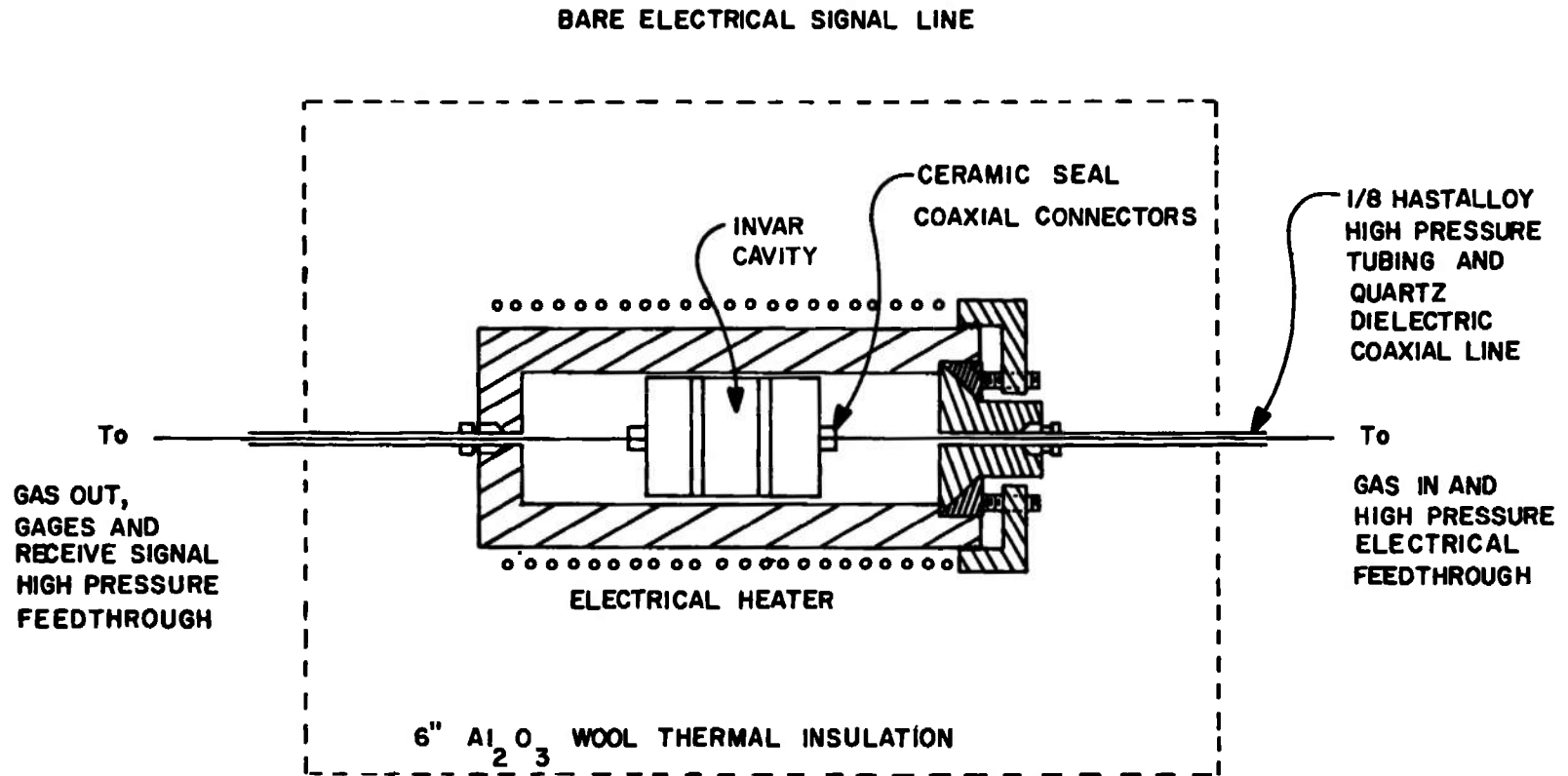


Fig. 7. Hastalloy high pressure cell for high pressure use.

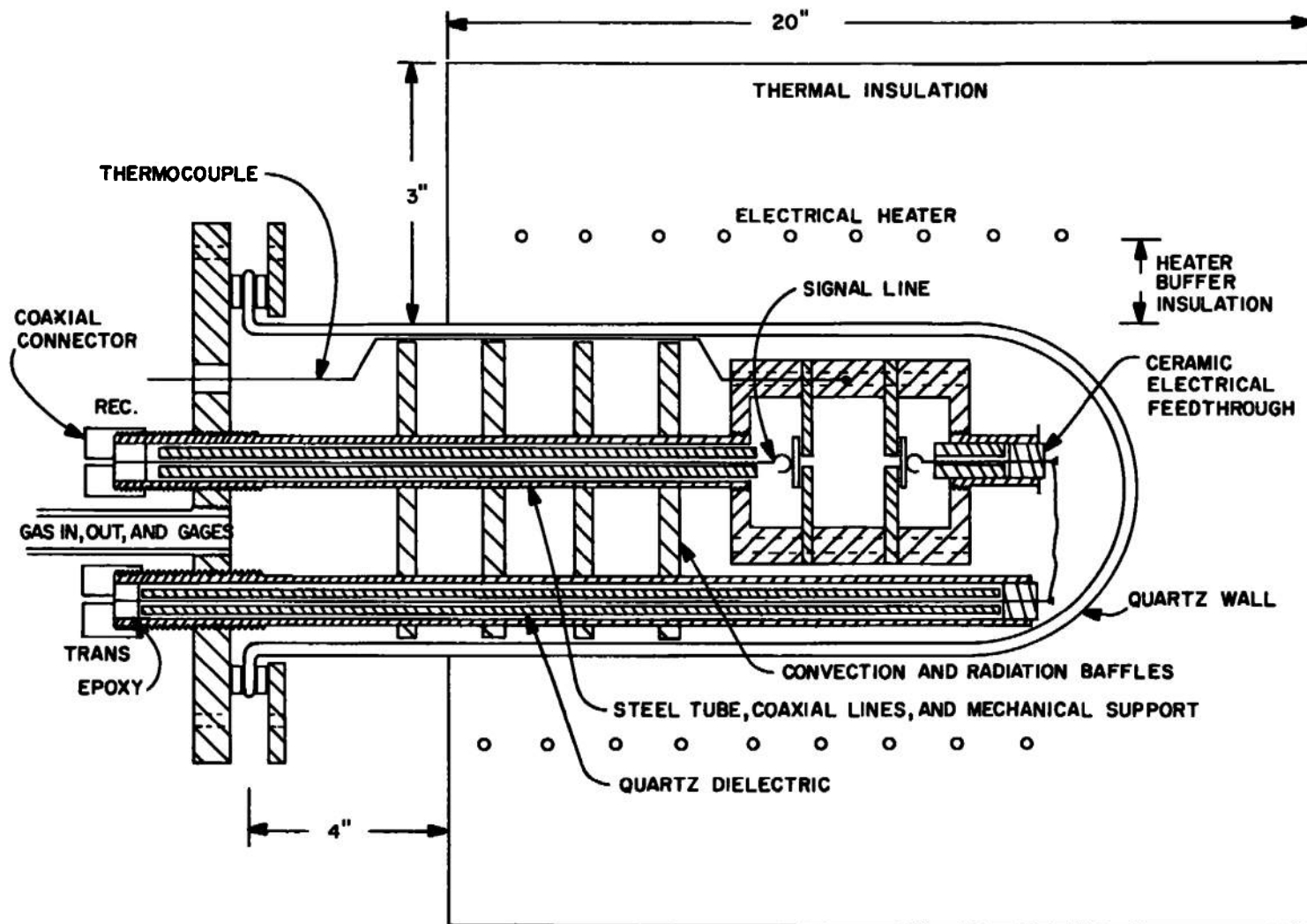


Fig. 8. Quartz oven for low pressure-high temperature use.

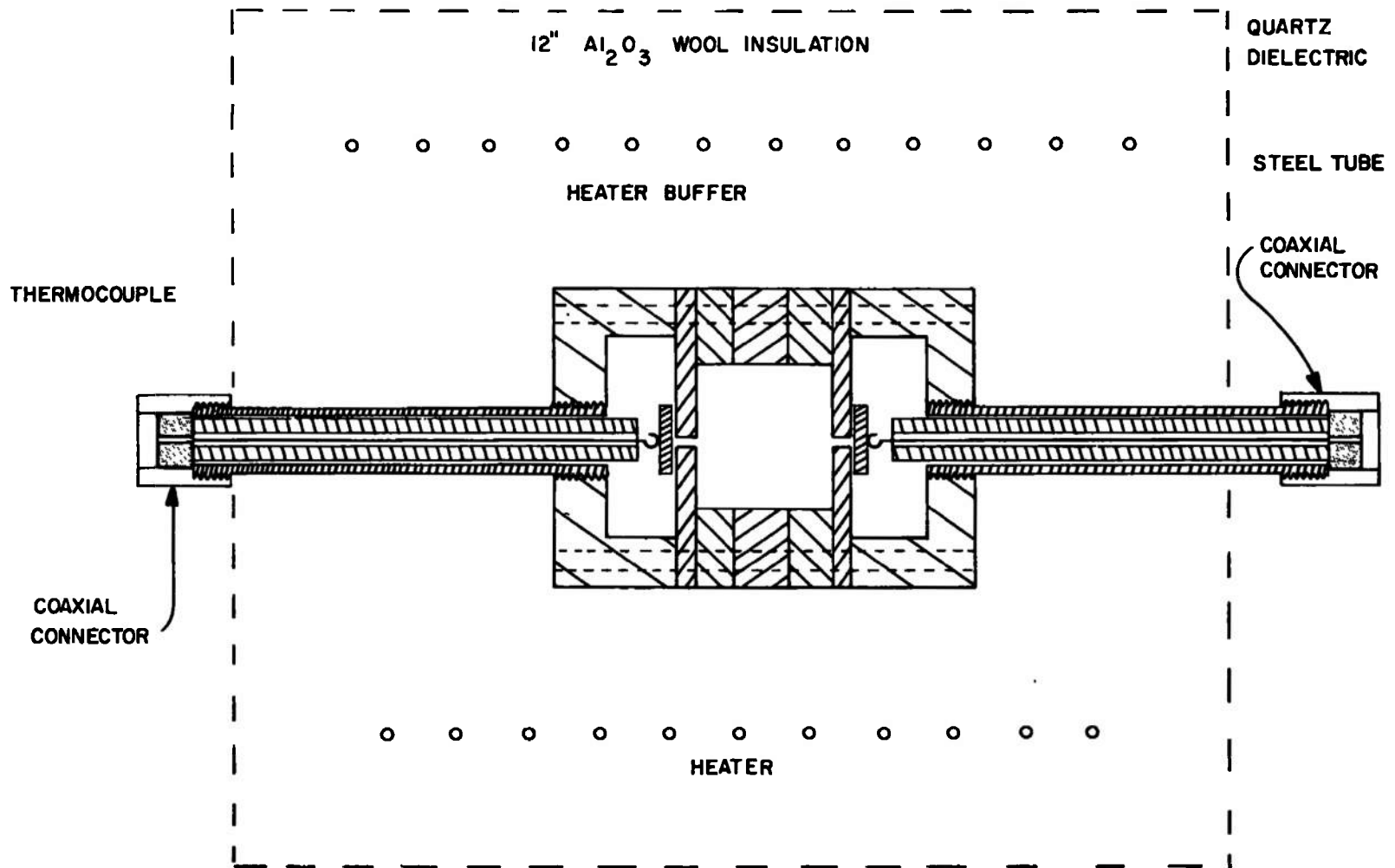
all the ovens built around the cavities had at least 2 inches of alumina cotton between the test volume, and the heating elements. In addition, at least 4 inches of similar insulating material was packed on either side of the heaters as indicated in Figs. 1 through 8. The construction was designed to minimize gradients and to stabilize the test zone against power fluctuations in the heater. In fact, all the ovens used required the better part of an 8-hour day to come to equilibrium. Equilibrium was judged by the lack of drift in the phase null at resonance. Temperature fluctuations of 1 pt in 10^6 could be detected* this way.

The quartz oven could be evacuated and filled with any desired gas. Mainly, nitrogen and air were investigated in the quartz oven. Air at atmospheric pressure was also investigated in the oven assembly shown in Fig. 9. This cavity always had a gas leak path to atmospheric air. In addition, the cavity body was segmented to allow the coupling hole correction to be studied for a given set of end plates on different length cavities. Discontinuities of up to 0.0001" may have existed between the radii of the various segments of the cavity plates. However, the data agree with the quartz cavity data to 0.5%. The temperature determinations in the segmented cavity were accomplished in a way identical to those used in the quartz ovens.

The acoustic cavity assemblies used during the present work were constructed in several radial pieces bolted together as in Fig. 10. The acoustic cavity itself is formed by the central cylindrical piece and the end plates. The gas is allowed to leak into the cavity between the end plates and the side walls. Thus, it is necessary to pull a vacuum on the cell or oven containing the cavity and load to a high pressure to obtain a pure test gas. A small radial scratch along the side wall was sufficient to assure good exchange of gas. Typically, three evacuation and load cycles were sufficient to assure a pure gas in the cavity. Purity of the gas was checked by comparing the sound speed at one atmosphere during two successive phases of the load cycle. In addition, the time required for the gas to leak into the cavity and come to thermal equilibrium with the cavity walls could be determined by monitoring the change of sound speed with time after a positive pressure change. Typically, impurity levels of 5 pts in 10^5 were observable and a 15-minute equilibrium time was measured.

The end plates were held onto a thick walled (greater than 1/4") cavity head by small screws to facilitate initial test and assembly of the

*Absence of drift implied temperature stability. However, the presence of drift could be due to several mechanisms.



57

Fig. 9. Cavity and furnace for measurements in atmospheric air.

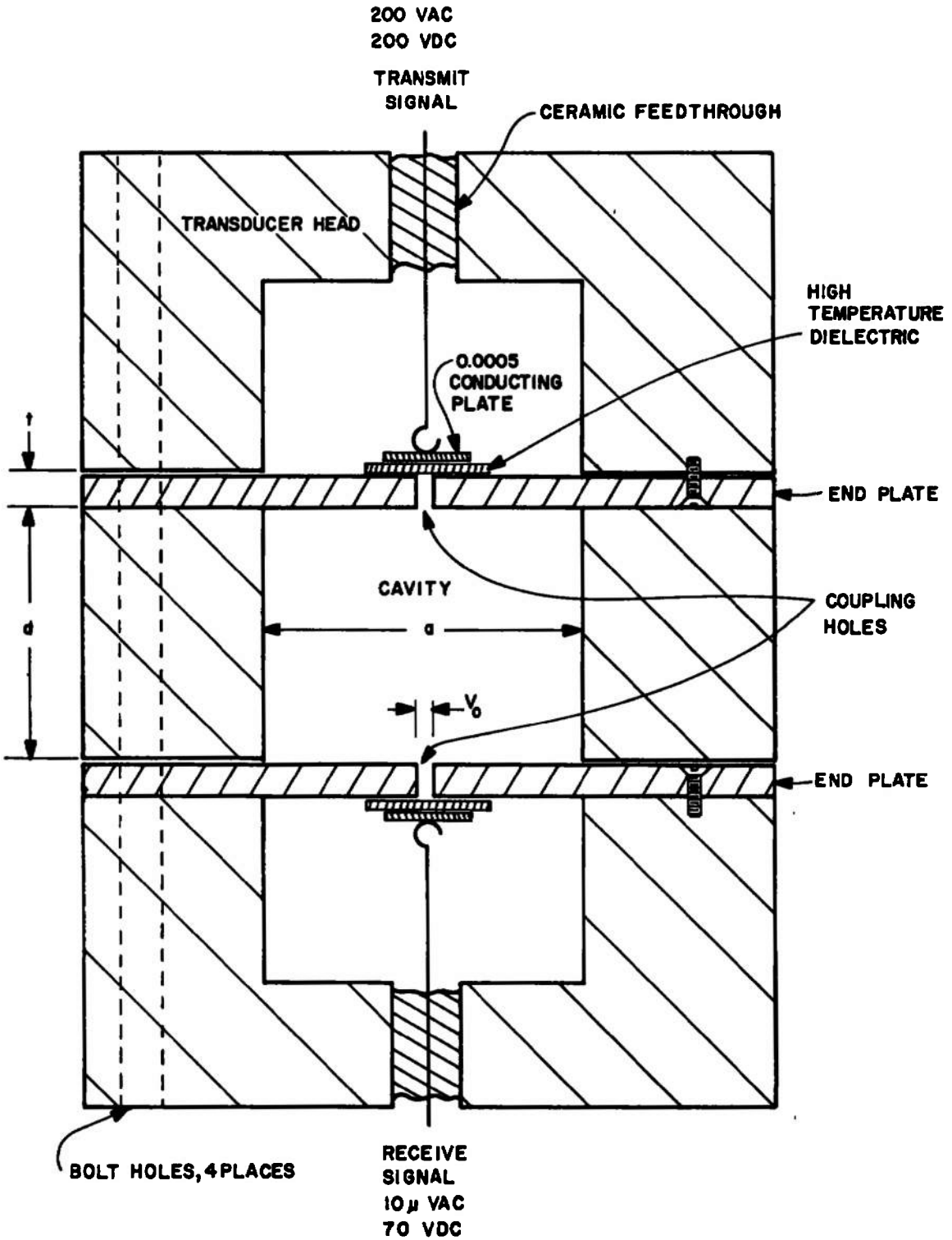


Fig. 10. Acoustic cavity and transducer.

transducers. Thick walled transducer heads were found necessary to reduce electrical pickup between the receive and transmit transducers. In addition, such construction minimized the possibility of any low frequency acoustic resonances in the head itself.

The end plates were made of the same material as the cavity body. The end plates were between 0.330 and 0.139 cm thick. Thinner end walls than ~ 0.1 cm had plate resonances.

The area of the end plate was ~ 2000 times the area of the coupling holes. Thus, plate resonances were extremely efficient in exciting sound in the cavity. Any sound introduced this way into the gas had plate resonances (Ref. 40, p. 213) and phase shifts superimposed on cavity resonances. End plate resonances become more troublesome at elevated temperatures because several factors conspire to drop the plate resonance frequencies as temperature increases. Large radius cavities (large end plate radius) must be used to maintain a sufficiently narrow linewidth at elevated temperatures. Also, as temperature increases the elastic modulus of the steel end plate drops. Thus, lowest frequency end plate resonance was designed to be ~ 80 kHz at room temperature (~ 1 cm radius cavity). A thick (~ 0.330 cm) plate was used with a thin (~ 0.139) plate to avoid simultaneous resonances in the two end walls.

Cavities with radii ranging from 1.26 cm down to 0.25 cm and radius to diameter ratios ranging between 0.1 and 1 were successfully employed in the present work. However, only five cavities were used to take the data presented below. The material and dimensions of these cavities are presented in Table 4. The thermal expansion of the cavity material is also shown in Table 4. The change in cavity dimensions due to thermal expansion between ~ 300 and 1000°K amounts to $\sim 1\%$. Measurement of the radial mode resonant frequency versus temperature in a gas such as argon at low density (~ 1 amagat) would suffice to determine cavity dimensions versus temperature to parts in 10^4 . However, available thermal expansion data⁴¹ was used to correct viscosity data. Recall in Section 3.5 that only the cavity dimensions enter the Prandtl number determination. Thus, the Prandtl number measurement (actually $\frac{\gamma-1}{P_r^{1/2}}$) is not dependent on thermal expansion.

The cavity dimensions and materials of the present study were chosen for flexibility in the face of a program calling for measurements over a wide range of pressures, temperatures and gases. Future work should employ cavities optimized for more specific areas of the pressure-temperature range. High acoustic impedance materials such as tungsten

Table 4. Material and dimensional characteristics of cavities used to measure data reported below.

Cavity and Test Volume	Radius cm	R'	Material	Thermal Expansion Coefficient
Precision (Aminco high pressure cell)	0.72896	0.81223	5200 steel	8.4×10^{-6} (0-400°K)
High pressure (Aminco high pressure cell)	0.72433	0.33621	302 Stainless steel	9.6×10^{-6} (0-400°K)
High temperature (quartz oven)	1.2584	0.81215	"	9.6×10^{-6} (0-400°K)
Segmented (open oven atmospheric air)	0.62808	0.78039 (varies with run)	Cold rolled steel 1018	8.4×10^{-6} (0-900°K)
High temperature, high pressure (Hastalloy pressure cell)	0.64255	0.37683	Invar	0.7×10^{-6} (300°K) 6.4×10^{-6} (600°K)

will reduce acoustic transmission losses by a factor of 5 or more for high density (greater than 100 amagats) measurements. Oxidation resistant nickel base superalloys can be used effectively for measurements in air and oxygen at temperatures up to $\sim 1000^{\circ}\text{K}$. Finally, the advent of digital frequency synthesizers at low frequencies together with tracking phase-lock amplifiers means that large cavities ($\sim 3''$) can be used without compromising electronic stability requirements. Larger cavities simplify the hole correction problem and allow high cavity Q to be obtained. Large cavities have advantages for low pressures (under 100 atm) and high temperature measurements. Nevertheless, any special optimization introduces problems. High ρc and oxidation resistant materials are difficult to procure and fabricate. Large cavities make thermal stability and uniformity problems more acute. In addition, large cavities pose difficult pressure cell design problems especially above $\sim 200^{\circ}\text{C}$. These are the basic considerations behind the mechanical design and the cavities for the present work.

4.3 TRANSDUCERS

The electrostatic transducers, shown in Fig. 10, consist of a flexible dielectric between a flexible conducting layer and the back side of the cavity end wall. A dc voltage between the cavity end plate (ground) and the flexible layer cause a compressive electrostatic force between the two conducting parts. An alternating signal superimposed on the dc field causes the electrostatic force to fluctuate. The dielectric then also vibrates, driving the trapped gas back and forth in the coupling hole. Similarly, a pressure wave in the coupling hole causes the dielectric film to vibrate. The resulting variations in capacitance of the electrostatic transducer causes an rf voltage to appear across the receive transducer.

In fact, the operation of the electrostatic transducers is considerably complicated by the formation of polarization⁴² in the dielectric. The dc bias gradually induces dipole states both on the surface of the dielectric and in the body of the dielectric layer. The polarization field opposes the bias field. As a result the signal of the new transducer falls off as a function of time. Different dielectrics show varying ability to polarize. Mylar and mica show 100% polarizability so that the signal would drop off to zero eventually. The teflon and quartz dielectrics show very little signal loss due to polarization. In addition, above a certain temperature, which we have called the depolarization, no permanent polarization is observed.

The time dependent polarization is a major problem just below the depolarization temperature because the amplitude change due to

depolarization is superimposed on changes due to thermal drift as well as those due to the resonance. There is also drift in the system phase shift since the space between the conducting plates increases, as the polarization field cancels the dc bias field, decreasing the transducer capacitance. Therefore, it is necessary to operate above or well below the depolarization temperature. A drift of $\sim 1\%$ in amplitude per hour was found to be tolerable.

Several materials were tried for the flexible parts of the electrostatic transducer. The results are summarized in Table 5. Our early work used mylar films as the dielectric. The mylar was available with an aluminum coating. A mylar transducer built up a polarization field at room temperature in a matter of minutes on the receive side after an ~ 100 dc bias was turned on. The receive side could then be operated without bias for several days before noticeable depolarization occurred. However, the drive signal (100 at ~ 20 kHz) was sufficient to keep the transmit side depolarized.

The aluminized mylar is very satisfactory until a slight temperature range is introduced. Above 50°K , in the absence of the dc bias, the mylar becomes fully depolarized in a matter of minutes. It is then not possible to obtain a stable signal.

Quartz and mica dielectric membranes are useful at high temperatures. The quartz has the advantage of very little polarization. Quartz films can easily be obtained by blowing bubbles in quartz tubing. However, it is difficult to obtain flat quartz films. In addition, the films fail by fracture to easily be practical. However, more recent work which we have not had time to complete indicates that much thicker films, ~ 0.002 , might be satisfactory from an acoustic point of view. Small diameter flat plates of such material are available from Corning Glass Works.

The mass of the movable films increases the amount of coupling of sound between the end plate and the transducer. An unbonded metal foil is equally effective for the flexible electrode as a bonded foil or coating. In addition, transducers constructed with metal foils do not fail by electrode wear as quickly as coated transducers. In addition, unbonded foils have obvious advantages from the point of view of thermal expansion on delicate dielectrics. Nevertheless, tests on the large diameter, high temperature cavity, showed a great deal of end plate excitation. For this reason the back electrode was made with a much thinner layer of vapor deposited nickel-chrome.

Mica is very useful for high temperature dielectric films. Commercial plates ~ 0.005 " thick can easily be split into ~ 5 parts under water.

Table 5. Dielectric and flexible electrode parameters.

Dielectric		Electrode		Percent Polarizability	Depolarization Temperature	Maximum Operation Temperature	Comments
Material	Thickness inch	Material	Thickness inch				
Teflon	0.001	Al foil	0.0005	3	-	250°C	Low activity, low spurious resonances
Mylar	0.0002-0.0005	Al coating Cu foil	10 ⁻⁵ .0003	100	<50	200°C	Depolarized by 100V AC on transmit side. Good activity. Low spurious resonances with Al coating.
Quartz	0.0001-0.001	Al foil Cu foil Re foil	0.0005 0.0003 0.0005	1	-	1300°C	Very difficult to handle. Low activity.
Mica	0.0005-0.001	Mo foil Re foil Chromel-B	0.0003 0.0005 10 ⁻⁵	100	280	1000°C	Not depolarized on transmit side. High activity low spurious resonances. Polarization greatly enhanced by H ₂ O, CO ₂ .

These films cut into ~ 1 cm circular samples and coated with nickel-chrome (over a ~ 0.8 cm diameter) are the best high temperature transducers found to date. The activity of the mica dielectric transducers is much ($\times 5$) greater than transducers with other dielectrics. This is possibly due to the stiffness of the mica dielectrics causing more gas motion around the coupling hole.

However, the mica coated with nickel-chrome transducer is not completely satisfactory. Even after careful surface preparation the nickel-chrome coating tends to flake off. Although the mica dielectric has never failed the transducers do not survive thermal cycling above 600°K . In addition, the transducer coating lasts only about 8 hours at 1000°K . The mica transducers show strong polarization effects. The polarization rate seems to vary somewhat from sample to sample and is greatly enhanced by H_2O and CO_2 . In dry N_2 , Ar and air the mica dielectric transducers work well except for a small temperature range between 200 and 280°K where polarization changes very quickly.

One of the difficult problems in realizing the electrostatic transducers is obtaining small coupling holes with diameters of $< 0.010''$. The hole has to be in a thick enough plate so that resonances in the plate vibrations are all well above the frequencies of interest. This means a $0.010''$ hole in a $0.100''$ plate. After trying several potential sources of such holes we found laser drilling and jewel bearing firms which could provide appropriate coupling holes. A company called Laser Nucleonics in Waltham has put a $0.004''$ hole in a $0.125''$ plate and can drill smaller holes if desired. A second approach has involved using orifice jewels (made by watch jewel manufacturers in Waltham). We have tried jewels with holes ranging from $0.008''$ to $0.002''$ in diameter. The geometry of these holes is extremely well known which makes orifice jewels particularly attractive for checking coupling hole corrections. However, most of the coupling holes used for data taking were smooth bore straight through holes drilled by conventional* means, with diameters between $0.008''$ and $0.013''$.

The laser drilled holes are conical, tapering about $0.002''$ per $0.020''$ of length. The walls of the hole are quite rough and the modes on the coupling hole cannot be calculated. However, the laser drilled holes give a large amplitude of cavity excitation with a small coupling correction. The laser drilled holes must be calibrated to obtain 1% corrections, which is equivalent to 0.01% in linewidth.

*Electric discharge and cut drill stocks.

The orifice jewel coupling holes are smooth bore cylindrical holes. The jewel is a piece of Al_2O_3 about 0.030" long and 0.060" wide with an ~ 0.005 " hole drilled in the center. The jewel is press fit into a 0.060" hole drilled in the end plate of the cavity. The jewel holes' geometry is well known because an optical comparator photograph is supplied with each jewel. A photograph of the jewel cross section is useful because the jewel is transparent. The hole and the taper in the back end are clearly visible in these pictures. Since the outside radius is accurately known, the hole length and radius can be determined from the photographs to better than 1%. Thus, the jewels are ideal for calibration purposes. It should be noted however that the output from jewel coupling holes is sharply reduced compared to drilled holes. This can be rectified by using a metallic backing on the jewel.

The coupling holes used for the bulk of the data were uniform radius (to $\sim 1\%$) through the entire plate thickness. The holes were cleaned with steel cleaning rods which can be obtained from watch supply outlets. Otherwise, the holes were used in the as drilled condition. Due to the length of the required coupling holes 0.008" was the lowest diameter drilled hole we could obtain. Much smaller holes can be obtained by slip fitting steel capillary tubes to larger holes in the end plate. However, several acoustic considerations put a lower limit on the permissible hole size. Considerable reduction of the hole correction can be effected once the operation of coupling holes smaller than 0.008" is studied experimentally.

Some of the factors limiting hole size variation can be seen from consideration of signal levels. The output voltages of the receive transducer is between 0.2-20 μV in all the measurements reported in the present work. Transducer sensitivity is about 1 $\mu\text{V}/\mu\text{bar}$. Therefore, the pressure wave in the receive coupling hole is 2×10^{-7} to 2×10^{-4} bars. The reflection of the pressure wave in the cavity approximately doubles the incident pressure amplitude in the coupling hole. This means that pressure levels in the cavity are 10^{-7} - 10^{-4} bars. Due to the Q of the cavity, the field in the cavity is Q times the exciting field from the transmitter coupling holes. However, the pressure incident on the cavity from the coupling hole is $\sim \left(\frac{a}{r_0}\right)^2$ times as large as the pressure transmitted into the cavity. Therefore, the pressure field in the coupling holes is approximately 10^{-4} - 10^{-1} bars! Thus, because of the large area ratio between the coupling holes and the cavity one can easily get nonlinear flow in the coupling holes. Nonlinearities in the coupling hole render the hole correction intractable and cause several interfering effects (such as odd harmonics).

The above discussion applies for 0.010" diameter coupling holes. The receive voltage level of 0.2 μ V is the minimum level that one can use without intolerable feedthrough and receiver noise.

Since the receive signal varies with $\left(\frac{r_o}{a}\right)^2$ the sound pressure amplitude in the transmitter coupling hole must be raised by $\left(\frac{r_o}{a}\right)^2$ when the coupling hole size is decreased. It appears that coupling holes ~ 0.001 " diameter should be possible with a drive level of 10^{-2} and a receive voltage level of 0.2 μ V from the above considerations. However, successful operation below ~ 0.005 " may not be possible due to inefficiency of the electrostatic transducer operating into small holes and viscous losses in the coupling holes. In addition, signal levels higher than 0.2 μ V are necessary for linewidth measurements better than $\sim 0.1\%$.

4.4 ELECTRONICS

Two electronic systems were used to drive cavity and process the output. The initial work in argon and nitrogen was completed using a PAR HR28 phase-lock amplifier. The PAR has an oscillator which provided the (1 V) drive amplifier signal. The drive amplifier in turn provided up to 270 volts rf to the transmit transducer. The signal from the output of the cavity was fed in turn into the signal end of the PAR instrument.

The signal end of the HR28 also incorporates an amplifier which is ganged tuned with the oscillator. The tuned amplifier has an adjustable Q which was set at 5. The amplifier feeds a phase detector. The phase of signal from the amplifier is compared to the phase of a reference signal from the HR-8 oscillator. A phase shifter in the reference channel allows the phase detector to be nulled. The phase reading on the phase shifter is then the 90° complement of the phase shift between the oscillator driving the cavity and the signal through the cavity.

The measured quantity is the phase shift between the reference voltage inside the phase-lock amplifier and the voltage at the input to the HR-8 phase detector. Examination of the overall experimental diagram in Fig. 11 indicates that there are several electrical elements between the pressure wave in the cavity and the electrical signals we measure. Therefore, tests were carried out to prove that these electrical elements do not introduce additional phase shifts which influence the linewidth measurement.

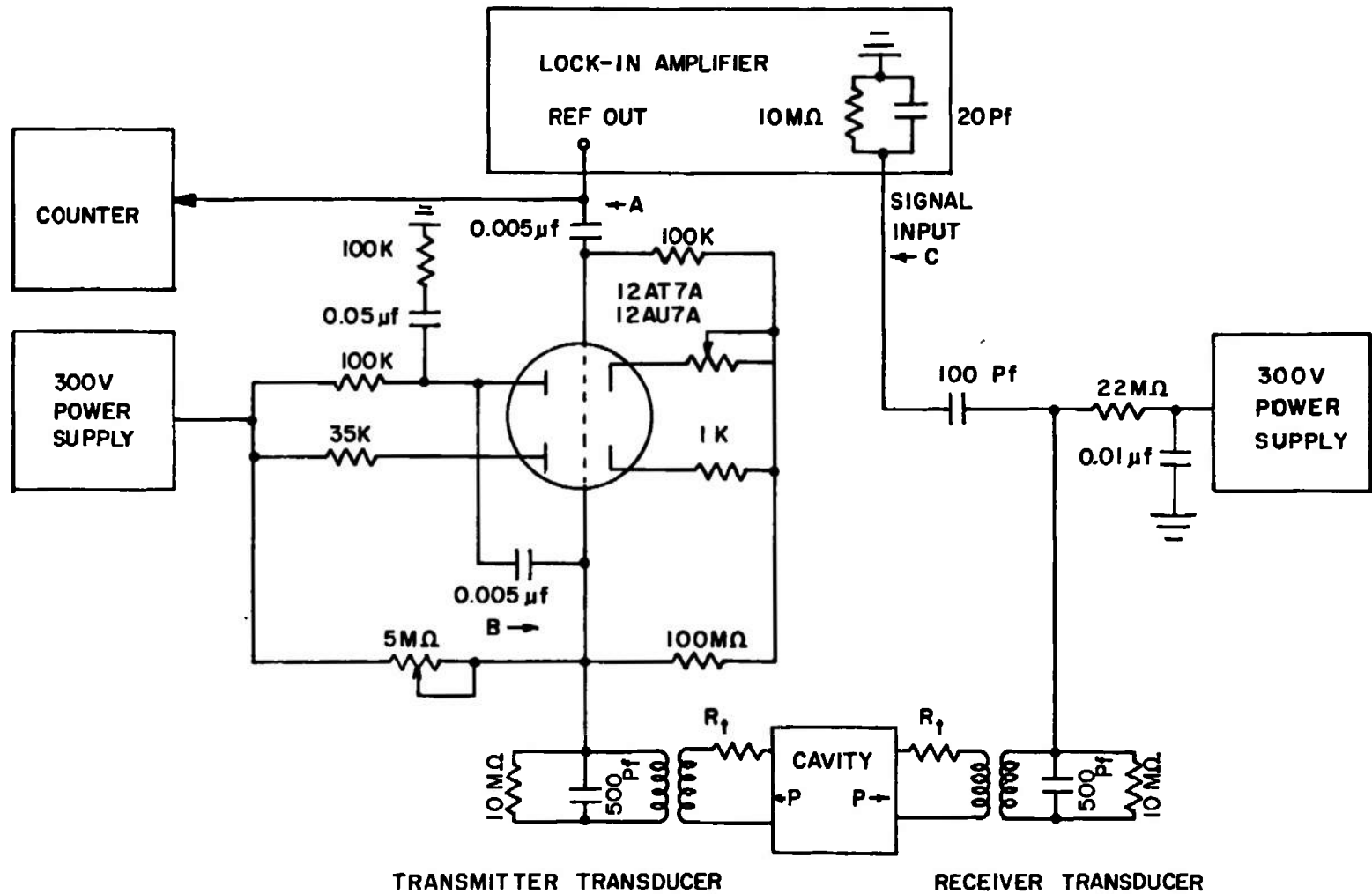


Fig. 11. Circuit details for cavity proof tests.

The electrostatic transducer requires a ~ 100 volt ac signal and a variable dc bias of up to 200 dc. Since the signal channel tuning must be exactly set on the reference frequency, we obtained the transducer driving signal by amplifying the reference signal from the phase-lock amplifier. It is relatively simple to build an amplifier which has a roughly linear frequency dependent phase shift. One such device built around a 12 AU7 is indicated in Fig. 11.

The output of the drive amplifier might seem a better choice for a reference than the HR28 internal reference. This would avoid any possible phase shifts in the amplifier. However, it is much easier to obtain a distortion free reference voltage at low voltages. The cavity and the tuned amplifier of the HR28 filter out distortion introduced by the drive amplifier in the signal channel.

Most of the data was taken with an improved electronic system. The block diagram for this system is shown in Fig. 12. The heart of this system is the Model 129 PAR tracking phase-lock amplifier. This amplifier puts out a dc voltage proportional to the in-phase and 90° out of phase components of the signal channel with respect to the reference channel. These two components of the signal are read out on a digital voltmeter.

The frequency is set to 0.001 Hz, using a Rockland digital frequency synthesizer. The synthesizer frequency must be checked on a counter to be sure it is working properly. The sine wave is fed into a drive amplifier which provides the large amplitude required to drive the cavity.

A cathode follower stage was added to the drive amplifier to improve the high frequency output. The harmonic distortion of the drive signal is also considerably reduced by the cathode follower stage. In addition, a variable transducer bias control was incorporated in the output of the drive amplifier. The variable bias supply is required because the high voltage rf is not sufficient to depolarize the mica dielectric. Thus, periodically the drive transducer bias must be adjusted between ~ 10 and 40 volts. The improved version of the driver amplifier is shown in Fig. 13.

The frequency synthesizer and tracking phase-lock amplifier reduce the time required to make a complete measurement from three hours to one-half hour over the system in Fig. 11. A three-hour measurement time means that two data points per day are an absolute maximum data rate. Any equipment failure or temperature instability means

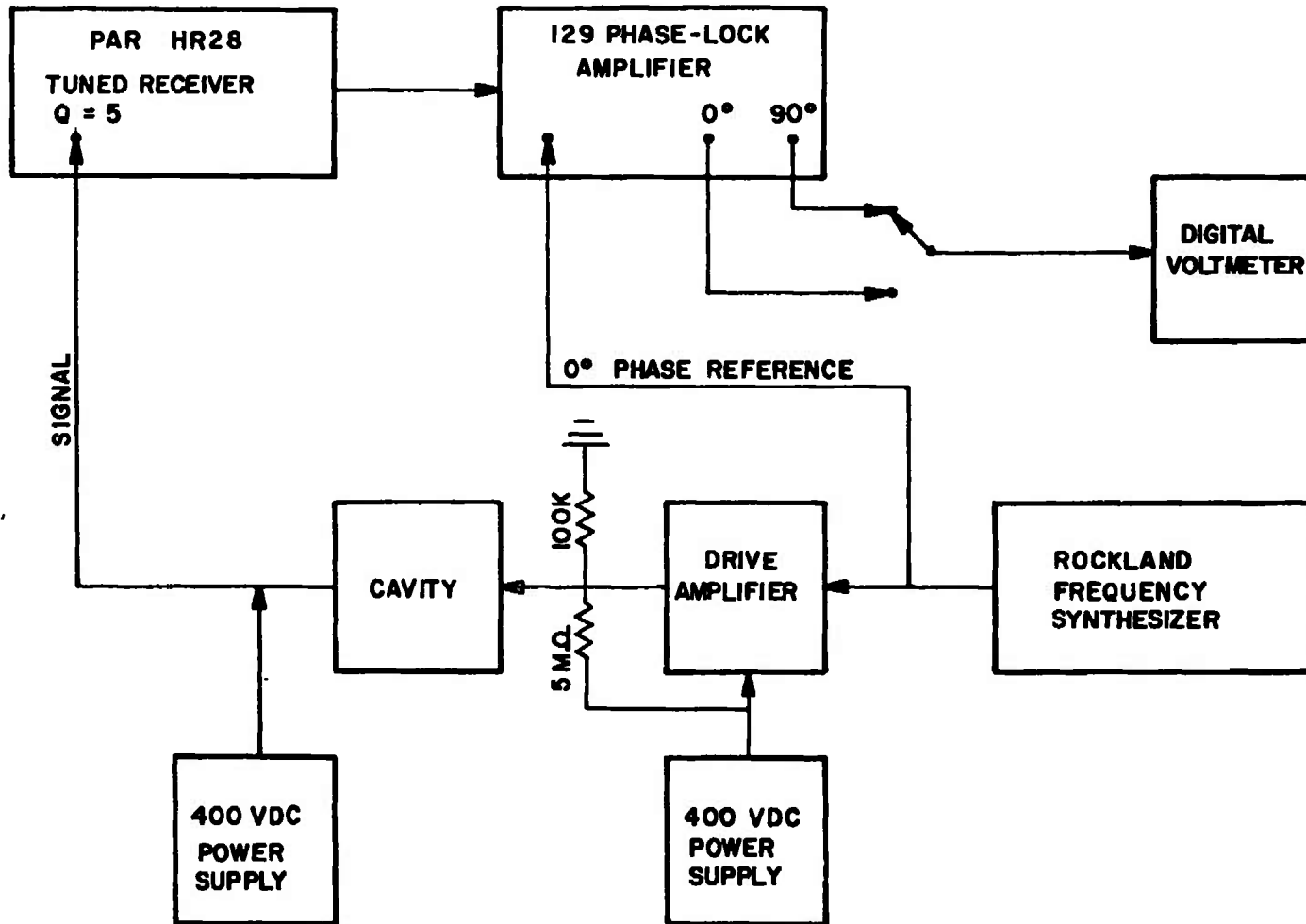


Fig. 12. Improved electronic system for cavity measurements.

70

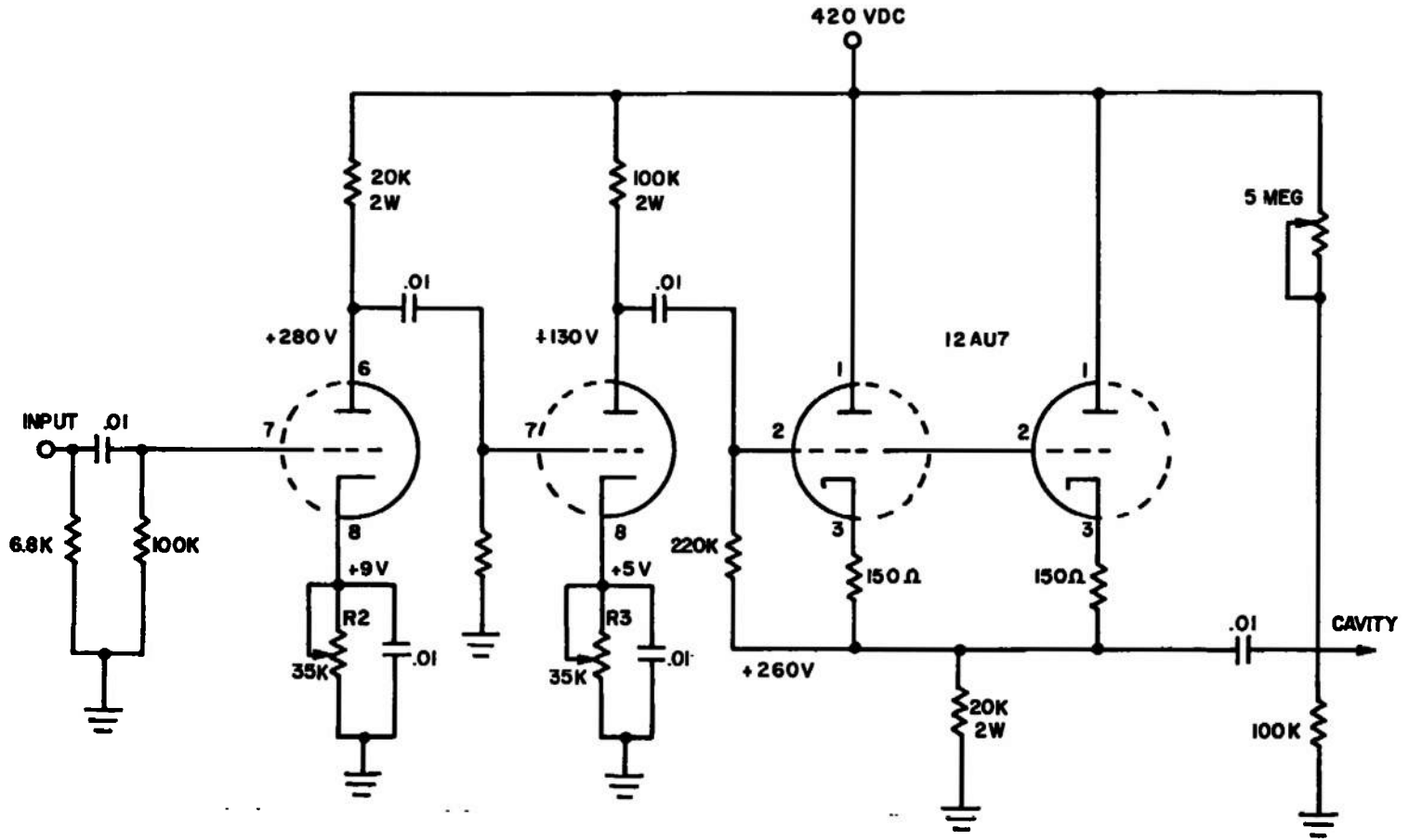


Fig. 13. Driver amplifier with cathode follower.

only one data point can be taken. The new equipment reduces the measurement time to a half hour so that any problems can be corrected, the system equilibrated, with enough time remaining in a half day's work to assure at least one measurement. Four data points a day can be taken at one temperature and different pressures with the Rockland frequency synthesizer and PAR 129 phase-lock amplifier.

The synthesizer and tracking phase meter also improve the immunity of the technique to line voltage, temperature, pressure and oscillator frequency drift. During a measurement of phase and amplitude versus frequency for a single mode the maximum drift consistent with 0.1% transport property measurement accuracy is 0.1 Hz, 6×10^{-3} °C, and 0.2 psi for frequency, temperature and pressure, respectively. Measurement of a single mode with the system in Fig. 11 requires these tolerances be held for an hour. The setup in Fig. 12 requires these tolerances be held for only ten minutes. Finally, the synthesizer allows the frequency to be changed by exact uniform steps (for instance, 10 Hz to ± 0.001 Hz). Thus, a counter is not necessary. In addition, the uniform spacing of frequency points decreases data reduction time by at least a factor of three.

The Model 129 phase-lock amplifier automatically tracks the synthesizer frequency, eliminating the time and error involved in tuning the receive amplifier to transmit signal frequency. However, the tuned amplifier of the HR28 is still used and is set to the line center before a line sweep is taken. In addition, both phase and amplitude measurements are done in the phase-lock mode. This means that the noise immunity is improved. Finally, phase and amplitude measurements are obtained simultaneously at one frequency which further reduces the data reduction time.

This is especially true of time-consuming feedthrough corrections. The 0° (in-phase) and 90° (out of phase) components of both the feedthrough and cavity signal had to be calculated from the phase and amplitude information with the system shown in Fig. 11. The appropriate feedthrough component could then be subtracted from the corresponding signal component. The PAR Model 129 directly measures the 0° and 90° components.

Although the line shape techniques described above provide a great deal of information, they have three major disadvantages. They are: (1) the measurement takes a long time, (2) the temperature must be held constant during this time, and (3) the frequency must be measured very accurately (typically 5 pt in 10^7 for 0.01% in linewidth). The

frequencies f_1 and f_2 corresponding to the $\pm 45^\circ$ phase measurements are subtracted to obtain the linewidth in the line shape technique. Since the linewidth is about 1% of f_1 and f_2 , accurate linewidths require much more accurate values of f_1 and f_2 . Also, the temperature must be held constant (to 0.01%) for roughly ten minutes while the line shape is being measured.

Transport property measurements can in principle be made much faster, and more accurately, using a double side-band technique which allows center frequency and linewidth to be set and measured separately. In the double side-band system illustrated in Fig. 14 the center frequency (ω_0) is sent into one leg of a balanced modulator and a frequency corresponding roughly to one-half of the half width into the second leg of the balanced modulator. The output of the modulator then consists of two equal amplitude sine waves, one at $\omega_0 + \omega_m$ and the other at $\omega_0 - \omega_m$. These two frequencies are sent simultaneously through the cavity.

The output of the cavity, shown also in Fig. 14, shows the usual beat pattern due to the interference of the ($\omega_0 \pm \omega_m$) signals. The center frequency is set holding ω_m constant and adjusting ω_0 until the envelope cross-overs as viewed on an oscilloscope are sharp. ω_0 can be set to 1% of the linewidth this way in a matter of seconds. More accurate line center frequency may be obtained by numerical processing of ω_0 versus ω_m which corrects for non-Lorentzian line shape, and/or electrical feedthrough, etc. The line center so defined is center of symmetry of amplitude and exact expressions for this quantity in terms of cavity geometry, sound speed and linewidth are available from the cavity theory. However, for 0.1% transport property determinations the 1% of linewidth ω_0 setting and the assumption of a Lorentzian line shape are adequate.

The setting ω_m to exactly one-half the linewidth requires the remaining electronic elements in Fig. 14. The output of the cavity is sent into a logarithmic detector which converts the envelope at ω_m into a cosine wave at $2\omega_m$. In addition, the phase of the detector output is twice the difference between the cavity phase shift ϕ_+ and ϕ_- at $\omega_0 + \omega_m$ and $\omega_0 - \omega_m$, respectively. When ω_m is one-half the linewidth $\omega_0 + \omega_m$ and $\omega_0 - \omega_m$ are brought 90° out of phase by their transit through the cavity. The output of the logarithmic detector is therefore 180° out of phase with the original ω_m .

The final step in the logic of setting ω_m equal to one-half the linewidth involves generating a cosine wave at $2\omega_m$ but 90° out of phase with the original ω_m driver. This is done to one part in 10^5 (in-phase) with a digital frequency and phase synthesizer described below. The reference

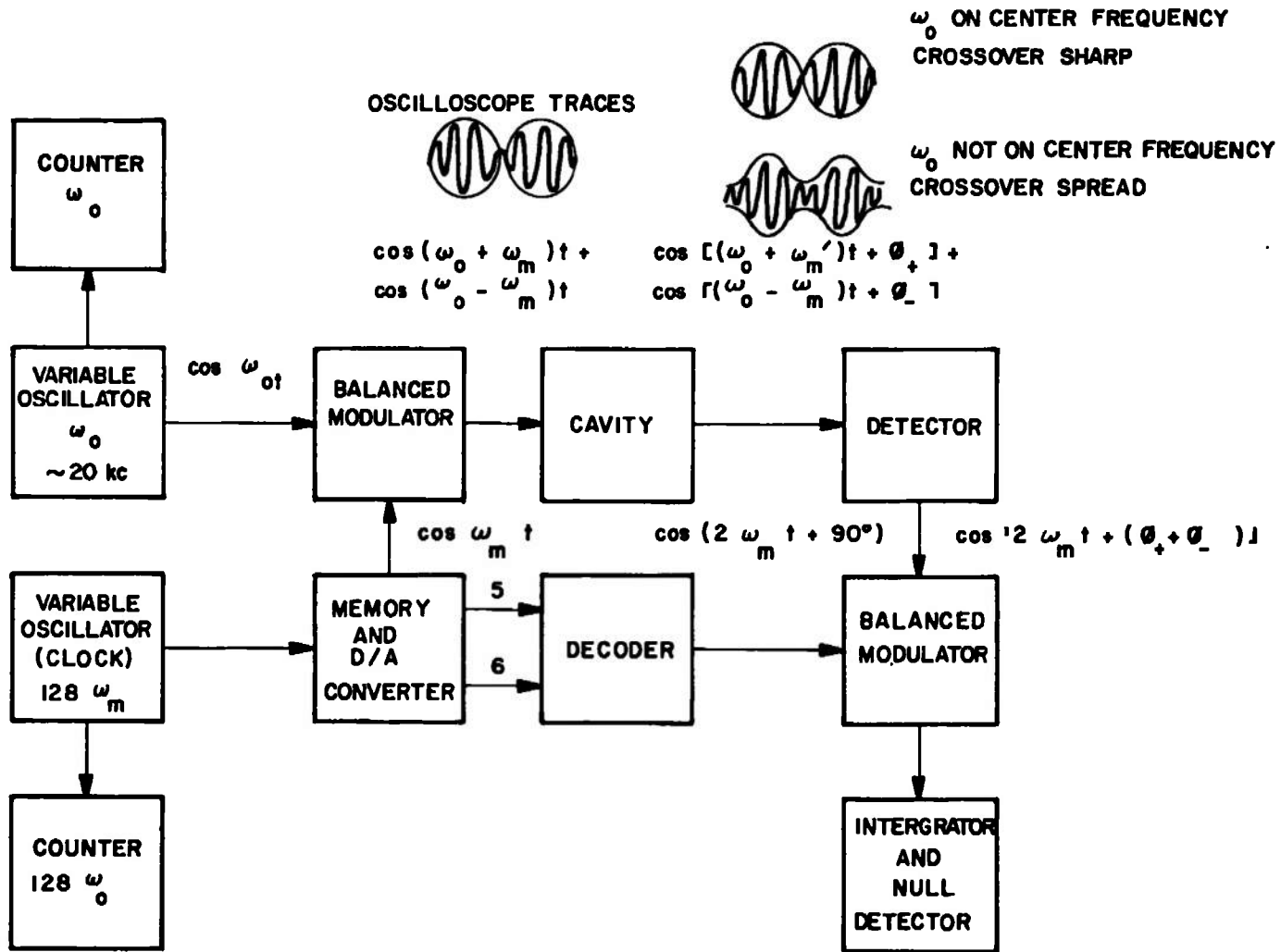


Fig. 14. Block diagram of automated linewidth measurement system using a double side band technique.

signal $\cos(2\omega_m + 90^\circ)$ is fed into the reference leg of a balanced modulator and the $\cos[2\omega_m + 2(\phi_+ - \phi_-)]$ from the logarithmic detector is fed into the other leg. ω_m is varied until a null in the balanced modulator output is obtained. This indicates that $2(\phi_+ - \phi_-)$ is 180° , or equivalently, ω_m is one-half the linewidth.

The above procedure requires some time to describe but the setting and measurement of ω_o and ω_m are accomplished in seconds. In addition, because the phase is generated digitally to one part in 10^5 the linewidth determinations to one part in 10^5 are possible! Thus, with a very simple electronic apparatus this technique holds promise for unheard of precision in thermodynamic and transport property measurements.

The key factor which allows such precise linewidth measurement to be performed is the development of a digital frequency synthesizer and digitally phase shifted output.

The problem was to obtain a signal source (ω_m) which would continuously tune the range from 0-10 kHz while providing an extremely precise signal at $2\omega_m + 90^\circ$ which would contain essentially no even harmonic distortion. These conditions are met by the use of a specially modified hybrid circuit manufactured for military use by Micro Networks Corporation of Worcester, Massachusetts (see Fig. 15). This hybrid circuit consists of a seven bit counter, a 1024 bit read-only memory (programmed with the sine table), a seven bit digital-to-analog voltage converter and the associated reference voltage supplies and amplifiers.

In operation the counter is driven by a clock signal at a frequency of $128\omega_m$. Each pulse of the clock selects in sequence one word (8 bits) of the memory. The word is a number corresponding to the amplitude of the sine wave at that time and is converted to a voltage by the D/A converter. The output of the unit is then a highly accurate sine wave whose frequency is derived from that of the clock

$$\omega_m = \frac{\text{clock frequency}}{128}.$$

The modifications which were made for us were to bring out the leads from the 5th and 6th bits of the counter. The voltage at the 5th bit changes its state every 45° (that is, every eighth clock pulse) while the voltage from the 6th bit changes state every 90° (every fourth clock pulse).

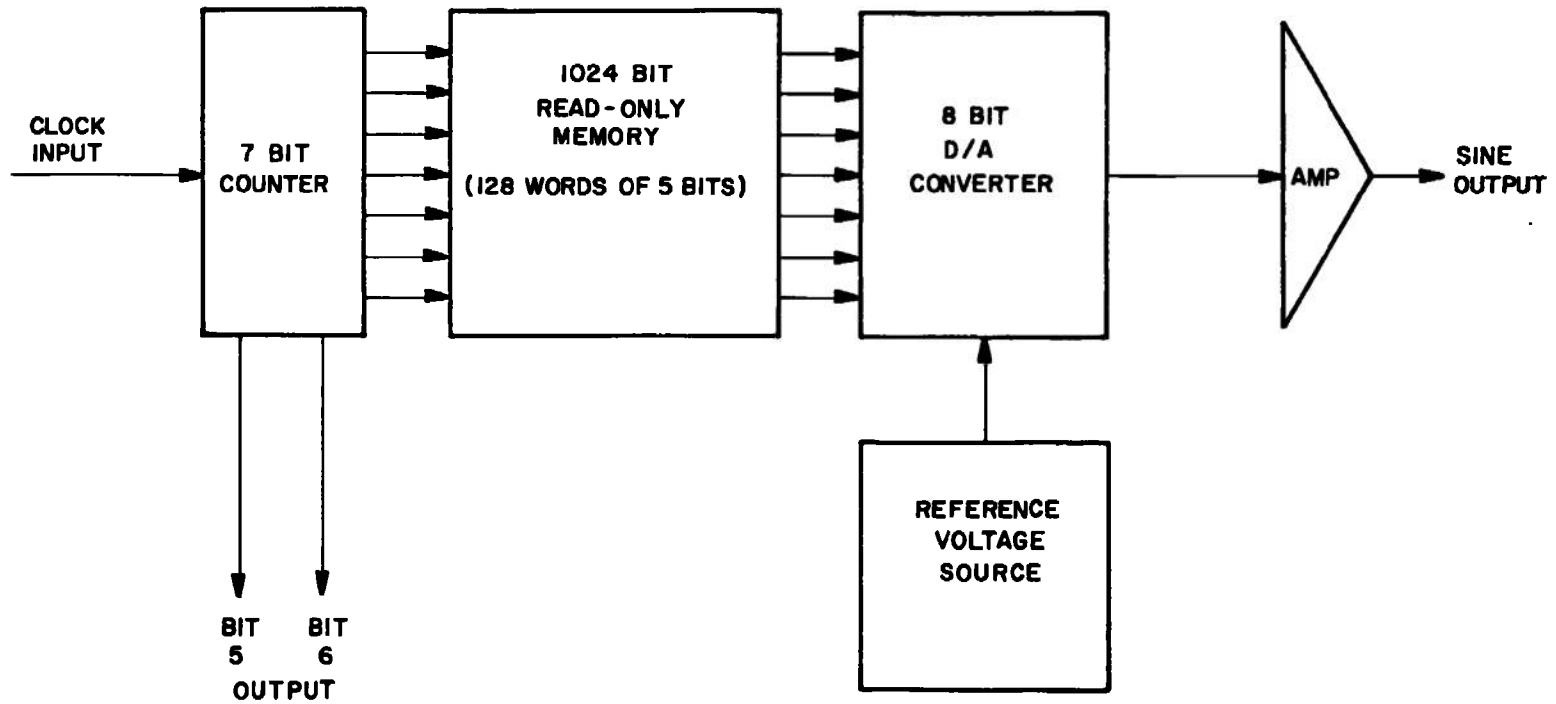


Fig. 15. Block diagram of hybrid circuit.

The sine wave output ω_m and the square waves* at $2\omega_m$ (bit 6), $4\omega_m$ (bit 5) and $2\omega_m + 90^\circ$ (exclusive OR), are shown in the timing diagram, Fig. 16. The $\omega_m + 90^\circ$ square wave is obtained, for instance, by decoding the $2\omega_m$ and $4\omega_m$ in an "exclusive" or logic gate. This device constitutes the blocks labeled "sine wave" and "decode" in Fig. 14.

The digital phase synthesizer proved valuable for calibrating the quadrature of the phase-lock amplifiers used in the line sweep measurements. The $2\omega_m$ outputs from bit 6 and the exclusive OR are 90° out of phase to a precision limited by the jitter of the digital logic. This jitter is some fraction of the switching time (~ 5 nsec) of the logic. Thus, at the maximum frequency ($2\omega_m = 20$ kHz) the device will put out the 90° phase angle as defined to better than 0.02° or 0.02%. Thus, the quadrature of the phase-lock amplifiers is checked by putting bits into the signal port and the exclusive OR into the reference channel. The 90° angles as read out from the phase-lock amplifiers were found to be good to 0.05° . The fractional quadrature error results in a fraction linewidth error of the same magnitude. Therefore, the systematic quadrature error tends to cancel in the subtractions and divisions used to obtain transport properties from linewidths.

4.5 DATA

Measurement of viscosity, Prandtl number and sound speed are presented in Tables 6-13. The gases covered are argon, nitrogen, hydrogen and air. The accuracy of the argon and nitrogen viscosity data below 100 atm. is 0.1% in viscosity and 0.5% in Prandtl number. The viscosity data in this range is within 0.2% of the oscillating disk results.⁴³ The remaining data have not been compared in detail with other work but spot checks indicate accuracies better than 1%.

The maximum temperature-pressure point measured was 405 atm at 600°K . The atmospheric data in nitrogen and air were extended to 1000°K . End plate resonances prevented data taking in hydrogen at elevated temperatures.

* ω_m refers to the frequency of the fundamental component of the square wave.

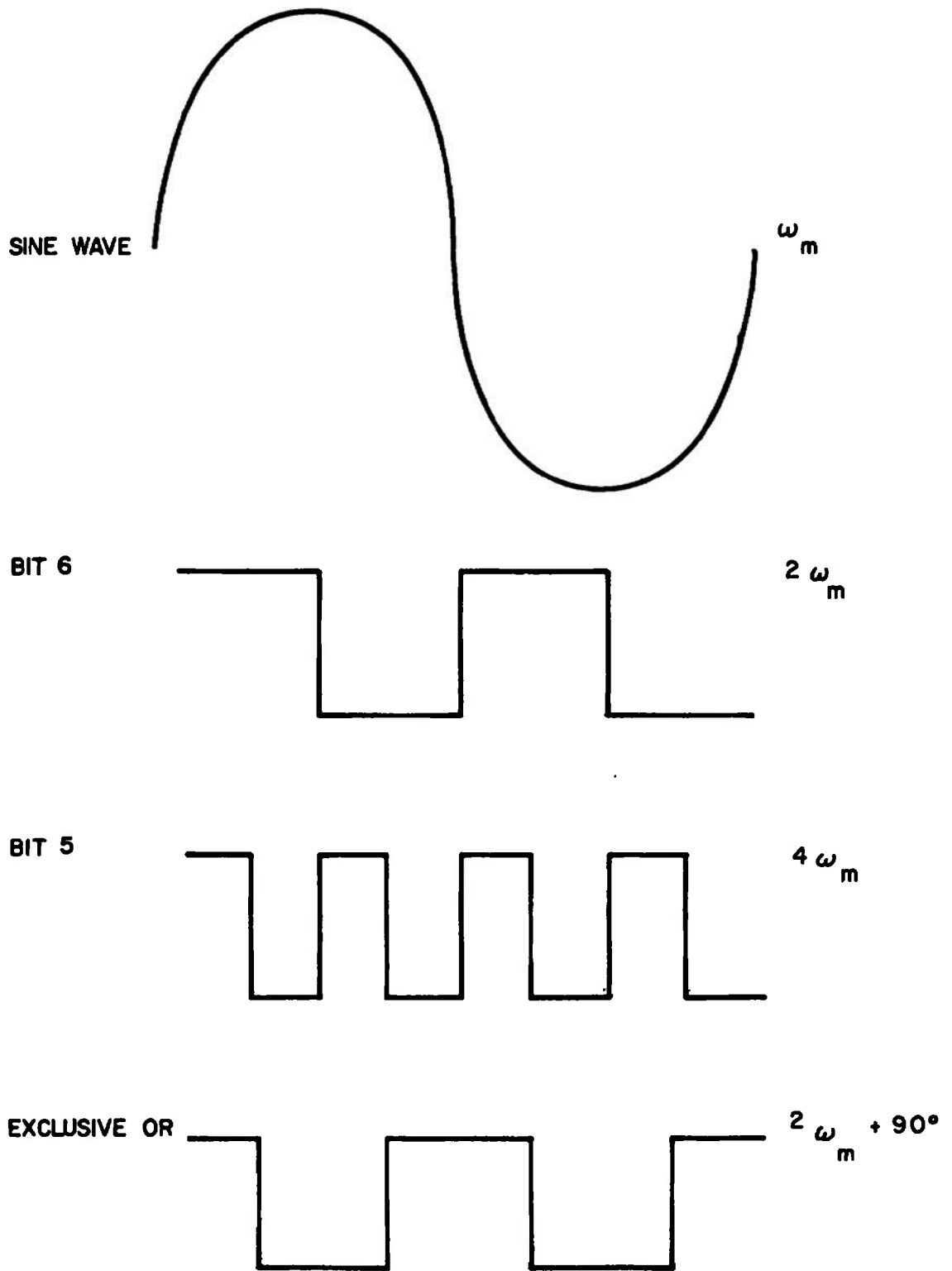


Fig. 16. Timing diagram for digital synthesizer decoder.

Table 6. High temperature measurements in nitrogen (1 atm).

Temperature $^{\circ}\text{K}$	Viscosity $\times 10^{-4}$ Poise $\text{g sec}^{-1} \text{cm}^{-1}$	Prandtl Number	Thermal Conductivity $\times 10^{-4}$ Watts $\text{cm}^{-1} \text{K}^{-1}$	Specific Heat Ergs $\text{g}^{-1} \text{K}^{-1}$ (Ref. 33)	Density g cm^{-3} (Ref. 26)
299.0	1.789	0.714	2.619	1.040	1.1414
382.5	2.159	0.705	3.192	1.043	0.8922
407.1	2.283	0.708	3.368	1.045	0.8383
420.3	2.306	0.700	3.445	1.046	0.8120
435.1	2.378	0.720	3.553	1.048	0.7843
437.2	2.374	0.697	3.568	1.048	0.7806
440.7	2.380	0.693	3.601	1.048	0.7744
608.9	2.984	0.695	4.615	1.076	0.5605
762.0	3.473	0.694	5.562	1.112	0.4479
856.6	3.751	0.699	6.096	1.136	0.3984
950.6	4.031	0.705	6.619	1.157	0.3590
992.3	4.119	0.697	6.893	1.166	0.3439

Table 7. High temperature measurements in air (1 atm).

Temperature °K	Viscosity $\times 10^{-4}$ Poise $\text{g sec}^{-1} \text{cm}^{-1}$	Prandtl Number	Thermal Conductivity $\times 10^{-4}$ Watts $\text{cm}^{-1} \text{°K}^{-1}$	Specific Heat Ergs $\text{g}^{-1} \text{°K}^{-1}$ (Ref. 33)	Density g cm^{-3} (Ref. 27)
350.6	2.109	0.713	2.98	1.009	1.006
398.1	2.315	0.710	3.30	1.014	0.886
404.4	2.342	0.701	3.34	1.014	0.873
425.1	2.429	0.709	3.47	1.017	0.830
591.8	3.064	0.709	4.53	1.049	0.596
599.2	3.104	0.709	4.50	1.051	0.589
716.4	3.486	0.711	5.29	1.079	0.493
750.3	3.593	0.711	5.49	1.087	0.470
799.4	3.758	0.707	5.75	1.097	0.441
805.5	3.777	0.703	5.90	1.100	0.438
895.2	4.051	0.710	6.38	1.120	0.394
954.9	4.224	0.715	6.59	1.132	0.370
380.2	2.241	0.711	3.19	1.012	0.928
401.6	2.330	0.711	3.33	1.014	0.879
448.3	2.526	0.709	3.63	1.021	0.787
519.2	2.804	0.708	4.09	1.033	0.680
609.1	3.137	0.705	4.69	1.054	0.579
650.7	3.260	0.710	4.87	1.063	0.542
699.0	3.446	0.710	5.20	1.074	0.505
711.6	3.467	0.710	5.25	1.077	0.496
790.1	3.726	0.703	5.69	1.097	0.447
850.6	3.909	0.703	6.07	1.110	0.415
880.2	3.987	0.697	6.39	1.117	0.401
956.4	4.241	0.703	6.70	1.133	0.369

Table 8. High pressure measurements in nitrogen.

Temperature °K	Pressure atm	Viscosity $\times 10^{-4}$ Poise $\text{g sec}^{-1} \text{cm}^{-1}$	Prandtl Number	Specific Heat C_p $\times 10^7$ Ergs $\text{g}^{-1} \text{°K}^{-1}$	Specific Heat Ratio	Sound Speed $\text{cm}(\mu\text{sec})^{-1}$	Thermal Conductivity $\times 10^{-4}$ Watts $\text{cm}^{-1} \text{°K}^{-1}$
294.2	1.000	176.4	0.713	1.040	1.400	0.03498	257.3
291.7	4.940	175.1	0.710	1.061	1.402	0.03491	261.7
289.2	5.300	174.7	0.712	1.062	1.401	0.03478	260.6
292.2	6.700	175.8	0.713	1.065	1.408	0.03497	250.1
295.4	57.82	187.4	0.724	1.128	1.499	0.03619	291.9
295.3	66.53	189.6	0.728	1.142	1.513	0.03640	297.4
294.8	72.86	191.0	0.732	1.152	1.523	0.03669	300.6
298.9	87.62	196.9	0.730	1.161	1.550	0.03723	313.2
298.8	101.2	200.4	0.728	1.177	1.571	0.03767	324.0
298.9	102.8	201.1	0.728	1.779	1.573	0.03768	325.7
298.8	108.5	202.1	0.733	1.190	1.582	0.03797	328.1
299.0	112.6	204.0	0.729	1.196	1.589	0.03815	334.7
298.9	115.4	204.2	0.732	1.197	1.593	0.03824	333.9
299.0	127.9	208.8	0.736	1.214	1.613	0.03874	344.4
298.6	137.7	209.9	0.739	1.227	1.624	0.03919	348.5
299.6	159.9	219.5	0.742	1.240	1.674	0.04701	366.8
297.6	240.3	244.0	0.747	1.309	1.831	0.04352	426.4

Table 9. High pressure measurements in air.

Temperature °K	Pressure atm	Viscosity $\times 10^{-4}$ Poise $\text{g sec}^{-1} \text{cm}^{-1}$	Prandtl Number	Specific Heat C_p $\times 10^7$ $\text{Ergs g}^{-1} \text{°K}^{-1}$	Specific Heat Ratio	Sound Speed $\text{cm}(\mu\text{sec})^{-1}$	Thermal Conductivity $\times 10^{-4}$ $\text{Watts cm}^{-1} \text{°K}^{-1}$
298.6	10.01	1.886	0.711	1.012	1.417	0.03529	2.686
299.7	21.42	1.916	0.710	1.020	1.465	0.03550	2.749
298.8	36.30	1.937	0.702	1.034	1.486	0.03568	2.855
298.1	52.7	1.968	0.722	1.087	1.498	0.03587	2.960
297.8	91.5	2.051	0.739	1.148	1.554	0.03669	3.186
298.0	101.2	2.104	0.747	1.161	1.572	0.03699	3.269
296.8	108.2	2.119	0.752	1.171	1.592	0.03713	3.295
297.1	116.4	2.149	0.762	1.185	1.598	0.03740	3.339
297.2	231.1	2.175	0.762	1.194	1.638	0.03763	3.410
297.4	130.5	2.198	0.768	1.202	1.609	0.03790	3.442
298.3	152.1	2.995	0.787	1.232	1.649	0.03881	3.592
298.4	211.8	2.603	0.840	1.302	1.704	0.04167	3.994
298.3	299.5	2.904	0.835	1.363	1.913	0.04665	4.743

Table 10. High pressure measurements in hydrogen.

Temperature °K	Pressure atm	Viscosity $\times 10^{-4}$ Poise $\text{g sec}^{-1} \text{cm}^{-1}$	Prandtl Number	Specific Heat C_p $\times 10^7$ Ergs $\text{g}^{-1} \text{°K}^{-1}$	Specific Heat Ratio	Sound Speed $\text{cm}(\mu \text{sec})^{-1}$	Thermal Conductivity $\text{Watts cm}^{-1} \text{°K}^{-1}$
295.15	1.441	0.884	0.703	14.311	1.405	1301.9	17.9
295.29	3.945	0.884	0.703	14.319	1.405	1302.8	18.0
295.26	5.556	0.884	0.704	14.328	1.403	1307.8	17.9
295.25	6.610	0.884	0.702	14.328	1.405	1307.9	18.0
297.16	9.120	0.883	0.702	14.336	1.406	1307.4	18.0
291.08	15.65	0.882	0.702	14.315	1.406	1314.6	17.9
291.79	22.31	0.883	0.703	14.369	1.406	1321.8	18.0
296.73	24.66	0.884	0.704	14.377	1.407	1331.6	18.0
297.78	33.23	0.883	0.697	14.398	1.407	1342.4	18.2
297.57	39.80	0.885	0.702	14.414	1.407	1326.3	18.2
297.47	42.17	0.884	0.702	14.418	1.408	1327.5	18.2
295.26	48.30	0.885	0.702	14.439	1.409	1350.3	18.2
297.56	56.90	0.888	0.701	14.460	1.409	1359.6	18.3
269.31	57.80	0.890	0.702	14.460	1.410	1366.6	18.3
296.63	63.30	0.891	0.702	14.472	1.410	1365.9	18.4
294.60	69.00	0.894	0.703	14.484	1.411	1368.7	18.4
299.19	88.80	0.908	0.702	14.526	1.414	1393.7	18.8
299.15	108.8	0.912	0.703	14.550	1.420	1411.4	18.9

Table 11. High pressure measurements in argon

Temperature °K	Pressure atm	Viscosity $\times 10^{-4}$ Poise $\text{g sec}^{-1} \text{cm}^{-1}$	Prandtl Number	Specific Heat C_p $\times 10^7$ $\text{Ergs g}^{-1} \text{°K}^{-1}$	Specific Heat Ratio	Sound Speed $\text{cm}(\mu \text{sec})^{-1}$	Thermal Conductivity $\text{Watts cm}^{-1} \text{°K}^{-1}$
297.2	0.500	2.256	0.689	0.5209	1.670	.003200	1.73
297.2	1.00	2.255	0.89	0.5216	1.670	0.03203	1.70
299.2	20.41	2.302	0.691	0.5459	1.728	0.03235	1.82
294.8	26.80	2.295	0.690	0.5543	1.749	0.03213	1.84
296.9	28.10	2.319	0.692	0.5668	1.746	0.03225	1.90
299.2	40.82	2.363	0.700	0.5703	1.791	0.03255	1.93
295.7	46.50	2.358	0.702	0.5734	1.811	0.03250	1.93
294.4	67.60	2.437	0.725	0.6119	1.873	0.03278	3.06
294.1	81.36	2.480	0.739	0.6408	1.947	0.03286	2.15
296.0	100.0	2.571	0.755	0.6589	1.971	0.03328	2.24
295.4	103.6	2.582	0.754	0.6621	1.986	0.03331	2.27
294.2	110.3	2.610	0.762	0.6712	2.024	0.03344	2.30
294.2	117.4	2.645	0.776	0.6785	2.048	0.03361	2.31
295.2	125.1	2.700	0.777	0.6859	2.063	0.03389	2.38
295.0	132.3	2.724	0.776	0.6938	2.094	0.03430	2.43

Table 12. High pressure-temperature measurements in argon.

Temperature °K	Pressure atm	Viscosity $\times 10^{-4}$ Poise $\text{g sec}^{-1} \text{cm}^{-1}$	Prandtl Number	Specific Heat C_p $\times 10^7$ Ergs $\text{g}^{-1} \text{°K}^{-1}$	Specific Heat Ratio	Sound Speed $\text{cm}(\mu\text{sec})^{-1}$	Thermal Conductivity $\text{Watts cm}^{-1} \text{°K}^{-1}$
425.7	20.42	3.075	0.732	0.5761	1.7061	0.03801	2.42
426.1	59.70	3.141	0.725	0.5865	1.721	0.03942	2.54
423.1	108.2	3.565	0.778	0.5824	1.787	0.03997	2.67
424.8	153.2	3.350	0.737	0.6033	1.803	0.04273	2.74
522.5	214.8	3.511	0.737	0.6033	1.956	0.04372	3.01
518.7	254.6	3.984	0.786	0.6316	1.899	0.04491	3.37
521.5	351.1	4.119	0.744	0.6656	1.982	0.04982	3.84
522.6	365.8	4.211	0.762	0.6891	2.014	0.04995	3.81
510.5	415.6	4.354	0.752	0.6895	2.263	0.04521	3.88
510.4	25.33	3.978	0.744	0.6702	1.685	0.04141	2.77
507.7	154.7	3.736	0.706	0.5182	1.829	0.04283	3.08
507.2	221.7	3.843	0.699	0.5823	1.932	0.04352	3.25
511.3	330.1	3.596	0.612	0.5914	2.019	0.04578	3.52
601.9	480.1	4.405	0.701	0.5998	2.196	0.04792	3.78
602.3	220.5	4.231	0.704	0.6021	1.834	0.05814	3.52
600.0	318.7	4.393	0.700	0.5863	1.895	0.06013	3.70

Table 13. High pressure-temperature measurements in nitrogen.

Temperature °K	Pressure atm	Viscosity $\times 10^{-4}$ Poise $\text{g sec}^{-1} \text{cm}^{-1}$	Prandtl Number	Specific Heat C_p $\times 10^7$ Ergs $\text{g}^{-1} \text{°K}^{-1}$	Specific Heat Ratio	Sound Speed $\text{cm}(\mu\text{sec})^{-1}$	Thermal Conductivity $\text{Watts cm}^{-1} \text{°K}^{-1}$
392.6	10.29	2.207	0.714	1.050	1.412	0.04063	3.25
421.9	51.24	2.373	0.720	1.093	1.432	0.04312	4.14
401.2	99.94	2.370	0.725	1.115	1.474	0.04355	3.64
422.6	152.3	2.563	0.718	1.071	1.548	0.04727	3.51
398.4	214.3	2.595	0.775	1.013	1.532	0.04763	3.39
391.2	238.2	2.641	0.772	1.197	1.552	0.04843	4.09
392.6	422.9	3.144	0.781	1.175	1.653	0.05856	4.73
501.2	11.13	2.620	0.712	1.056	1.398	0.04576	3.89
501.6	172.2	2.817	0.765	1.095	1.483	0.05104	4.02
519.4	219.7	3.057	0.790	1.167	1.896	0.06029	4.52
511.1	521.1	3.641	0.785	1.175	1.901	0.0658	5.45
620.5	174.9	3.177	0.725	1.061	1.462	0.05617	4.65
622.37	192.9	3.224	0.782	1.070	1.797	0.06269	4.41
624.0	413.5	3.498	0.775	1.162	1.671	0.06802	5.24
624.1	502.3	3.139	0.773	1.165	1.696	0.07181	4.73

SECTION V

SUMMARY

Acoustic resonators in gases provides a means for extremely precise (1-0.01%) thermal conductivity and viscosity determinations. In addition, sound speed is obtained at each pressure, volume, temperature point so that specific heat (sound speed) and relaxation time data are also obtained. Therefore a measurement with the acoustic resonator technique provides more information than separate measurements on a conventional thermal conductivity, viscosity plus a Joule-Thompson apparatus. Thus, one measurement on an acoustic resonator provides as much data as three conventional measurements. In addition, the data is self-consistent and potentially one to two orders of magnitude more accurate than existing techniques.

Theoretical expression for the linewidth and center frequency of the resonator is worked out for a nonideal gas with relaxation effects. Slip, accommodation and acoustic propagation into the walls are included. Slip corrections to viscosity and accommodation corrections for thermal conductivity are $\sim 0.5\%$ at 300°K (1 atm) and increase to $\sim 0.8\%$ at 1000°K (1 atm) for a 1 cm^3 volume cavity. However, these corrections become smaller directly with the square root of density and inversely with the square root of a typical cavity length. The losses due to propagation into the cavity walls increase from 0.1% in linewidth at ~ 1 amagat to $\sim 20\%$ in linewidth at ~ 400 amagats. Methods for calculating these quantities from measured quantities are detailed in the text.

Transducers for introducing sound into a resonator and sensing the resulting fields also contribute to the linewidth and center frequency. Methods for calculating the contribution of the transducers to the linewidth are given. The data reduction techniques for obtaining the linewidth from measurements with superimposed electrical feedthrough and mode coupling signals are discussed. These transducer associated effects amounted to as much as 50% of the measured linewidths at high pressures. However, with a combination of calculation and self-consistent iteration the transducer effects can be handled to a precision consistent with $\sim 0.1\%$ in viscosity.

Mechanical details of the transducers and cavities used in the present work are given. Mica dielectric electrostatic transducers coupled to the cavity with coupling holes ($\sim 0.2\text{ cm}$ long, 0.005 cm radius) were developed for use up to 1000°K . The tradeoffs between coupling corrections and allowable signal levels as a function of coupling hole

size are elaborated. It is concluded that an order of magnitude reduction of coupling hole correction beyond that obtained in the present work is feasible by specializing the hole size for narrow pvt ranges. Difficulties were encountered in running the mica dielectric transducers at temperatures above 600°K for times greater than ~ 8 hr. Therefore, electrostatic transducers with thick (0.002") quartz dielectric plates or conduction of the sound from regions below 600°K with acoustic wave guides are suggested for future high temperature work. It should be noted that the acoustic wave guide option could extend cavity measurements to about 2000°K .

Steel and invar cavities with volumes ranging between 1 and 4 cm^3 used in the present work are described in the text. The design tradeoff of oxidation resistance and acoustic impedance versus ease of fabrication and procurement is discussed. The greatest problem with the cavity design is flexural vibrations in the end plate. Thus, high modulus materials are optimum for end plate designs. It is also pointed out that cavities with volumes of up to 10 cm^3 are optimum for work at high temperatures or in hydrogen and helium.

Electronic systems for the accurate measurement of phase and amplitude versus frequency are described. A frequency synthesizer and a quadrature phase-lock amplifier are described which allow 0.01% linewidth determinations to be made. A digital phase shift synthesizer is described along with a modulation system capable of 0.001% linewidth determinations. However, the modulation system still requires a line sweep determination to eliminate feedthrough and correct for ω_0 Lorentzian line shapes. The electronics to drive and bias the transducers is also described.

Finally, data taken with the systems described above are presented. Accuracies of 0.1% in viscosity and 0.5% in Prandtl number are given for hydrogen, nitrogen, air and argon at 300°K at pressures up to about 150 atm. Data in argon and nitrogen are presented at pressures up to 460 atm and temperatures up to 600°K . In addition, measurements in nitrogen and air at temperatures up to 1000°K and at atmospheric pressure are given. These last two sets of data have accuracies approaching 0.5% in viscosity and 1% in thermal conductivity on the high temperature and high pressure ends.

REFERENCES

1. Goring, G. E., J. N. Holyoak, "Some Heat Capacities of Argon in Ranges 5 - 1000 Atm and 180 - 450°K", J. Chem. and Eng. Data 16, 173-177 (1971).
2. Carey, C., Carnevale, E. H., Uva, S., Marshall, T., "Experimental Determination of Gas Properties at High Temperatures and/or Pressures", AEDC-TR-68-105 (1968).
3. Carey, C., Carnevale, E. H., Uva, S., Marshall, T., "Experimental Determination of Gas Properties at High Temperatures and/or Pressures", AEDC-TR-69-78 (1969). Also, AEDC-TR-71-191 (1971), Carey, C., Bradshaw, J. H. and Carnevale, E. H.
4. Carey, C., "Boundary Layer Studies for Thermal Conductivity Determination", 9th Conf. on Thermal Conductivity, (H. Shanks Ed.) AEC Physics (TID-4500) pp. 572-586 (1970).
5. Smeets, G., "Bestimmung der Wärmeleitfähigkeit, Heisser Gas aus der Temperaturgrenzschicht in Strosser", Z. Naturforschg, 20A, 683 (1965).
6. Carey, C., Carnevale, E. H., "Measurements of Thermodynamic and Transport Properties with an Ultrasonic Technique," Thermal Conductivity, (C. Y. Ho and R. E. Taylor Ed.) Plenum Press, New York, 47-73 (1969).
7. Kohler, M., "Schallabsorption in binären Gasmischungen", Zeit. Für Physik 127, 41 (1949).
8. Apfel, J. H., "Acoustic Thermometry, Rev. Sci. Instr. 33, 428, (1962).
9. Bradshaw, J. H., "A Method for the Experimental Determination of the Coefficients of Viscosity and Thermal Conductivity of Gases by Means of an Acoustic Cavity Resonator", Ph.D. Thesis, Boston College (1972).
10. Thiesen, M., "Zur Theorie des geschlossenen Resonators, Ann. der Physik 24, 421-438 (1907).
11. Fritsche, L., "Theorie des Acustischen Zylinderresonators Unter Berücksichtigung der Schallanregung (II) Acoustica 16, 199-207 (1960).
12. Fritsche, L., "Präzision Messung der Klassischen Schallabsorption", Mit Hilfe des Zylinder Resonators (I) Acoustica 10, 189-198 (1960).

REFERENCES (cont'd)

13. Boa-Teh Chu, Kovaszny, L. S. G., "Non-linear Interaction in a Viscous Heat Conducting Compressible Gas", *J. Fluid Mech.* 3, 494-514 (1958).
14. Monin, A. S., Yaglon, A. M., Statistical Fluid Mechanics, MIT Press, Cambridge, Mass., 64-71 (1971).
15. Weston, D. E., "The Theory of the Propagation of Plane Sound Waves in Tubes", *Proc. Phys. Soc.* 66B, 695-709 (1953).
16. Henry, P. S., "The Tube Effect in Sound Velocity Measurements", *Proc. Phys. Soc.* 43, 340-361 (1931).
17. Huang, K., Statistical Mechanics, John Wiley, New York 109-110 (1963).
18. Loeb, L. B., The Kinetic Theory of Gases, Dover, New York (1961).
19. Present, R. D., Kinetic Theory of Gases, McGraw Hill, New York, 188-193 (1958).
20. Jody, B., Saxena, S. C., "Thermal Accomodation Coefficient Measurement in the Temperature Range 300° - 3600° K Neon-Tungsten", Univ. of Illinois, Dept. Energy Eng., TR-E-56 (1973).
21. Hutchinson, J. R., "Axisymmetric Vibrations of a Free Finite Length Rod", *JASA* 51, 222-240 (1972).
22. Zermanek, J., "An Experimental and Theoretical Investigation of Elastic Wave Propagation in a Cylinder, *JASA* 51, 265-283 (1972).
23. Rschevkin, S. N., The Theory of Sound, Pergamon Press, New York, Chapter V through VII (1963).
24. Mason, W. P., Electromechanical Transducers and Wave Filters, D. Van Nostrand, New York (1958).
25. Skvor, Z., "On the Acoustical Resistance Due to Viscous Losses in the Air Gap of Electrostatic Transducers", *Acustica* 19, 295-299, (1967/1968).

REFERENCES (cont'd)

26. Bender, E., "Equations of State Exactly Representing the Phase Behavior of Pure Substances", Proc. 5th Symp. on Thermophysical Properties, (C. F. Bonilla Ed.) ASME, New York, p. 227 (1970).
27. Zubarev, W. W., Kozlov, A. D., "Determination of Model Inter-molecular Potentials from Experimental Data", Translated from Tep 10 fiz. ka Vysokiky Temperature 9, 859-862 (1971).
28. Michaels, A., DeGraaff, W., Wassenaar, T., Levelt, J. M., Louwerse, P., "Compressibility Isotherms of Hydrogen and Deutrium at Temperatures Between - 1750°C and 150°C, Physica, 25, 25-42 (1959).
29. Presnall, D. C., "Pressure-Volume-Temperature Measurements on Hydrogen from 200°C to 600°C and up to 1800 Atmospheres", J. Geophysical Reas. 74, 6026-6033 (1969).
30. Sengers, J. V., "Thermal Conductivity Measurements of Elevated Densities Including the Critical Region", Thesis Univ. Amsterdam (1962).
31. Newall, G. F., "Theory of Oscillation Type Viscometer V: Disk Oscillating Between Fixed Plates", ZAMP 10, 160-174 (1959).
32. Kestin, J., Leidenfrost, W., "The Effect of Moderate Pressures on the Viscosity of Five Gases", Thermodynamic and Transport Properties of Gases, Liquids and Solids, (Y. S. Touloukian, Ed.) McGraw Hill, New York (1959).
33. Touloukian, Y. S., Makita, T, "Thermophysical Properties of Matter", Volume 6, Plenum Press, New York, 16a and 13b.
34. Bauer, H. J., Schotter, R., "Collision Transfer of Vibrational Energy from Nitrogen and Methane to the Carbon Dioxide Molecule", J. Chem. Phys. 51, 3261-3270 (1969). (See also H. Roesler, Acoustica 17, 73-78, and H. J. Bauer, H. Roesler, Z. Naturforsch 19, 656, 1964).
35. Parker, J. G., Ritke, D. N., "Vibrational Relaxation Times of Methane and Oxygen at Increased Pressure", JASA 51, 169-181 (1972).

REFERENCES (cont'd)

36. Clark, A. L., Katz, L., "Resonance Method for Measuring the Ratio of the Specific Heat of a Gas C_p/C_r ", Pt. 1, Canadian Journal of Research 18A, 23-38 (1940).
37. Henderson, M. C., Donnelly, G. J., "Acoustic Resonance Tube for High Pressures and Low f/p ", JASA, 34, 719-734 (1962).
38. Eggers, F., Funck, Th., "Ultrasonic Measurements with Millimeter Liquid Samples in the 0.5-100 MHz Range", Rev. Sci. Inst. 44, 969-977 (1973).
39. Kuhl, W., Schodder, G. R., Schröder, F. K., "Condenser Transmitters and Microphones with Solid Dielectrics for Airborne Ultrasonics", Acustica, 4, 519-532 (1954).
40. Morse, P. M., Ingard, K. V., Theoretical Acoustics, McGraw Hill (1968).
41. Papadakis, E. P., "Tabulation of Coefficients of a Quadratic Function for the Thermal Expansion of Various Alloys and Other Engineering Materials", Materials Science and Engineering, 10, -95-203 (1972).
42. Sessler, G. M., West, J. E., "Electret Transducers: A Review", JASA, 52, 1589-1600 (1973).
43. Kestin, J., Payroç, E., Sengers, J. V., "On the Density Expansion for Viscosity in Gases," Physica 54, 1-19 (1971).

APPENDIX A

TRAVELING WAVES IN A CYLINDRICAL WAVE GUIDE

PHYSICAL VARIABLES

The cavity is a cylindrical wave guide with end wall mounted perpendicular to its axis. The linewidth and center frequency expressions can be obtained by first making wave functions which satisfy the wave equations and the boundary equations on the side walls. These waves are then allowed to reflect back and forth between the end walls of the cavity. The sum of all these reflections is the desired field in the cavity.

The wave equations are expressed in terms of the potentials H_1 , H_2 and H_3 (see Table A. 1). However, the boundary conditions apply to the pressure, temperature and flow velocity. The flow velocity is related to the potentials in the usual way^{1, 2}

$$\mathbf{v} = \nabla (H_1 + H_2) + \nabla \times \bar{H}_3. \quad (\text{A. 1})$$

The second term in (A. 1) can be simplified if only axisymmetric modes are considered. The contribution to the particle velocity due to the viscous wave is

$$\nabla \times H_3 = \frac{1}{r} \begin{vmatrix} \hat{r} & \hat{r}_\theta & \hat{z} \\ \frac{\partial}{\partial r} & \frac{\partial}{\partial \theta} & \frac{\partial}{\partial z} \\ H_r & H_\theta & H_z \end{vmatrix}. \quad (\text{A. 2})$$

The caret indicates unit vectors in the radial (r), azimuthal \hat{r}_θ , and axial (\hat{z}) direction. The axisymmetric condition means that the azimuthal component of the particle velocity must vanish. Thus, $H_r = H_z \equiv 0$. In addition, for simplicity we modify the nomenclature so that H_3 is a scalar satisfying

$$H_\theta = \frac{\partial^2 H_3}{\partial r \partial z}. \quad (\text{A. 3})$$

Notice that this new potential (H_3) satisfies the viscous wave equation. In addition, no spurious solutions are generated by the transformation in

Table A.1. Summary of wave equations for acoustic, thermal and viscosity potentials (see Ref. 3).

Mode			
	Acoustic	Thermal	Viscous (3 Equations)
Wave equations	$\nabla^2 H_1 + k_1^2 H_1 = 0$	$\nabla^2 H_2 + k_2^2 H_2 = 0$	$\nabla^2 \bar{H}_3 + k_3^2 \bar{H}_3 = 0$
Wave Constants	$k_1^2 = \left(\frac{\omega}{c}\right)^2 \frac{\gamma}{\gamma} [1 - i2\pi f \bar{\delta}_v]$	$k_2^2 = i\omega \bar{\gamma} \frac{\rho C_v}{\lambda} [1 - i\epsilon]$	$k_3^2 = i \frac{\rho \omega}{2\eta}$
Mode constants	$a_1 = -\frac{C_v}{C_v} \frac{k_1^2}{i\omega - \frac{\lambda}{\rho C_v} k_1^2}$	$a_2 = -\frac{C_v}{C_v} \frac{k_2^2}{i\omega - \frac{\lambda}{\rho C_v} k_2^2}$	-
Second order terms	$\bar{\delta}_v = \frac{\gamma}{\gamma} \frac{\omega}{\rho c^2} \left[\eta + \eta' + (\bar{\gamma} - 1) \frac{\lambda}{C_p} \right]$	$\bar{\epsilon} = \frac{\gamma}{\gamma} \frac{\omega}{\rho c^2} (\bar{\gamma} - 1) \left(\eta + \eta' - \frac{\lambda}{C_p} \right)$	

Eq. (A. 3) since only the differentiated form appears in the particle velocity. The particle velocity in the radial (\dot{r}) and axial (\dot{z}) directions are from (A. 1) and A. 3)

$$\dot{r} = \frac{\partial}{\partial r} \left[H_1 + H_2 + \frac{\partial^2 H_3}{\partial z^2} \right] \quad (\text{A. 4})$$

and

$$\dot{z} = \frac{\partial}{\partial z} \left[H_1 + H_2 - \left(\frac{1}{r} \frac{\partial H_3}{\partial r} + \frac{\partial^2 H_3}{\partial r^2} \right) \right]. \quad (\text{A. 5})$$

The acoustic temperature amplitude T is given in terms of the quantity

$$\theta = \frac{\beta}{\gamma - 1} T = a_1 H_1 + a_2 H_2 \quad (\text{A. 6})$$

where β is the thermal expansion coefficient, and γ the equilibrium specific heat ratio. a_1 and a_2 are given in Table A. 1. Equation (A. 6) is identical to (A. 23) of Ref. 3. However, a_1 and a_2 can be simplified to

$$a_1 = i \frac{C_v}{C_p} \frac{k_1^2}{\omega} \quad \text{and} \quad a_2 = -i \frac{C_v}{C_p} \frac{k_2^2}{(\gamma - 1) i \omega} \quad (\text{A. 7})$$

to better than 1 pt in 10^4 for the conditions of the present work. Terms of the order $\bar{\epsilon}$ have been neglected compared to 1 in a_2 and terms of the order of $\left(\frac{k_1}{k_2} \right)^2$ have been neglected compared to 1 in a_1 . The approximation $\left(\frac{k_1}{k_2} \right)^2 \ll 1$ is employed many times below. Therefore, values of $\left(\frac{k_2}{k_1} \right)^2$ are given in Table A. 2 for several pressures and temperatures in nitrogen. $\left(\frac{k_1}{k_2} \right)^2$ gets smaller directly as density over thermal conductivity are increased and as frequency is decreased. Experimentally,

Table A. 2. (Ratio thermal to acoustic wavelength)² for nitrogen
at several pressures and temperatures.*

Temperature °K			
PRESSURE ATM		300	1000
	1	1.01×10^{-3}	3.01×10^{-3}
	100	1.18×10^{-4}	4.07×10^{-4}
	500	0.71×10^{-4}	2.1×10^{-4}

* $\epsilon = 20$ kHz.

this fact makes high pressures and low frequencies favorable.*

Finally, an expression for acoustic pressure amplitude (p) in terms of potentials is obtained from the equations of state and conservation of energy. The conservation of energy is (a corrected version of) Eq. (A.16) of Ref. 1

$$\nabla^2 \phi = \left[\frac{\lambda}{\rho \bar{C}_v} \nabla^2 \theta + i\omega\theta \right] \frac{\bar{C}_v}{C_v} . \quad (\text{A. 8})$$

Differentiating the equation of state with respect to time as using (A. 8) to eliminate $\frac{\partial}{\partial t} \left(\frac{1}{\rho_o} \right)$ the equation of state becomes

$$\frac{\partial}{\partial t} \left(\frac{p}{\rho_o} \right) = - \frac{c^2}{\gamma} \nabla^2 \phi + \beta \frac{c^2}{\gamma} \frac{\partial T}{\partial t} . \quad (\text{A. 9})$$

Here c is the equilibrium sound speed and ρ_o the ambient density. The energy equation, together with the simple harmonic dependence of the pressure amplitude ($e^{-i\omega t}$), allow (A. 9) to be transformed into

$$\frac{p}{\rho_o} = \rho_o c^2 \frac{1}{\gamma k_w^2} \frac{\bar{C}_v}{C_v} \left[\nabla^2 \theta + \bar{\gamma} k_w^2 \theta \right] . \quad (\text{A. 10})$$

This can be further simplified using (A. 6) to eliminate θ . The final** expression for pressure becomes

$$p = \rho c^2 a_1 \frac{\bar{C}_v}{C_v} \bar{\gamma} H_1 \quad 0 \left(\frac{k_1}{k_2} \right)^2 . \quad (\text{A. 11})$$

*More mundane considerations of spurious resonances in the cavity walls favor small cavities. Also, at very high densities acoustic propagation into the walls becomes important.

**Note we have used $C_p - C_v = \bar{C}_p - \bar{C}_v$ since the contribution of internal modes (vibration, etc.) is the same for C_p and C_v and is independent of pressure for gases.

APPLICATION OF BOUNDARY CONDITIONS

The wave equations in Table A. 1 may be separated in cylindrical coordinates. In fact, for the cylindrical wave guide a complete set of orthogonal solutions can be found exactly. This set of wave functions are then used to obtain an extremely precise solution to the cavity problem. In addition, this complete orthogonal set of cylindrical wave guide solutions serves as the basis of transducer coupling corrections. Therefore, we have gone into the cylindrical wave guide problem in great detail.

The wave equations in Table A. 1 can be separated in the usual way into the solutions of the type

$$\begin{bmatrix} H_1 \\ H_2 \\ H_3 \end{bmatrix} = \sum_{p=0}^{\infty} \begin{bmatrix} A_p^{(1)} J_0(\gamma_p^{(1)} r) e^{ik_p^{(1)} z} \\ A_p^{(2)} J_0(\gamma_p^{(2)} r) e^{ik_p^{(1)} z} + B_p^{(2)} J_0(\gamma_p^{(1)} r) e^{ik_p^{(2)} z} \\ A_p^{(3)} J_0(\gamma_p^{(3)} r) e^{ik_p^{(1)} z} + B_p^{(3)} J_0(\gamma_p^{(1)} r) e^{ik_p^{(3)} z} \end{bmatrix} \quad (\text{A. 12})$$

The z dependent terms in the viscous and thermal waves can be suppressed for the cylindrical wave guide problem since the wave numbers involved have large imaginary parts. Thus, they are rapidly damped any distance greater than ~ 0.1 mm from the wall. The conditions of separation require that

$$\begin{bmatrix} k_1^2 = k_p^{(1)2} + \gamma_p^{(1)2} \\ k_2^2 = k_p^{(1)2} + \gamma_p^{(2)2} \\ k_3^2 = k_p^{(1)2} + \gamma_p^{(3)2} \end{bmatrix} \quad (\text{A. 13})$$

be satisfied by the separation constants $\gamma_p^{(1)}$, $\gamma_p^{(2)}$ and $\gamma_p^{(3)}$.

The three equations (A. 13) can be used to eliminate all the constants of separation in terms of $k_1^{(1)2}$ and the known wave numbers k_1 , k_2 and k_3 .

It is already known that the losses have a "small" (less than 20%) effect on the wave numbers $\left(\gamma_p^{(1)}, k_p^{(1)}\right)$ of the acoustic mode. Thus, $k_p^{(1)}$ is of the order of the cavity radius for the first mode ($p = 0$) in Eq. (A. 13). The higher p 'th order modes are radial modes which travel even slower than the zero order mode. That is, for $p > 0$

$$k_p^{(1)2} = k_1^2 - \gamma_p^{(1)2} < k_1^2. \quad (\text{A. 14})$$

Therefore, the approximations

$$\gamma_p^{(2)2} = \frac{k_2^2}{1 + \left(\frac{k_p^{(1)}}{\gamma_p^{(2)}}\right)^2} \sim k_2^2 \left(\frac{k_1}{k_2}\right)^2 \quad (\text{A. 15})$$

$$\gamma_p^{(3)2} = \frac{k_3^2}{1 + \left(\frac{k_p^{(1)}}{\gamma_p^{(3)}}\right)^2} \sim k_3^2 \left(\frac{k_1}{k_3}\right)^2 \quad (\text{A. 16})$$

can be made. These approximations have been explored above (see Table A. 2). However, the theory can be worked through with the approximate radial wave numbers and a correction made using these answers which will be good to $\sim \left(\frac{k_1}{k_2}\right)^4$.

The boundary conditions are determined by the physical processes which are taking place. Energy and momentum exchange at the wall must be taken into account at low densities (~ 1 amagat) and high precisions (~ 1 pt in 10^{-4} in linewidth). Acoustic transmission into the walls of the cavity becomes important at elevated densities (~ 100 amagat). These phenomena cause the fluctuating components of the particle velocity and temperature to be different from zero on the cavity walls.

The radial component of the particle velocity at the wall (\dot{r}_w) differs from zero mainly due to the acoustic propagation into the walls of the wave guide.* This problem is quite complex to solve in general.^{3,4} However, the dependence of these losses and ρc can be shown. The frequency or ρc dependence of the acoustic transmission losses can be used to determine the corresponding increment in linewidth experimentally. The transmission losses can be estimated to within an order of magnitude⁵ by assigning a modulus $Y = \rho_w c_w^2$ to the walls. The modulus is defined by

$$\dot{r} \Big|_w = 2 \pi i \omega a \frac{p}{\rho_w c_w^2} \quad (A.17)$$

Here, a is the cavity radius, ρ_w the wall density and c_w the sound speed based on the modulus Y . The pressure can be eliminated using (A.11), giving us

$$\dot{r} \Big|_w = 2 \pi i \left(\frac{\omega a}{c_w} \right) k_1 \frac{\bar{C}}{C_v} \bar{\gamma} H_1 \frac{\rho c}{\rho_w c_w} \quad (A.18)$$

as the appropriate boundary condition.

The possibility of waves reentering the cavity once they have been transmitted into the wall has been neglected. The contribution of such

waves is of the order of $\left(\frac{\rho c}{\rho_w c_w} \right)^2 \sim 10^{-10} - 10^{-6}$. The effective modulus

of the wall $\rho_w c_w$ will depend on the type of deformation induced on the wall by the pressure in the gas. However, on thick-walled cavities this will always lie somewhere between the longitudinal and the flexural modulus for the wall material. The axial velocity at the wall is not affected much by elastic motion of the wall. This is because the sound speed is much faster in the solid than in the gas. Thus, the pressure in the wall tends to be uniform over the length of the cavity.

However, the axial velocity is different from zero at low pressures due to slip. The axial velocity at the wall is given by⁶

$$\dot{z} = l_v \frac{\partial \dot{z}}{\partial r} \quad (A.19)$$

*The end wall losses due to acoustic transmission affect \dot{z} mainly.

The accommodation length l_v is a few mean free paths in the gas. The particle velocity due to slip is very small and is only important at densities ~ 1 amagat and below.

Similarly, the temperature at the wall depends on thermal accommodation between the gas and the wall. In addition, thermal waves propagate into the wall and cause an additional wall temperature variation. Since the temperature fluctuations do not penetrate the wall very far the one dimensional heat equation⁵

$$\frac{\partial^2 T}{\partial r^2} = \frac{\rho_w C_{vw}}{\lambda_w} \frac{\partial T}{\partial t} \quad (\text{A. 20})$$

describes the heat conduction. The solution to (A. 20) which is zero for $r \rightarrow \infty$ and $T_w e^{i\omega t}$ at the walls is

$$T = T_w \exp \left[i\omega t - \sqrt{\frac{\omega \rho_w C_{vw}}{2 \lambda_w}} (r - a) \right]. \quad (\text{A. 21})$$

Thus, the heat flux into the wall Q_w is

$$Q_w = \lambda_w \left. \frac{\partial T}{\partial r} \right|_{r=a} = \sqrt{\frac{\omega \rho_w C_{vw} \lambda_w}{2}} T_w = \frac{\lambda_w}{l_D} T_w. \quad (\text{A. 22})$$

The heat flux Q_w to the wall through the thin layer of gas with a few mean free paths (l_t) of the wall is

$$Q_w = \frac{\lambda}{l_t} (T - T_w) = \lambda \frac{\partial T}{\partial r} \quad (\text{A. 23})$$

where T is the temperature on the outer edge of the accommodation layer and l_t is the accommodation length. Equation (A. 23) is the boundary condition which must be satisfied by the hydrodynamic waves.

The wall temperature can be eliminated between (A. 22) and (A. 23)

$$T = \left[\frac{\lambda}{\lambda_w} l_D + l_t \right] \frac{\partial T}{\partial r}. \quad (\text{A. 24})$$

Table A. 3. Expression for particle velocity and temperature at the wall.

$$\begin{bmatrix} \dot{r} \\ \dot{z} \\ \theta \end{bmatrix} = \begin{bmatrix} A_p^{(1)} \gamma_p^{(1)} J_1(\gamma_p^{(1)} a) + A_p^{(2)} \gamma_p^{(2)^2} J_1(\gamma_p^{(2)} a) - A_p^{(3)} k_p^{(1)^2} \gamma_p^{(3)} J_1(\gamma_p^{(3)} a) \\ ik_p^{(1)} \left[A_p^{(1)} J_0(\gamma_p^{(1)} a) + A_p^{(2)} J_0(\gamma_p^{(1)} a) - A_p^{(3)} \gamma_p^{(3)} J_0(\gamma_p^{(3)} a) \right] \\ A_p^{(1)} a_1 J_0(\gamma_p^{(1)} a) + a_2 A_p^{(2)} J_0(\gamma_p^{(2)} a) \end{bmatrix} e^{ik_p^{(1)} z} \quad (\text{A. 25})$$

Table A. 4. Simultaneous equations for $A_p^{(n)}$ derived from temperature and particle velocity boundary conditions.

$$\left[\begin{array}{l}
 A_p^{(1)} \left[J_1(\gamma_p^{(1)a}) + i\alpha_s \gamma_p^{(1)} \frac{k_1}{\gamma_p^{(1)}} J_0(\gamma_p^{(1)a}) \frac{\rho c}{\rho_w c_w} \right] \gamma_p^{(1)} + A_p^{(2)} \gamma_p^{(2)} J_1(\gamma_p^{(2)a}) - A_p^{(3)} k_p^{(1)2} \gamma_p^{(3)} J_1(\gamma_p^{(3)a}) \\
 A_p^{(1)} (1 - \gamma_p^{(1)} l_v) J_0(\gamma_p^{(1)a}) + A_p^{(2)} (1 - \gamma_p^{(2)} l_v) J_0(\gamma_p^{(2)a}) - A_p^{(3)} (1 - \gamma_p^{(3)} l_v) \gamma_p^{(3)2} J_0(\gamma_p^{(3)a}) \\
 A_p^{(1)} a_1 \left[1 - \gamma_p^{(1)} \frac{\lambda}{\lambda_w} (l_D + l_t) \right] J_0(\gamma_p^{(1)a}) + A_p^{(2)} a_2 \left[1 - \gamma_p^{(2)} \frac{\lambda}{\lambda_w} (l_D + l_t) \right] J_0(\gamma_p^{(2)a})
 \end{array} \right] = 0$$

(A. 26)

The boundary condition on T thus goes to $T = 0$ as the ability of the wall to absorb heat becomes very large, that is, as $\frac{\lambda}{\lambda_w} \ell_D$ and ℓ_t go to zero. The accommodation length ℓ_t is a few mean free paths long ($\sim 10^{-5}$ cm at S. T. P.). However, as the pressure is dropped ℓ_t rapidly approaches to the thermal wavelength and can no longer be neglected. The thermal diffusion length becomes significant at elevated densities ($\rho \sim 500$ amagats). However, this does not become clear until the boundary conditions are applied.

The potentials from our trial solution (A. 12) can now be put into the expressions for particle velocity and temperature (A. 4-A. 6) to obtain an equation for the allowed values of radial wave number $\gamma_p^{(1)}$. The other constants are already known from the separation conditions (A. 13 and following discussion). The particle velocity and temperature at the wall are given by the equation in Table A. 3 for each value of p. Here we have used the formulas relating J'_0 and J'_1 to J_0 and J_1 to eliminate the derivatives of the Bessel functions. Applying the boundary conditions (A. 18), (A. 19) and (A. 24) to (A. 25) we get a set of simultaneous equations for the $A_p^{(n)}$, shown in Table A. 4.

Notice that the complex parts of (A. 18) have been dropped (the complex radial wave number $\gamma_p^{(1)}$ has been replaced with a real radial wave number γ_p)

$$\alpha_s = 2\pi \frac{\omega r_0}{c_s} \quad (\text{A. 27})$$

used in the boundary condition for \dot{r} (Eq. A. 18). The condition that (A. 26) can be solved for the A_p leads in the usual way to the dispersion relation for $\gamma_p^{(1)}$, which is given in Table A. 5. This relation is very complex as it stands. The approximations of (A. 15) and (A. 16) go a long way towards making it possible to solve the dispersion relation analytically. In addition, the Bessel functions in Eq. (A. 27) can be eliminated if relations such as

$$J'_0 \left(\gamma_p^{(n)} a \right) = \beta_i J_0 \left(\gamma_p^{(n)} a \right) \quad (\text{A. 29})$$

can be found.

Table A. 5. Dispersion relation for acoustic waves in a cylindrical wave guide with slip accommodation and acoustic transmission into the walls.

$$0 = \begin{bmatrix} \left[J_1(\gamma_p^{(1)a}) + i\alpha_s \gamma_p^{(1)} \frac{k}{\gamma_p^{(1)}} J_0(\gamma_p^{(1)a}) \right] \gamma_p^{(1)} & \gamma_p^{(2)} J_1(\gamma_p^{(2)a}) & -k_p^{(1)2} \gamma_p^{(3)} J_1(\gamma_p^{(3)a}) \\ (1 - \gamma_p^{(1)} \ell_v) J_0(\gamma_p^{(1)a}) & (1 - \gamma_p^{(2)} \ell_v) J_0(\gamma_p^{(2)a}) & -(1 - \gamma_p^{(3)} \ell_v) \gamma_p^{(3)2} J_0(\gamma_p^{(3)a}) \\ a_1 \left[1 - \gamma_p^{(1)} \left(\frac{\lambda}{\lambda_w} \ell_D + \ell_t \right) \right] J_0 \gamma_p^{(1)a} & a_2 \left[1 - \gamma_p^{(2)} \left(\frac{\lambda}{\lambda_w} \ell_D + \ell_t \right) \right] J_0(\gamma_p^{(2)a}) & 0 \end{bmatrix} \quad (\text{A.28})$$

CYLINDRICAL WAVE GUIDE DISPERSION RELATION

The classical approximations for the Bessel functions¹ with the arguments $\left(\gamma_p^{(2)} a\right)$ and $\left(\gamma_p^{(3)} a\right)$ are based on the large imaginary parts of $\gamma_p^{(2)}$ and $\gamma_p^{(3)}$. Recalling (A. 15) and k_2^2 from Table A. 1

$$\gamma_p^{(2)} \cong \frac{1+i}{\sqrt{2}} |k_2| \sim (1+i) 10^3 \quad (\text{A. 30})$$

where $|k_2|$ is of the order of 10^3 at about 1 atm and increases with pressure. Thus, the asymptotic expansions of Hankel⁷ should give good approximations here. Using 9. 2. 5 and 9. 2. 11 of Ref. 7, we find letting $z = \gamma_p^{(2)} a$ or $\gamma_p^{(3)} a$

$$\frac{J_1(z)}{J_0(z)} = -\tan\left(z - \frac{\pi}{4}\right) \left[1 + \frac{1-i}{2|z|}\right] O\left(\frac{1-i}{|z|^2}\right) \quad (\text{A. 31})$$

and expanding the tangent in exponentials

$$\tan\left(z - \frac{\pi}{4}\right) = i O\left(e^{-2|z|}\right). \quad (\text{A. 32})$$

Thus, the approximation (A. 31) is good to parts in 10^6 and (A. 32) in parts in e^{-2000} . Thus, the desired β_i for the thermal and viscous waves in (A. 29) are

$$\beta_i = -i \gamma_p^{(i)} \left[1 + \frac{1-i}{2|\gamma_p^{(i)} a|}\right] J_0\left(\gamma_p^{(1)} a\right). \quad (\text{A. 33})$$

The approximation for the acoustic mode $J_1\left(\gamma_p^{(1)} a\right)$ follows from the fact that the acoustic mode is not changed much by losses. Therefore we try an expansion⁽¹⁾ of $J_1\left(\gamma_p^{(1)} a\right)$ in a series consisting of the solutions $J_0\left(\gamma_p^{(1)} a\right)$ to the cylindrical wave guide problem. Thus, from standard formulas for expansions in Bessel functions⁷

$$J'_o(\gamma_p^{(1)r}) = \sum A_n J'_o(\gamma_n r) \quad (\text{A. 34})$$

where

$$A_n = \frac{1}{\frac{a}{2} J_o^2(\gamma_n r)} \int_0^a r J_o(\gamma_p^{(1)r}) J(\gamma_n r) dr. \quad (\text{A. 35})$$

The integration indicated in (A. 35) may be carried out. In addition, we can use the boundary condition for lossless waves $J'_o(\gamma_n a) = 0$.

The expansion (A. 34) then becomes, after solving for $J'_o(\gamma_p^{(1)a})$ (which comes from the integral in (A. 35))

$$J'_o(\gamma_p^{(1)a}) = \beta_1 J_o(\gamma_p^{(1)a}) \quad (\text{A. 36})$$

where

$$\beta_1 = -\frac{a}{2} (\gamma_p^{(1)2} - \gamma_p^2) \left[1 + \sum_{n \neq p} \frac{\gamma_p^{(1)2} - \gamma_p^2}{\gamma_n^{(1)2} - \gamma_n^2} \right]^{-1}. \quad (\text{A. 37})$$

The term in brackets is always less than $\frac{1}{2} \frac{k_1}{k_2} \sim 10^{-3}$ and decreases

with increasing pressure and frequency. In addition, the summation in (A. 25) rapidly approaches 1 as the radial mode number p becomes larger than $p = 1$.

EXPRESSIONS FOR $\gamma_p^{(1)}$ AND $k_p^{(1)}$

The dispersion relation (A. 28) can now be simplified to

$$k_1 \begin{bmatrix} \left[\beta_1 + i \alpha_s \gamma k_1 \left(\frac{\rho c}{\rho_w c_w} \right) \right] & \beta_2 & -k_p^{(1)2} \beta_3 \\ (1 - \gamma_p^{(1)} \ell_v) & (1 - \gamma_p^{(2)} \ell_v) & -(1 - \gamma_p^{(3)} \ell_r) \gamma_p^{(3)2} \\ a_1 \left[1 - \gamma_p^{(1)} \left(\frac{\lambda}{\lambda_w} \ell_D + \ell_t \right) \right] & \left[a_2 1 - \gamma_p^{(2)} \left(\frac{\lambda}{\lambda_w} \ell_D + \ell_t \right) \right] & 0 \end{bmatrix} = 0 \quad (\text{A. 38})$$

The dispersion relation solved for β_1 in a way which makes all the corrections due to nonideal boundary condition clear, becomes

$$\beta_1 = - \frac{1 - \gamma_p^{(1)} \ell_v}{1 - \gamma_p^{(3)} \ell_v} k_p^{(1)2} \frac{\beta_3}{\gamma_p^{(3)2}} + \frac{1 - \gamma_p^{(1)} \left(\frac{\lambda}{\lambda_w} \ell_D + \ell_t \right)}{1 - \gamma_p^{(2)} \left(\frac{\lambda}{\lambda_w} \ell_D + \ell_t \right)} \left[\frac{a_1}{a_2} \beta_2 - \left(\frac{1 - \gamma_p^{(1)} \ell_v}{1 - \gamma_p^{(2)} \ell_v} \right) \frac{a_1}{a_2} \beta_3 \frac{k_p^{(1)2}}{\gamma_p^{(3)2}} \right] - i \alpha_s \gamma k_1 \frac{\rho c}{\rho_w c_w} \quad (\text{A. 39})$$

The first term on the right-hand side of (A. 39) consists of the viscous "losses". $\gamma_p^{(1)} \ell_v$ can be neglected to parts in 10^5 here. The

effect of the momentum accommodation length is to increase* the viscosity by a factor

$$\left[1 - \gamma_p^{(3)} \ell_v \right]^{-2} . \quad (\text{A. 40})$$

This factor can easily be 1% in a small cavity at ~ 1 atm. However, it is at most 0.1% for the conditions of the present work.

The second term is the thermal conduction term plus a second order term involving viscous and thermal effects. The accommodation

effects in this second order term $\frac{1 - \gamma_p^{(1)} \ell_v}{1 - \gamma_p^{(2)} \ell_v}$ can be dropped to parts

in 10^5 in thermal conductivity. The effect of thermal capacity of the wall and thermal accommodation at the surface of the wall is to increase the thermal conductivity by the factor

$$\left[1 - \gamma_p^{(2)} \left(\frac{\lambda}{\lambda_w} \ell_D + \ell_t \right) \right]^{-2} . \quad (\text{A. 41})$$

The effect of thermal accommodation ℓ_t is important only at the lower pressures as indicated above for momentum accommodation. The thermal length ℓ_D of the wall is small (parts in 10^{-6}) at about 1 amagat. However, at 500 amagats it rises to about 1 pt in 10^{-4} .

The final term in (A. 39) is the loss to the side wall by acoustic transmission. This relation ignores any frequency or wavelength behavior due to the geometry of the cavity side walls. However, it shows the major frequency and ρc dependence of linewidth. This can be used in practice to compensate the linewidth measurements for acoustic transmission losses at elevated densities as described in the text of this report.**

* As is seen below $\frac{\beta_3}{\gamma_p^{(3)}} \propto \sqrt{\frac{\eta}{\rho}}$ and $\frac{\beta_2}{a_2} \propto \sqrt{\frac{\lambda}{\rho}}$.

** Notice that $\gamma_p^{(3)} \ell_v \sqrt{\frac{\eta}{\rho}} \propto \rho$ so that accommodation can be handled the same way!

Since we can easily restore the slip, accommodation and thermal capacity corrections by modifying viscosity with (A. 40) and thermal conductivity with (A. 41), we will no longer carry these terms in our algebra. The dispersion relation then becomes

$$\gamma_p^{(1)} - \gamma_p = \frac{2}{a} \left[k_p^{(1)2} \frac{\beta_3}{\gamma_p^{(3)2}} + k_1^2 \frac{\beta_2}{k_2^2} (\bar{\gamma}-1) + k_1^2 (\bar{\gamma}-1) \frac{\beta_3}{\gamma_p^{(3)2}} \frac{k_p^{(1)2}}{k_2^2} \right] \times$$

$$\times \left[1 + \sum_{p \neq n} \frac{\gamma_p^{(1)2} - \gamma_p^2}{\gamma_n^{(1)2} - \gamma_p^2} \right] + i \alpha_s \gamma k_1 \frac{\rho c}{\rho_w c_w} \tag{A. 42}$$

where we have used

$$\frac{a_1}{a_2} = - \left(\frac{k_1}{k_2} \right)^2 (\bar{\gamma}-1) \left(\frac{1 - \frac{\bar{\epsilon}}{\gamma-1}}{1 - \left(\frac{k_1}{k_2} \right)^2} \right) \tag{A. 43}$$

In fact, many of the second order terms can be considered corrections to the viscosity and thermal conductivity in the manner discussed above for accommodation and slip. The total correction factors for viscosity and thermal conductivity are shown in Table A. 6. The remaining expression for the radial wave number is

$$\gamma_p^{(1)} - \gamma_p = \frac{2}{a} \left[\frac{\gamma_p^{(1)2} - k_1^2}{k_3} + (\bar{\gamma}-1) \frac{k_1^2}{k_2} + (\bar{\gamma}-1) \frac{k_1^2}{k_3} \left(\frac{k_1^2}{k_2^2} \right) \right] + i \alpha_s \gamma k_1 \frac{\rho c}{\rho_w c_w} \tag{A. 44}$$

The expression (A. 44) is the basis of the first order wave number expressions. The true viscosities and thermal conductivities must be corrected by the factors in Table A. 6 in order to obtain wave numbers correct to second order and for nonideal boundary conditions. Typically, at 300°K, 1 atm and $f_{01} \sim 50$ kHz the correction factors amount to $\sim 0.5\%$ in viscosity and decreases with increasing pressure.

Table A. 6. Second order correction factors for nonideal acoustic wave guide
in p'th radial mode.

Multiply True	by to get corrected wave numbers
Viscosity	$\left[1 + \sum_{p \neq n} \frac{\left(\frac{\omega}{c}\right)^2 \epsilon_{sp}}{\gamma_n^3 - \gamma_p^2} \right] \left[1 + \frac{1}{ k_3 a } \right] \left[1 + 2 k_3 \ell_v \right]$
Thermal Conductivity	$\left[1 + \sum_{p \neq n} \frac{\left(\frac{\epsilon}{c}\right)^2 \epsilon_{sp}}{\gamma_n^2 - \gamma_p^2} \right] \left[1 + \frac{\gamma-1}{ k_2 a } \right] \left[1 + 2 k_2 \left(\frac{\lambda}{\lambda_w} \ell_D + \ell_t\right) \right]$

The wave numbers for traveling acoustic waves in a cylindrical wave guide are to the first order

$$\gamma_p^{(1)2} = \gamma_p^2 + \frac{1-i}{2} k_1^2 \epsilon_{sp} + i \alpha_s \gamma k_1 \frac{\rho c}{\rho_w c_w} \quad (A. 45)$$

and from Eq. (A. 13)

$$k_p^{(1)2} = k_1^2 - \gamma_p^2 - \frac{1-i}{2} k_1^2 \epsilon_{sp} - i \alpha_s \gamma k_1 \frac{\rho c}{\rho_w c_w} \quad (A. 46)$$

where

$$\epsilon_s = \left[\left(\frac{\gamma_p}{k_1} \right)^2 - 1 \right] \sqrt{\frac{\eta}{\omega \rho}} + (\tilde{\gamma} - 1) \sqrt{\frac{\lambda}{\omega \rho C_p}} \quad (A. 47)$$

The imaginary part of $k_p^{(1)}$ is the absorption coefficient for pth mode acoustic wave propagating down a cylindrical wave guide. The real part of $k_p^{(1)}$ is the wave number (frequency/propagation speed) for such waves. The $\gamma_p^{(1)}$ form an infinite set of allowed complex wave numbers closely following the allowed real wave numbers of the lossless wave guide problem. These real wave numbers are the successive roots of the first order Bessel functions and satisfy the equation

$$J_1(\gamma_p a) = 0 \quad (A. 48)$$

We can now make an orthogonal set of wave functions out of the acoustic mode wave functions from which all acoustic disturbances in a cylindrical wave guide can be made.

THE EFFECTS OF THE SOUND SOURCE

The amplitude of the modes $A_p^{(i)}$ is determined by the velocity versus radial distance on a source located at $z = 0$ in the wave guide.

The functions $\phi_p = J_0(\gamma_p^{(1)} r) e^{i k_p^{(1)} z}$ satisfy the boundary conditions

on the side wall already. Thus, if we make a sum of ϕ_p which satisfy the boundary conditions on the end wall at the source we get solutions which satisfy the wave equations and boundary conditions everywhere. Transducers

which cause \dot{z}_o to vary only with r at the source are used in the present work. The expansion of \dot{z}_o in ϕ_p can be accomplished to give

$$\dot{z} = \sum G_p \phi_p. \quad (\text{A. 49})$$

Here, we have not assumed that the ϕ_p are orthogonal. They are not because $\gamma_p^{(1)}$ has imaginary parts. However, in practice, linear sums of the ϕ_p can be found which are orthogonal and these functions used to uniquely calculate the G_p of Eq. (A. 49). This fine point is not important for the cavity because as already noted the ϕ_p are almost orthogonal. However, for the coupling hole problem (a $\sim k_2$ or k_3) orthogonalization is necessary as is discussed in Appendix C.

Transducers at $z = 0$ whose particle velocity matches the particle velocity of the p th mode exactly will generate only ϕ_p . Thus, from a physical point of view we can insist that each ϕ_p satisfy the boundary conditions on the source wall separately. Plane viscous and thermal wave propagation in the z direction are required to satisfy the boundary conditions at the wall in the presence of the acoustic wave ϕ_p . Thus our trial solution (A. 12) becomes

$$\begin{bmatrix} H_1 \\ H_2 \\ H_3 \end{bmatrix} = \begin{bmatrix} A_p^{(1)} J_0(\gamma_p^{(1)} r) e^{ik_p^{(1)} z} \\ B_p^{(2)} J_0(\gamma_p^{(1)} r) e^{ik_p^{(2)} z} \\ B_p^{(3)} J_0(\gamma_p^{(1)} r) e^{ik_p^{(3)} z} \end{bmatrix} \quad (\text{A. 50})$$

Note that we have not used the radial viscous and acoustic modes since $J_0(\gamma_p^{(1)} r)$ vanish over most of the end wall (for $r > \frac{1}{k_2}$). More is said about this below.

Analogous to Eqs. (A. 18), (A. 19), (A. 20) the boundary conditions on the source wall for the p th radial mode are set forth in Table A. 7.

Table A. 7. Boundary conditions for acoustic source wall.

$$\begin{array}{l}
 \dot{r} \\
 \dot{z} \\
 T
 \end{array}
 \Bigg|_{z=0}
 =
 \begin{array}{l}
 \ell_v \frac{\partial \dot{r}}{\partial z} = \left[ik_p^{(1)} \ell_v A_p^{(1)} + ik_p^{(2)} \ell_v B_p^{(2)} - ik_p^{(3)} \ell_v B_p^{(3)} \right] \gamma_p^{(1)} J_1(\gamma_p^{(1)} r) \\
 G_p J_0(\gamma_p r) \\
 \left(\frac{\lambda}{\lambda_w} \ell_D + \ell_t \right) \frac{\partial T}{\partial t} = -i \left[a_1 k_p^{(1)} \left(\frac{\lambda}{\lambda_w} \ell_D + \ell_t \right) A_p^{(1)} + a_2 k_p^{(2)} \left(\frac{\lambda}{\lambda_w} \ell_D + \ell_t \right) B_p^{(2)} \right] J_0(\gamma_p^{(1)} r)
 \end{array}
 \Bigg|_{z=0}
 \quad (A.51)$$

The differences in the end wall and side wall conditions are due to interchange of \dot{r} and \dot{z} as the tangential and normal velocity components. In addition, the normal velocity is specified by transducer design in the coupling coefficient G_p .

The velocity components in the gas just outside the accommodation lengths are obtained by substituting our trial solution (A. 12) (with $J(\gamma_p^{(i)} r)$, $i = 2, 3$ suppressed) into Eqs. (A. 4), (A. 5) and (A. 6) and evaluating them at $z = 0$. The boundary conditions in the gas become

$$\begin{bmatrix} \dot{r} \\ \dot{z} \\ T \end{bmatrix}_{z=0} = \begin{bmatrix} \left[A_p^{(1)} + B_p^{(2)} - k_p^{(3)^2} B_p^{(3)} \right] \gamma_p^{(1)} J_1(\gamma_p^{(1)} r) \\ i \left[k_p^{(1)} A_p^{(1)} + k_p^{(2)} B_p^{(2)} + \gamma_p^{(1)^2} k_p^{(3)} B_p^{(3)} \right] J_0(\gamma_p^{(1)} r) \\ \left[a_1 A_p^{(1)} + a_2 B_p^{(2)} \right] J_0(\gamma_p^{(1)} r) \end{bmatrix} \quad (A. 52)$$

Finally, setting (A. 52) and (A. 51) equal to one another a set of simultaneous equations for $A_p^{(1)}$, $B_p^{(2)}$ and $B_p^{(3)}$ are obtained

$$A_p^{(1)} \left[1 - ik_p^{(1)} \ell_v \right] + B_p^{(2)} \left[1 - ik_p^{(2)} \ell_v \right] - B_p^{(3)} k_p^{(3)^2} \left[1 - ik_p^{(3)} \ell_v \right] = 0$$

$$A_p^{(1)} k_p^{(1)} + B_p^{(2)} k_p^{(2)} + B_p^{(3)} \gamma_p^{(1)^2} k_p^{(3)} = -iG_p \quad (A. 53)$$

$$A_p^{(1)} a_1 \left[1 - ik_p^{(1)} \left(\frac{\lambda}{\lambda_w} \ell_D + \ell_t \right) \right] + B_p^{(2)} a_2 \left[1 - ik_p^{(2)} \left(\frac{\lambda}{\lambda_w} \ell_D + \ell_t \right) \right] = 0$$

The amplitude of the wave excited by the source transducer $A_p^{(1)}$ can be found by solving (A. 53) by Cramer's rule. After neglecting $\frac{a_1}{a_2}$ ($\sim 10^{-6}$) compared to an expression formally equivalent to Fritsche's equation (33) (Ref. A. 1)

$$A_p^{(1)} = \frac{-iG_p}{k_p^{(1)} + h} \tag{A. 54}$$

is obtained. However, h , including nonideal boundary conditions, is

$$h = \frac{1 - ik_p^{(1)} l_v}{1 - ik_p^{(3)} l_v} \frac{\gamma_p^{(1)2}}{k_p^{(3)}} + \frac{1 - ik_p^{(1)} \left(\frac{\lambda}{\lambda_w} l_D + l_t \right) k_1^2}{1 - ik_p^{(2)} \left(\frac{\lambda}{\lambda_w} l_D + l_t \right) k_2^2} \tag{A. 55}$$

and $k_p^{(1)}$ contains all the second order terms discussed in the last paragraph. The most significant point about (A. 54) is that every time $k_p^{(1)} \rightarrow 0$ (recal = (A. 46)) the amplitude $A_p^{(1)}$ gets very large. Thus, frequencies where $k_1 = |\gamma_p|$ are radial resonances. The coupling coefficient is not strongly dependent on frequencies because we had to design a "broadband" transducer for the application under study. However, multiple reflections between opposing walls will pull the resonance predicted by (A. 54). In addition, the radial resonance goes as $k_p^{(1)2}$ in a cavity which is easier to calculate than the $k_p^{(1)}$ dependence in an infinite wave guide. Therefore, the multiple reflection problem in a cavity with two end walls will be done before the modes are identified in detail.

MULTIPLE REFLECTIONS AND CAVITY RESONANCES

Walls at the end of the wave guide cause the waves to reflect back and forth. The total field at any point is the sum of all the multiple reflections. The basic traveling acoustic mode wave is incident on the end wall and gives rise to a reflected wave. The potential for the acoustic mode is

$$H_1 = A_p^{(1)} J_0 \left(\gamma_p^{(1)} r \right) e^{ik_p^{(1)} z} + B_p^{(1)} J_0 \left(\gamma_p^{(1)} r \right) e^{-ik_p^{(1)} (z-d)} \tag{A. 56}$$

Near the end wall ($z = d$) the plane viscous and thermal waves are from (A. 12)

$$H_3 = B_3^{(3)} J_0(\gamma_p^{(1)} r) e^{-ik_p^{(3)}(z-d)} \tag{A. 57}$$

$$H_2 = B_2^{(2)} J_0(\gamma_p^{(1)} r) e^{-ik_p^{(2)}(z-d)}$$

The velocity and temperature can be calculated just outside the accommodation layer using (A. 4) through (A. 6) to get

$$\begin{bmatrix} \dot{r} \\ \dot{z} \\ \theta \end{bmatrix}_{z=d} = \begin{bmatrix} -\gamma_p^{(1)} J_1(\gamma_p^{(1)} r) \left(A_p^{(1)} e^{-ik_p^{(1)}d} + B_p^{(1)} + B_p^{(2)} - k_p^{(3)2} B_p^{(2)} \right) \\ -i J_0(\gamma_p^{(1)} r) \left(k_p^{(1)} A_p^{(1)} e^{ik_p^{(1)}d} - k_p^{(1)} B_p^{(1)} - k_p^{(1)} B_p^{(2)} - \gamma_p^{(1)2} k_p^{(3)} B_p^{(3)} \right) \\ J_0(\gamma_p^{(1)} r) \left(A_p^{(1)} a_1 e^{ik_p^{(1)}d} + B_p^{(1)} a_1 \right) \end{bmatrix} \tag{A. 58}$$

The boundary conditions on \dot{r} and T are the same as those given in (A. 51). However, the \dot{z} boundary condition must be modified for acoustic transmission which is similar to (A. 18)

$$\dot{z} = i\alpha_E \omega k_1 \bar{\gamma} - \frac{\rho c}{\rho_w c_w} \tag{A. 59}$$

Here α_E is a constant of proportionality which depends on how the end wall is clamped and its geometry. One of the problems encountered experimentally is that plate resonances in the end walls must be avoided. Otherwise α_E is not a constant and it is not possible to separate cavity resonances from end wall resonances. As before, the velocity and temperature in the gas can be set equal to the velocity and temperature at the wall to give a set of equations for the reflection coefficients r

$$\frac{B_p^{(i)}}{A_p^{(1)}} = r_i \text{ Thus (A. 58) becomes}$$

$$\begin{aligned} & \left(1 - ik_p^{(1)} \ell_v\right) r_1 + \left(1 - ik_p^{(2)} \ell_v\right) r_2 - k_p^{(3)2} \left(1 - ik_p^{(3)} \ell_v\right) r_3 \\ & = \left(1 - ik_p^{(1)} \ell_v\right) e^{ik_p^{(1)} d} \end{aligned}$$

$$\begin{aligned} & \left(1 - \alpha_E \omega k_1 \bar{\gamma} \frac{\rho c}{\rho_w c_w}\right) k_p^{(1)} r_1 + k_p^{(2)} r_2 + k_p^{(3)} \gamma_p^{(1)2} r_3 \\ & = \left(1 - \alpha_E \omega k_1 \bar{\gamma} \frac{\rho c}{\rho_w c_w}\right) e^{k_p^{(1)}} \end{aligned} \tag{A. 60}$$

$$\begin{aligned} & a_1 \left[1 - k_p^{(1)} \left(\frac{\lambda}{\lambda_w} \ell_D + \ell_t\right)\right] r_1 + a_2 \left[1 - k_p^{(2)} \left(\frac{\lambda}{\lambda_w} \ell_D + \ell_t\right)\right] r_3 \\ & = a_1 \left[1 - k_p^{(1)} \left(\frac{\lambda}{\lambda_w} \ell_D + \ell_t\right)\right] e^{ik_p^{(1)}} \end{aligned}$$

Solving for the reflection coefficient by Cramer's rule, we get

$$r_1 = \frac{\epsilon_+ k_p^{(1)} - h}{\epsilon_- k_p^{(1)} + h} e^{ik_p^{(1)} d} = e^{ik_p^{(1)} d} \tag{A. 61}$$

where ϵ_+ and ϵ_- are given by

$$\epsilon_{\pm} = 1 \pm i \alpha_E k_1 \bar{\gamma} \left(\frac{\rho c}{\rho_w c_w}\right). \tag{A. 62}$$

Thus, a wave of amplitude $A_p^{(1)}$ originating at $z = 0$ incident on an end wall located at $z = d$ gives rise to a reflected wave of amplitude $r_1 A_p^{(1)}$ at the end wall. Notice the effect of traveling a distance d along the wave guide has been in the reflection coefficient. In addition, $k_p^{(1)}$, ϵ_+ , and ϵ_- have been defined for algebraic convenience.

The field in the cavity is sensed at the opposite wall from the source wall ($z = d$). The requirement for isolation of the transducer from the cavity leads to a large coupling loss between the input signal and the output signal. Electrical feedthrough is minimized by sensing the field in the cavity at $z = d$. The total wave traveling toward the end wall is

$$A_p^{(1)} e^{ik_p^{(1)}d} + A_p^{(1)} e^{ik_p^{(1)}d} e^{i2k_p^{(1)}d} + \dots = \frac{A_p^{(1)} e^{ik_p^{(1)}d}}{1 - 2e^{ik_p^{(1)}d}} \quad (\text{A. 63})$$

Similarly, the sum of the reflected waves at $z = d$ is

$$A_p^{(1)} e^{ik_p^{(1)}d} + A_p^{(1)} e^{i3k_p^{(1)}d} + \dots = \frac{A_p^{(1)} e^{ik_p^{(1)}d}}{1 - 2e^{ik_p^{(1)}d}} \quad (\text{A. 64})$$

The total excitation at $z = d$ is the sum of the incident and reflected waves

$$H_1 \Big|_{z=d} = A_p^{(1)} \frac{\left(e^{ik_p^{(1)}d} + e^{ik_p^{(1)}d} \right)}{1 - 2e^{ik_p^{(1)}d}} = \frac{(\epsilon_- + \epsilon_+) k_p^{(1)}}{2i(\epsilon_- k_p^{(1)} + h)(\epsilon_- k_p^{(1)} - h)} \frac{G_p}{\sin k_p^{(1)}d} \quad (\text{A. 65})$$

The sum of two angle formulas and the definition of $k_p^{(1)}$ can be used to give (note $\epsilon_+ + \epsilon_- = 1$)

$$\sin k_p^{(1)d} = \frac{k_p^{(1)}}{(\epsilon_- k_p^{(1)} + h)(\epsilon_- k_p^{(1)} - h)} \left[k_p^{(1)} \sin k_p^{(1)d} - (\epsilon_+ - \epsilon_-) h \sin k_p^{(1)h} + \frac{h^2}{k_p^{(1)}} \sin k_p^{(1)d} - i h \cos k_p^{(1)d} + i \frac{\epsilon_+ - \epsilon_-}{2} k_p^{(1)} \cos k_p^{(1)d} \right] \quad (\text{A. 66})$$

The final expression for line shape of a cavity is

$$H_1 = \frac{-G_p J_0(\gamma_p r)}{\left[k_p^{(1)} + \frac{h^2}{k_p^{(1)}} - (\epsilon_+ - \epsilon_-) h \right] \sin k_p^{(1)d} - i \left[h - \frac{\epsilon_+ - \epsilon_-}{2} k_p^{(1)} \right] \cos k_p^{(1)d}} \quad (\text{A. 67})$$

where we have used (A. 56) and (A. 65) to simplify (A. 66).

The working relations for the transport property determinations require further approximations to reduce (A. 67) to a manageable form. The general magnitude of the various terms indicates how such approximations can be made. When the real part of $k_p^{(1)d} = n\pi$ $n = 0, 1, \dots$ the real part of the denominator of (A. 67) becomes very small and the resonate buildup of amplitude is observed. The radial resonances of the cavity occur when $n = 0$. That is, every time the excitation frequency is

$$\left(\frac{\omega_{op}}{c} \right)^2 \cong k_1^2 \cong \gamma_p^2 \quad (\text{A. 68})$$

as indicated by Eq. (A. 45). The longitudinal modes occur for $n \neq 0$ $\gamma_p = 0$, so that

$$\left(\frac{\omega_{no}}{c} \right)^2 \cong \left(\frac{n\pi}{d} \right)^2$$

The compound modes are obtained when $n \neq 0$ and $\gamma_p \neq 0$, that is, the index $p \neq 0$

$$\frac{\omega_{np}^2}{c} \cong \frac{n\pi}{d} - \gamma_p^2 \quad (A.69)$$

The approximate signs are used because we have neglected small changes in resonant frequency due to losses in the cavity. In fact, if we collected all the real terms of the denominator in Eq. (A.67) and set them equal to zero we would find that the effect of the first order correction is to lower the resonant frequency by one-half the cavity linewidth.

The wave number $k_p^{(1)}$ for longitudinal and compound modes has a large $\left(|k_p^{(1)}| \sim 1 \text{ cm}^{-1} \right)$ real part and a small $\left(\text{Im } k_p^{(1)} < 10^{-3} \right)$ imaginary part. Therefore, we can factor out $k_p^{(1)}$ from the denominator of (A.67) to give

$$H_1 = \frac{1}{k_p^{(1)}} \frac{-G_p J_0(\gamma_p r)}{\left[1 + \left(\frac{h}{k_p^{(1)}} \right)^2 + (\epsilon_+ - \epsilon_-)h \right] \sin k_p^{(1)} d - i \left[\frac{h}{k_p^{(1)}} - \frac{\epsilon_+ - \epsilon_-}{2} \right] \cos k_p^{(1)} d} \quad (A.70)$$

The transcendental terms in the denominator of (A.70) may be written

$$\sin(k_p^{(1)} d) = \sin \left(k_p^{(1)} - \frac{n\pi}{d} \right) d \quad (A.71)$$

and

$$\cos k_p^{(1)} d = (-1)^n \cos \left(k_p^{(1)} - \frac{n\pi}{d} \right) d \quad (A.72)$$

Near longitudinal or radial resonance these arguments become small and Taylor expansion approximations can be used.

The arguments of (A.71) and (A.72) can be written with the help of (A.46) and (A.47)

$$\left(k_p^{(1)} - \frac{n\pi}{d} \right) d = \frac{\omega^2 - \omega_{pn}^2}{\omega_n^2} n\pi - \frac{i}{2} \frac{k_1}{\sqrt{k^2 - \gamma_p^2}} \left[\epsilon_s + \alpha_s \gamma \frac{\rho c}{\rho_w c_w} + \omega \delta_v \right] d \quad (A.73)$$

near the resonant frequency. The real part of (A. 73) is of the order* of $\frac{\delta}{2\omega_n} \sim 10^{-4}$, the imaginary part is of the order of 10^{-3} . Thus, (A. 71) and (A. 72) become

$$\sin k_p^{(1)} d = k_p^{(1)} d \left[1 - \frac{(k_p^{(1)} d)^2}{31} \right] = k_p^{(1)} d + 0 (10^{-6}) \quad (\text{A. 74})$$

and

$$\cos k_1^{(1)} d = \left[1 - \frac{(k_p^{(1)} d)^2}{21} \right] = 1 - 0 (10^{-6}) . \quad (\text{A. 75})$$

The line shape within one linewidth of the center frequency reduces to

$$H_1 = \frac{1}{k_p^{(1)}} \frac{-G_p J_0(\gamma_p r)}{\left(k_p^{(1)} - \frac{n\pi}{d}\right) d - i \left(\frac{h_1}{k_p^{(1)}} + \frac{\epsilon_+ - \epsilon_-}{2}\right)} \quad (\text{A. 76})$$

The linewidth can be identified by using (A. 73) to put (A. 76) into the form

$$H_1 = \frac{\omega_n^2}{k_p^{(1)} (\omega + \omega_{pn}) n\pi} \frac{-G_p J_0(\gamma_p r)}{\omega - \omega_{pn} + i\delta} \quad (\text{A. 77})$$

where to the first order

$$\delta = \omega_{pn}^{1/2} \delta_{pn} + (\alpha_E + \alpha_s) \frac{\omega}{\sqrt{\omega^2 - \omega_{po}^2}} \gamma \frac{\rho c}{\rho_w c_w} . \quad (\text{A. 78})$$

This linewidth is the frequency difference between 45° phase shift points. The second order terms are again lumped into multipliers correcting the viscosity and thermal conductivity. The total correction terms including those originally noted in Table A. 6 are given in Table A. 8.

* δ is the linewidth.

Table A. 8. Total second order correction factor for viscosity and thermal conductivity in cavity linewidth expressions.

Multiply True	by to get corrected viscosity and thermal conductivity in linewidth
Viscosity	$\left\{ \left[1 + \sum_{p \neq n} \frac{\left(\frac{\omega}{c}\right)^2 \epsilon_{sp}}{\gamma_n^2 - \gamma_p^2} + \frac{1}{ k_3 a } \right] + \left[1 + \left(\frac{\delta d}{c}\right)^2 \right] \right\} \left[1 + 2 \left(k_3 + \sqrt{\left(\frac{\omega}{c}\right)^2 - \gamma_p^2} \right) l_v \right]$
Thermal Conductivity	$\left\{ 1 + \sum_{p \neq n} \frac{\left(\frac{\omega}{c}\right)^2 \epsilon_{sp}}{\gamma_n^2 - \gamma_p^2} + \frac{\gamma-1}{ k_2 a } \left[1 + \left(\frac{\delta d}{c}\right)^2 \right] \right\} \left[1 + 2 \left(k_2 + \sqrt{\left(\frac{\omega}{c}\right)^2 - \gamma_p^2} \right) \left(\frac{\lambda}{\lambda_w} l_D + l_t \right) \right]$

The radial mode linewidth required a slightly different approach because $k_p^{(1)} \rightarrow 0$ fast resonance made the Taylor expansion (A. 73)

impossible. The wave number $k_p^{(1)} d$ goes to $\sim \frac{\omega^2 - \omega_{p0}^2}{\omega_{01}^2} < 10^{-2}$ for

the first radial mode. The small angle approximations can be made for $\sin k_p^{(1)} d$ and $\cos k_p^{(1)} d$. The line shape near the line center (A. 67) in the present approximation is

$$H_1 = \frac{-G_p J_0(\gamma_p r)}{\frac{\omega^2 - \omega_{p0}^2}{\omega_{01}^2} - i \left[\left(\frac{\omega}{c} \right) \epsilon_s + h + \alpha_s \gamma \frac{\omega}{a} \frac{\rho c}{\rho_w c_w} \right]} \quad (A. 79)$$

The linewidth is found as before to be

$$\delta = \omega_{p0}^{1/2} \delta_{p0} + \alpha_s \gamma \frac{\omega}{c} d \frac{\rho c}{\rho_w c_w} \quad (A. 80)$$

The second order terms considered as corrections to viscosity are given in Table A. 8 for the radial mode.

REFERENCES

- A1. Theorie Des Akus.Tischen Zylinderresona Tors Unter Berücksichtigung Der Schallanregung 11, L. Fritsche, Acustica 10, 1960, pp.199-207.
- A2. Research Study and Experimental Program to Determine the Transport Properties of High Temperature and High Density Gases, C. Carey, J. H. Bradshaw, E. H. Carnevale, AEDC-TR-71-191 (1971).
- A3. Systematic Errors in Ultrasonic Propagation Parameter Measurements, V. A. Del Grosso, NRL Rpt. 6852, 1968.
- A4. Systematic Errors in Ultrasonic Propagation Parameter Measurements, V. A. Del Grosso, NRL Rpt. 6133, 1965.
- A5. The Tube Effect in Sound Velocity Measurements, P. S. Henry, Proc. Royal Soc. 43, p.540, 1931.
- A6. Statistical Mechanics, K. Wang, John Wiley & Sons, New York, p.110.
- A7. Advanced Calculus for Applications, F. B. Hildebrand, Prentice-Hall, New Jersey, 1962.
- A8. Handbook of Mathematical Functions, M. Abramowitz and A. Stengun, NBS App. Math. Series 55, 1964, p.364.

APPENDIX B

EFFECTS OF MULTIPLE WAVES IN COUPLING HOLES

The sound is coupled into the cavity through small holes. The coupling holes are themselves wide band resonators. That is, short cylindrical wave guides terminated on one side by the electrostatic transducer and on the other side by a large change in radius. Both terminating impedances reflect most of the energy incident on them. The lowest resonant frequency of the coupling holes is (from three to six times) well above the cavity resonances. In addition, because of the small diameter the losses are 50 times greater than the cavity losses. The Q of the coupling holes is at most 0.1 times the cavity, Q.

The cavity plus transducers consist of finite cylindrical wave guides connected together as shown in Fig. B1. The problem is greatly simplified by the fact that all the transmission coefficients (T) are very small. The various components of signals reaching the receive transducer can be classified by the power of the transmission coefficients which multiply them. Since the transmission coefficients are always less than 10^{-2} such a series will converge fast.

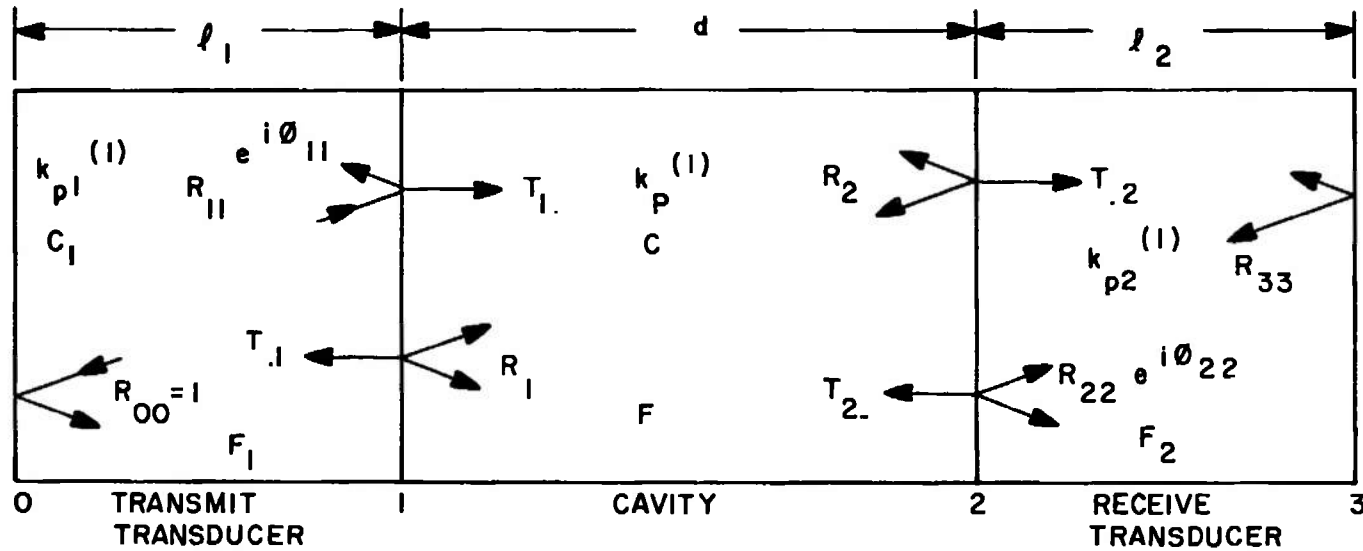
The total forward-going wave due to sound initially trapped in the transmitter can be expressed as the product of the amplitude of the signal introduced at $z = 0$ (A_o) times the response of the coupling hole F_1

$$A_f = A_o F_1 = \frac{A_o e^{-ik_p^{(1)} \ell_1}}{1 + R_{00} R_{11} \exp - 2i \left(k_p^{(1)} \ell_1 + \phi_{11} \right)} \quad (B.1)$$

This is the total primary wave incident on the interface (1) of Fig. B1. The expression for F_1 is summing multiple reflections of the waves trapped in the coupling hole and evaluating at $z = \ell$. The reflection coefficients R_{00} and R_{11} are defined in Fig. B1. ϕ_1 is the phase shift of the reflection coefficient at the exit of the coupling hole interface (1). Similar quantities are defined for each of the three parts of the cavity resonator in Fig. B1.

The total primary wave exiting the cavity is $A_f T_1$. This wave undergoes multiple reflections. The resulting primary forward wave at interface (2) is then

$$B_f = A_o F_1 T_1 \cdot F \quad (B.2)$$



LEGEND:

 F_1, F_2, F

RESPONSE FUNCTION OF SECTION INDICATED BY THE SUBSCRIPT.

 C_1, C_2, C

SOUND SPEED

 $k_{p1}^{(1)}, k_{p2}^{(1)}, k_p^{(1)}$

TRAVELING WAVE NUMBER FOR APPROPRIATE SECTION AS DEFINED IN APPENDIX A.

Fig. B1. Definition of terms for coupling hole problem.

This signal is then introduced into the receive coupling hole to give a total received primary wave

$$C_f = A_o F_1 T_1 \cdot F T_2 F_2 \quad (B. 3)$$

A backward primary wave is also generated in the cavity. This wave incident on interface (1) is transmitted into the transmitter coupling hole. A secondary forward wave is thus generated which leads to a secondary component in the received signal. This signal has two additional transmission coefficients as multipliers since it passes through interface (1) two additional times as compared with the primary waves. An additional secondary wave is generated by the backward primary wave from the receive coupling hole. The total secondary wave is

$$C_f^{(2)} = \left[R_1 T_2 \cdot T_1 F_2 F \exp - i \left(k_p^{(1)} d - k_{p2}^{(1)} \ell_2 \right) \right. \\ \left. + R_0 T_1 T_1 \cdot F F_1 \exp - i \left(k_{p1}^{(1)} \ell_1 - k_p^{(1)} d \right) \right] C_f \quad (B. 4)$$

The products $T_2 \cdot T_1$ and $T_1 T_1 \dots$ are typically of the order of 10^{-6} so that secondary and higher order waves can be neglected.

The receive signal is given by Eq. (B. 3). The reflection and transmission coefficients are complex and slightly frequency dependent. However, this effect is small and can be considered as a constant system phase shift over a cavity linewidth. The reflection and transmission coefficients at the cavity coupling hole interface are the traveling wave coefficients calculated in Appendix C. Notice that the large insertion loss in the cavity, typically 120 dB, is required to make the contributions of secondary and higher order waves small. The results rapidly become intractable as the higher order terms become important.

APPENDIX C

REFLECTION AND TRANSMISSION COEFFICIENTS AT
COUPLING HOLES

The excitation of a fluid filled cavity with coupling holes is a complicated process because small holes, the order of the wavelength of viscous and thermal waves, must be used to preserve the Q of the cavity. Each of the three wave systems: acoustic, viscous (vortex) and thermal (entropy) waves, satisfy a wave equation independently at every point within the fluid. The waves couple on interfaces between solids and fluids. This coupling dictates the relative partition of energy between the acoustic, viscous and thermal wave types. However, the acoustic mode wave functions alone may be used to match velocity and pressure at the interface of the cavity and the coupling hole. The main contributions of viscous and thermal waves are contained in the imaginary parts of $k_p^{(1)}$ and $\gamma_p^{(1)}$ from Appendix A.

In the present discussion we calculate the linewidth of a cavity fed by a centered coupling tube on one end wall and tapped by a centered receiving tube on the other end wall. The coupling holes cause line broadening, shift the center frequency and introduce a phase shift between the electrical signals and the pressure wave in the cavity. The reflection coefficient for traveling waves in the coupling tube and the cavity will be calculated using normalized waves from Appendix A, which already satisfy the boundary conditions on the side walls of the cavity and the coupling tubes. This means symmetric radial modes for a circular wave guide in the present case. The terminology is indicated in Fig. C1.

Here we consider a wave incident on the coupling hole from the cavity in the s th radial mode. In the reflection process other modes, ϕ_n , are generated in the cavity and radial mode waves, ψ_m , are excited in the coupling hole. The other modes in addition to the incident mode are required because the particle velocity in the junction plane (σ) between the cavity and the coupling tube does not correspond to a pure mode of the cavity or the coupling tube.

We insist that the medium does not come apart so the particle velocity is continuous, and that energy is conserved so the stress is continuous across any surface. Losses due to the thermal and viscous waves required on the solid portion of the wall (S) are taken into account by adding the appropriate linewidth for a closed cavity to the linewidth due to losses to the coupling hole area (σ) (see Fig. C1). Note that in

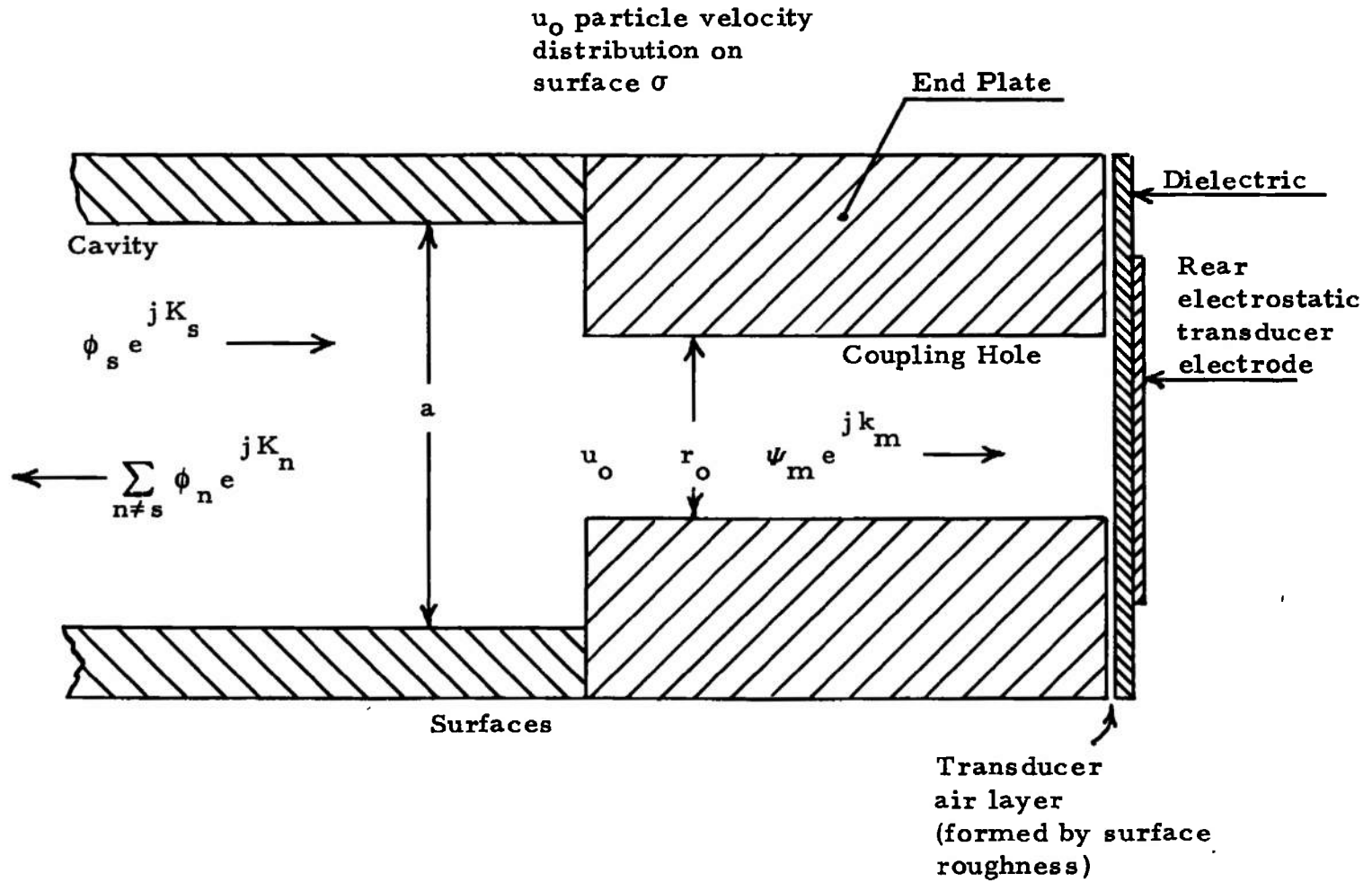


Fig. C1. Terminology for hole coupling problem.

what follows little explicit mention of thermal and viscous waves is made. Since no coupling of the viscous thermal and acoustic waves occurs in σ , the stresses and particle velocity due to each wave type separately must be continuous in σ . Viscous and thermal waves sufficient to satisfy the boundary condition on S and the side walls of the tube come close (1 pt in 10^6) to satisfying the continuity condition for all the waves automatically. The effects of viscous and thermal waves therefore are assumed to be accounted for by using acoustic traveling wave modes with wall losses. Our first task is to set up and solve an integral equation for the particle velocity u_o^s in (σ) when the sth cavity mode is incident on the cavity end wall.*

Since the radial part of the traveling wave functions for tubes can be normalized to form a complete orthogonal set, continuity of axial particle velocity (u_o^s) at $z = 0$ (on σ) can be assured by simply expanding u_o^s in the two sets of traveling wave functions. For instance, the axial particle velocity in the cavity u^s is

$$u^s = \phi_s \sinh(\theta_s + jK_s z) + \sum_{n \neq s} U_n^s \phi_n e^{-jK_n z} \quad (C.1)$$

where the (sinh) notation is used to represent the sum of the incident and reflected sth mode wave. Similarly, the axial particle velocity in the coupling tube is

$$u^m = \sum_m V_m^s \psi_m e^{jk_m z} \quad (C.2)$$

where K_n and k_m are the wave numbers** for the n and mth modes in the cavity and the coupling tube, respectively. Note that we have assumed that the wave equation is separable with the solution to the radial wave equation being $\psi(r)$. This is not possible in the corners of the wave guide. However, a small error discussed below is introduced (1 pt in 10^9) by this assumption. The coupling coefficients U_n^s and V_m^s are defined so that they give the proper particle velocity distribution u_o^s in the coupling area σ . That is, the U_n^s and V_m^s are the projections† of u_o^s on ψ_m and ϕ_n

*The notation and approach are those of Ref. C1.

**The wave numbers are given by Eq. (A.46) of Appendix A. A new notation has been adapted here for simplicity.

† The abbreviated notation means

$$\langle \psi | u \rangle = \int_{\sigma} \psi u d\sigma; dv = 2\pi r dv.$$

$$U_n^s = \langle \phi_n | u_o^s \rangle \quad (C. 3)$$

and

$$V_m^s = \langle \psi_m | u_o^s \rangle . \quad (C. 4)$$

The generalized phase angle (θ_n) in terms of the coupling coefficients is

$$\sinh \theta_n = \langle \phi_n | u_o^s \rangle . \quad (C. 5)$$

Finally, expressions for the reflection coefficient R_s for the incident wave in the cavity as well as the transmission and excitation coefficient for the various waves excited during reflection will make the above definitions more concrete. The reflection coefficient is

$$R_s = e^{-2\theta_s} . \quad (C. 6)$$

The excitation coefficient of coupled modes in the cavity is

$$R_n^s = 2 U_n^s e^{-2\theta_n} \quad (C. 7)$$

and the transmission coefficient into the coupling tube is

$$T_m^s = V_m^s e^{-\theta_m} . \quad (C. 8)$$

In light of the definition of θ_n , U_n^s and V_m^s above all the needed coefficients can be calculated once the particle velocity in the area σ is known.

Continuity of stress reduces to continuity of pressure for the acoustic wave. The normalization implicit in Eqs. (1) and (2) means that if axial velocity due to the m th mode is

$$u = \psi_m e^{jKz} \quad (C. 9)$$

then the pressure due to the m th mode is

$$p = -\frac{\rho \omega}{K} \psi_m e^{jKz} . \quad (C. 10)$$

The pressure in the cavity is

$$\frac{p}{\omega} = \rho \frac{\phi_s}{K_s} \cosh(\theta_s + jK_s z) - \rho \sum_{n \neq s} \frac{U_n^s}{K_n} \phi_n e^{-jK_n z} \quad (C.11)$$

Similarly, in the coupling tubes the pressure is

$$\frac{p}{\omega} = \rho \sum_m \frac{V_m^s}{K_m} \psi_m e^{jk_m z} \quad (C.12)$$

The equality of the pressure at $z = 0$ gives

$$\phi_s \cosh \theta_s - \langle G^- | u_0^s \rangle - \langle G^+ | u_0^s \rangle = 0 \quad (C.13)$$

where

$$G^- = \sum_{n \neq s} \frac{K_s}{K_n} \phi_n(r_0) \phi_n(r) \quad (C.14)$$

$$G^+ = \sum_m \frac{K_s}{k_m} \psi_m(r_0) \psi_m(r) \quad (C.15)$$

and r_0 is an independent radial coordinate for integration purposes. In order to put (C.13) in a more convenient form, we multiply both sides of (C.13) by u_0^s and integrate over the remaining (r) dependence on σ . In addition, we add to (C.13) after integration the relation

$$\cosh \theta_s \langle u_0^s | \phi_s \rangle = \frac{1}{2} \sinh 2\theta_s \quad (C.16)$$

(obtained from (C.5)). The final integral equation for u_0^s is then

$$\frac{1}{2} \sinh 2\theta_s = 2 \cosh \theta_s \langle u_0^s | \phi_s \rangle \quad (C.17)$$

$$- \left[\langle u_0^s | G^- | u_0^s \rangle + \langle u_0^s | G^+ | u_0^s \rangle \right].$$

A simple variational approach to (C. 18) is possible because the integral equation (C. 17) is quadratic in u_0^s . A useful set of functions to expand u_0^s for the variation is

$$u_0^s = \sum_{\mu=0}^{\infty} A_{\mu} \chi_{\mu} \cosh \theta_s \quad (\text{C. 18})$$

where

$$\chi_{\mu} = \left[1 - \left(\frac{r}{a} \right)^2 \right]^{\mu} \quad (\text{C. 19})$$

The first two such functions are used in the present work. The equations for A_{μ} obtained from (C. 18) and (C. 17) as described below are symmetric and easily extended to any order of μ .^{*} However, calculation for $\mu = 0-2$ shows no significant improvement over the result for $\mu = 0$ and 1. This assumed functional form (C. 18) can be put into (C. 17) to give

$$\begin{aligned} \frac{1}{2} \tan 2\theta_s &= 2 A_0 \langle 1 | \phi_s \rangle + 2 A_1 \langle \chi_1 | \phi_s \rangle \\ &- A_0^2 \langle 1 | G^- + G^+ | 1 \rangle - A_1^2 \langle \chi_1 | G^- + G^+ | \chi_1 \rangle \quad (\text{C. 20}) \\ &- 2 A_0 A_1 \langle 1 | G^- + G^+ | \chi_1 \rangle . \end{aligned}$$

As explained in Ref. 1, page 155, integral equations such as (C. 20) can be used to obtain the "best" values of the unknown parameters A_{μ} by requiring that $\tan 2\theta_s$ have a minima with respect to the variation of the A_{μ} . Thus, setting the partial derivatives with respect to A_0 and A_1 equal to zero two simultaneous equations for A_0 and A_1 are obtained (note we have used the symmetry of G^+ and G^-)

$$\begin{aligned} \langle 1 | G^- + G^+ | 1 \rangle A_0 + \langle 1 | G^- + G^+ | \chi_1 \rangle A_1 &= \langle 1 | \phi_s \rangle \\ \langle 1 | G^- + G^+ | \chi_1 \rangle A_0 + \langle \chi_1 | G^- + G^+ | \chi_1 \rangle A_1 &= \langle \chi_1 | \phi_s \rangle . \end{aligned} \quad (\text{C. 21})$$

^{*}See Ref. C1 for formal results.

These equations can be solved for A_1 and A_0 to give

$$A_0 = \frac{1}{\Delta} \left[\langle 1 | \phi_s \rangle \langle \chi_1 | G^- + G^+ | \chi_1 \rangle - \langle \chi_1 | \phi_s \rangle \langle 1 | G^- + G^+ | \chi_1 \rangle \right]$$

$$A_1 = \frac{1}{\Delta} \left[\langle \chi_1 | \phi_s \rangle \langle 1 | G^- + G^+ | 1 \rangle - \langle 1 | \phi_s \rangle \langle 1 | G^- + G^+ | \chi_1 \rangle \right] \quad (C. 22)$$

where

$$\Delta = \langle 1 | G^- + G^+ | 1 \rangle \langle \chi_1 | G^- + G^+ | \chi_1 \rangle - \langle 1 | G^- + G^+ | \chi_1 \rangle^2.$$

Once the wave functions ϕ_n and ψ_m are known the constants A_0 and A_1 can be evaluated from (C. 22) and $2\theta_s$ calculated from (C. 20). This gives us the required reflection coefficient from (C. 6). In addition, substituting the now known particle velocity u_0^s from (C. 2) into (C. 3) and (C. 4) all the coupling coefficients U_n^s and V_n^s , and the excitation (C. 7) and transmission coefficients can be calculated.

The wave functions required to evaluate the integrals indicated above are the traveling wave functions $J_0(\gamma_p^{(1)} r)$ of Appendix A. These wave functions must be made orthogonal⁽²⁾ and normalized before they can be used. Orthogonalization of the cavity wave functions is not important and

$$\phi_p = \frac{2}{a^2} \frac{J_0(\gamma_p r)}{J_0^2(\gamma_p a)}.$$

However, the suitably normalized wave functions for the coupling tube functions given in Table C. 1 are considerably more complicated.

Fortunately, only the first two functions ψ_p are necessary. Recalling the size of $\gamma_0^{(1)}$ from Appendix A (Eq. A. 47) the orthogonalized wave functions are seen to reduce to the lossless wave functions as

$\gamma_0^{(1)2} \rightarrow 0$. In fact, by the time $p = 100$ atm the lossless wave functions describe the reflection and transmission coefficients typically to 1 part in 10^5 .

Table C.1. First two orthogonalized wave functions in a coupling tube.

$$\phi_0 = \frac{2}{r_0^2} \frac{J_0(\gamma_0^{(1)} r)}{\left(1 + \frac{1}{2} \gamma_0^{(1)2} r_0^2\right)}$$

$$\phi_1 = \frac{2}{r_0^2} \frac{J_0 \gamma_1^{(1)} r}{J_0^2(\gamma_1^{(1)} r_0)} \left[1 - \frac{2}{r_0^2} \frac{\gamma_0^{(1)2}}{\gamma_1^{(1)2}} \frac{1}{J_0(\gamma_1^{(1)} r_0)} \right]$$

REFERENCES

- C1. Theoretical Acoustics, P. M. Morse, K. U. Ingard, McGraw-Hill, New York, 1968, pp. 527-533.
- C2. Methods of Mathematical Physics, Vol. I., P. M. Morse, H. Feshbach, McGraw-Hill, New York, 1953, p. 928.